

Biomimetic Accommodating Intraocular Lens

Thesis by

Charles DeBoer

In Partial Fulfillment of the Requirements

for the Degree of

Doctor of Philosophy



California Institute of Technology

Pasadena, California

2012

(Defended May 30, 2012)

© 2012

Charles DeBoer

All Rights Reserved

To: My Wife, Leakana

Acknowledgements

I would like to thank everyone who has helped me arrive at this point in my academic career. First and foremost, I would like to thank my wife, Leakana, who continually supports me no matter what crazy endeavor I am pursuing. She takes care of me when I don't sleep, proofreads my work at all hours, gives me encouragement, and does not hold back her honest opinion. I would like to thank my family for encouraging me to advance myself academically, even when I held a good engineering job. I would not have been able to be here without encouragement. As I finish my PhD, I can see how much I have learned in the past five years of medicine and engineering and I feel this learning process has opened many doors for my future career.

This research would not have been possible without help from so many people. Thank you to Hyung Wan Do for your help with the material testing. I would like to thank all of our surgeons for defining and refining our surgical techniques, which allowed *ex vivo* testing of our lens. Thank you, Roberto Gonzalez, for developing the initial surgical procedures. The first dissections seemed impossible and we had little guidance because we were trying out and refining a new surgical and testing technique. Your assistance with developing the testing procedures provided a fundamental step in the ability to measure IOL performance. Juan Carlos Gutierrez, Juan Carlos Martinez, and Raul Lopez are all great friends and innovators of the surgical technique. You took a challenging surgical technique, performed it with small surgical incisions, and then refined it for absolute repeatability. Thank you for all the countless hours you helped to prepare tissue and achieve device reliability.

I would like to thank all of the MEMS lab members who trained me on how to use the machines. Thank you Trevor Roper for maintaining the machines that we broke

and thank you, Christine Garske, for supporting my project and always being dependable and helpful. I will never forget the many gastronomic adventures with the MEMS lab.

My advisors, Dr. Tai and Dr. Humayun, taught me the most valuable lessons during the PhD. Both are successful, kind, approachable, and supportive. They truly set the standard for excellence in research, mentoring, and scholarship. I feel very thankful to have been able to work with them on this project.

Dr. Tai taught me how to conduct fundamental research and to recognize the importance of understanding the basic operational principles behind a device. I will carry this fundamental thinking process with me throughout my career. Dr. Tai is an inspiring advisor at Caltech and truly cares about his students. I would also like to thank Dr. Tai for telling me his honest opinion on all subjects. This guidance has allowed me to work in a much more efficient manner.

Dr. Humayun has guided me even before entering the MD/PhD program. Out of the many things he has taught me, the most important is how to work in a space without all of the answers. This includes being able to judge and manage research risks, learning to present work in an effective manner, and keeping the big picture in mind. To solve big problems with a disruptive technology requires this type of thinking. In addition, he has taught me how to structure medically relevant research. The idea of solving presbyopia for a PhD thesis may seem a daunting task, but when I started with the clinical problem first, my final solution matched what was needed and I was not caught looking for an application to my technology. Thank you for always being available to guide me and train me in medicine and engineering. I look forward to the many years we will work together.

I would like to thank everyone who has helped me academically. This would start with what I consider the best elementary school in the world: Shorewood Hills in

Madison, Wisconsin. Located next to university housing and in the village where many of the professors from around the world lived, it was a small international community. This international community immersed me in a diverse worldview. At Shorewood Hills, I learned to understand different perspectives and customs at an early age. Occidental College paralleled this diversity and, in addition, provided rigorous training in developing my thought process by strengthening my analytical thinking skills. Occidental was one of the most supportive institutions I have attended. When I think about Occidental, a few examples come to mind, including Cecilia Fox, who guided me through medical school interviews years after graduation, tirelessly read each application, helped me with revisions, and let me know when I was ready. I would not be at this point in my life without her. Professor Schmeideshoff taught me how to conduct physics research the summer of my sophomore year at Occidental, had me co-author a paper with him, and helped me eight years later by giving me excellent recommendations for medical school. This dedicated support that Oxy gave to me has greatly helped me in my academic and career paths. I would like to thank Caltech for the scientific training I have received. In particular, I believe that the honor system guides not only coursework, but also scientific rigor. All of the faculty, students, and staff that I have interacted with are outstanding. This culture of excellence encourages us all to perform at a higher level. I cannot imagine a better place to conduct scientific research. I would like to thank the MD/PhD program at USC/Caltech for encouraging me to conduct device-based research, which directly helps patients. This flexibility with regard to diverse research paths is rare to find in an MD/PhD program and I do not think I could have done this anywhere else.

I would like to thank everyone who taught me how to think out of the box and inspired innovation. This started with my Grandfather Spransy, who inspired me with everything he built, including a heavily modified Studebaker he called the Green Dragon,

working model steam-powered boats, welded clocks, and weathervanes. I would like to thank the madlab, including Aaron Barnes and Matt McCormick, who guided me to think independently and imaginatively. They gave me the confidence to build prototypes unlike anything made before. This skill has greatly helped me with my PhD and in medical device research.

Abstract

Biomimetic Accommodating Intraocular Lens

Thesis by

Charles DeBoer

Doctor of Philosophy in Electrical Engineering

California Institute of Technology

The crystalline lens allows the eye to focus on near and far objects. During the aging process, it loses its ability to focus and often becomes cloudy during cataract formation. At this point, traditional medical therapy replaces the lens with an artificial replacement lens. Although replacement lenses for the crystalline lens have been implanted since 1949 for cataract surgery, none of the FDA-approved lenses mimic the anatomy of the natural lens. Hence, they are not able to focus in a manner similar to the youthful lens. Instead, they function in a manner similar to the aged lens and only provide vision at a single distance or at a very limited range of focal distances. Patients with the newest implants are often obliged to use reading glasses when using near vision, or suffer from optical aberrations, halos, or glare. Therefore, there is a need to provide youthful vision after lens surgery in terms of focusing ability, accurate optical power, and sharp focus without distortion or optical aberrations.

This thesis presents an approach to restoring youthful vision after lens replacement. An intraocular lens (IOL) that can provide accurate visual acuity along with focusing ability is proposed. This IOL relies on the natural anatomy and physiology of

the eye, and therefore is actuated in a manner identical to the natural lens. In addition, the lens has the capability for adjustment during or after implantation to provide high-acuity vision throughout life.

The natural anatomy and physiology of the eye is described, along with lens replacement surgery. A lens design is proposed to address the unmet need of lens-replacement patients. Specific care in the design is made for small surgical incisions, high visual acuity, adjustable acuity over years, and the ability to focus similar to the natural lens. Methods to test the IOL using human donor tissue are developed based upon prior experiments on the *ex vivo* natural lens. These tools are used to demonstrate efficacy of the newly developed accommodating intraocular lens.

To further demonstrate implant feasibility, materials and processes for building the lens are evaluated for biocompatibility, endurance, repeatable manufacture, and stability. The lens biomechanics are determined after developing an artificial anatomy testing setup inspired by the natural anatomy of the human focusing mechanism. Finally, based upon a mechanical and optical knowledge of the lens, several improved lens concepts are proposed and demonstrated for efficacy.

Table of Contents

BIOMIMETIC ACCOMMODATING INTRAOCULAR LENS	I
ACKNOWLEDGEMENTS	IV
ABSTRACT.....	VIII
TABLE OF CONTENTS	X
LIST OF FIGURES	XIV
LIST OF TABLES	XIX
1 BACKGROUND	1
1.1 OPTICAL CHARACTERIZATION OF THE EYE.....	3
1.2 ACCOMMODATION REFLEX	8
1.3 PATHOLOGY OF THE EYE: PRESBYOPIA	12
1.4 PATHOLOGY OF THE EYE: CATARACT.....	14
1.5 LENS REPLACEMENT	16
1.6 CURRENT INTRAOCULAR LENS TECHNOLOGY	17
1.7 CONCLUSION	21
2 SILICONE AS A BIOMATERIAL.....	23
2.1 INTRODUCTION	23
2.2 CROSSLINKING SILICONE ELASTOMERS.....	24
2.3 RESINS AND FILLERS	26
2.4 BIOCOMPATIBILITY.....	26
2.5 IMPLANT STABILITY IN THE BODY	27

2.6	DIFFUSION OF SILICONE OIL AND EXTRACTION.....	28
2.7	SILICONE BASE MATERIAL: NUSIL MED4-4210.....	29
2.8	EXPERIMENTAL	30
2.9	GLASS TRANSITION TEMPERATURE.....	31
2.10	DYNAMIC MECHANICAL ANALYSIS.....	33
2.11	GLASS TRANSITION TEMPERATURE OF MED4-4210.....	36
2.12	CURING SCHEDULE.....	39
2.13	REPEATABILITY OF MIXING.....	41
2.14	RATIO OF PART A TO PART B	43
2.15	CREEP-RECOVERY TESTING	45
2.16	STRESS RELAXATION.....	53
2.17	PERMEABILITY OF SILICONE	54
2.18	LENS ACCELERATED AGING TESTS	58
2.19	SUMMARY	59
3	MEASURING ACCOMMODATION IN A EX VIVO SETTING	61
3.1	INTRODUCTION	61
3.2	SURGICAL IMPLANTATION AND MOUNTING OF LENS	63
3.3	STRETCHING APPARATUS	71
3.4	LENS INSERTION TOOL	73
3.5	INFUSION / ASPIRATION SYSTEM	74
3.6	OPTICAL TEST METHODS	79
3.7	OPTICAL TEST SETUP VALIDATION	84
3.8	BENCH-TOP TESTING OF LENS FOR ACCOMMODATION	85

3.9	CONCLUSION	85
4	ACCOMMODATING INTRAOCULAR LENS	87
4.1	INTRODUCTION	87
4.2	REQUIREMENTS FOR AN ACCOMMODATING INTRAOCULAR LENS.....	88
4.3	OVERVIEW OF LENS DESIGN.....	89
4.4	MEMS-ENABLED INJECTION PORT	93
4.4.1	<i>Design for Use with Accommodating IOL</i>	<i>93</i>
4.4.2	<i>MEMS-Enabled Injection Port for High-Pressure Applications</i>	<i>98</i>
4.5	LENS BODY AND ASSEMBLY	101
4.6	CONCLUSION	103
5	LENS MECHANICS	104
5.1	INTRODUCTION	104
5.2	NATURAL LENS STRETCH WITH DIFFERENT CAPSULOTOMIES.....	105
5.3	ARTIFICIAL LENS CAPSULE	109
5.4	SCHEIMPFLUG CAMERA SYSTEM	113
5.5	PRESSURE MONITORING	118
5.6	LENS BIOMECHANICS DATA	120
5.7	BASE POWER ADJUSTMENT	125
5.7.1	<i>Power Adjustment with Fill Volume.....</i>	<i>126</i>
5.7.2	<i>Power Adjustment with Refractive Index</i>	<i>127</i>
5.8	ACCOMMODATION VERSUS FILL VOLUME	128
5.9	FINITE ELEMENT MODELING OF LENS	131
5.10	EXPERIMENTAL VALIDATION OF DESIGN IN PORCINE AND HUMAN TISSUE	136

5.10.1	<i>Porcine Eye Validation</i>	137
5.10.2	<i>Human Eye Validation</i>	138
5.11	CONCLUSION	140
6	LENS OPTIMIZATION	142
6.1	INTRODUCTION	142
6.2	HIGH-INDEX LENS	143
6.3	BASE-POWER-CORRECTED HIGH-INDEX LENS	144
6.4	CONCLUSION	148
7	CONCLUSION	149
	APPENDIX A: BIOLOGICAL TESTING DATA, MED4-4210	151
	APPENDIX B: INDEX OF SILICONE ELASTOMER TESTING, MED4-4210.....	152
	REFERENCES	153

List of Figures

FIGURE 1-1. ANATOMY OF THE HUMAN EYE	4
FIGURE 1-2. LIGHT PATH PASSING THROUGH CORNEA, TO AQUEOUS HUMOR, THROUGH THE LENS, AND BEING FOCUSED ON THE RETINA.....	5
FIGURE 1-3. DIAGRAM OF THE GRADIENT INDEX OF NATURAL LENS [10].....	6
FIGURE 1-4. CLOSEUP OF CILIARY MUSCLE, IRIS, AND LENS.....	7
FIGURE 1-5. NEURAL ACCOMMODATION REFLEX.....	10
FIGURE 1-6. ACCOMMODATION MECHANISM	11
FIGURE 1-7. ACCOMMODATIVE AMPLITUDE VERSUS AGE [17].....	12
FIGURE 2-1. PDMS MOLECULE.....	23
FIGURE 2-2. PLATINUM-CATALYZED CROSSLINKING REACTION.....	25
FIGURE 2-3. GLASS TRANSITION TEMPERATURE DIAGRAM.....	32
FIGURE 2-4. STORAGE MODULUS AND TAN δ VERSUS TEMPERATURE FOR A SAMPLE OF MED4-4210.....	38
FIGURE 2-5. YOUNG'S MODULUS VERSUS CURING TIME FOR NUSIL MED4-4210 AT DIFFERENT CURING TEMPERATURES	40
FIGURE 2-6. MODULUS OF ELASTICITY VERSUS A/B RATIO OF MED4-4210.....	44
FIGURE 2-7. FOUR-ELEMENT MODEL.....	46
FIGURE 2-8. TYPICAL CREEP-RELAXATION CURVE.....	47
FIGURE 2-9. DIAGRAM DEMONSTRATING HOW TO CALCULATE MODULUS OF ELASTICITY, VISCOSITY, RELAXATION TIME, AND IRRECOVERABLE STRAIN.....	48
FIGURE 2-10. CREEP EXPERIMENT: STRESS AND STRAIN VERSUS TIME FOR AN EXAMPLE EXPERIMENT.....	49

FIGURE 2-11. UPTAKE EXPERIMENT FROM THREE SAMPLES	57
FIGURE 2-12. LENS WEIGHT VERSUS TIME FOR LENSES FILLED WITH 100 CST SILICONE OIL AND 1000 CST SILICONE OIL	58
FIGURE 2-13. SUMMARY OF WEIGHT LOSS FOR LENSES AFTER 8 WEEKS OF ACCELERATED TESTING.....	59
FIGURE 3-1. KERATECTOMY, CONTINUOUS CIRCULAR CAPSULORHEXIS AND LENS EXTRACTION IS PERFORMED	64
FIGURE 3-2. REMOVAL OF THE IRIS	65
FIGURE 3-3. REMOVAL OF THE LENS	65
FIGURE 3-4. LENS INJECTOR, DEVELOPED TO PLACE LENS INSIDE LENS CAPSULE	66
FIGURE 3-5. MANUAL INSERTION OF THE LENS INTO THE LENS INJECTOR	66
FIGURE 3-6. INJECTION OF THE LENS INTO THE LENS CAPSULE	67
FIGURE 3-7. INJECTION OF FLUID INTO THE IMPLANTED LENS AFTER ACCESSING THE LENS REFILL VALVE.....	67
FIGURE 3-8. SCLERECTOMY	68
FIGURE 3-9. REMOVAL OF THE FOCUSING MECHANISM, INCLUDING THE CILIARY MUSCLE, ZONULES, LENS CAPSULE, AND IMPLANTED LENS	68
FIGURE 3-10. REMOVAL OF RESIDUAL VITREOUS FROM THE POSTERIOR POLE OF THE LENS CAPSULE.....	69
FIGURE 3-11. PREPARATION FOR GLUING THE CILIARY MUSCLE TO THE STRETCHING APPARATUS	69
FIGURE 3-12. GLUING THE CILIARY MUSCLE TO THE STRETCHING APPARATUS	70
FIGURE 3-13. LENS MOUNTED AND PREPARED FOR OPTICAL TESTING	71

FIGURE 3-14. STRETCHING APPARATUS	72
FIGURE 3-15. THE LENS INSERTER IS SHOWN WITH THE LENS LOADED (LEFT) AND BEING DELIVERED (MIDDLE AND RIGHT)	74
FIGURE 3-16. FILLING OF THE ACCOMMODATING IOL	75
FIGURE 3-17. FLUIDIC INJECTOR HANDPIECE	75
FIGURE 3-18. DIAGRAM OF THE INFUSION / ASPIRATION SYSTEM (TOP).....	76
FIGURE 3-19. SCHEMATIC OF INFUSION / ASPIRATION SYSTEM.....	78
FIGURE 3-20. ACCOMMODATION TEST SETUP DIAGRAM.	80
FIGURE 3-21. BASIC TEST SETUP FOR MEASURING FOCAL LENGTH OF A LENS	80
FIGURE 3-22. ACCOMMODATION TEST SETUP PICTURE	81
FIGURE 3-23. SINGLE IMAGE OF A LASER GOING THROUGH LENS (TOP).....	82
FIGURE 3-24. ANALYZED DATA	83
FIGURE 3-25. AUTOMATED ANALYSIS.....	83
FIGURE 4-1. BIOMIMETIC ACCOMMODATING IOL: ACCOMMODATED (LEFT) AND NON- ACCOMMODATED (RIGHT)	90
FIGURE 4-2. THE INJECTION PORT AND ACCOMMODATING INTRAOCULAR LENS.....	90
FIGURE 4-3. INSERTION OF THE LENS THROUGH A SMALL CORNEAL INCISION	91
FIGURE 4-4. LENS FILLED TO REQUIRED OPTICAL POWER AFTER INSERTION INTO THE LENS CAPSULE (SHOWN IN DOTTED LINES)	92
FIGURE 4-5. THE SELF-SEALING INJECTION PORT CLOSSES ONCE THE LENS INSERTER IS FINISHED FILLING	92
FIGURE 4-6. PRESSURE CHAMBER USED TO MEASURE RESEALABLE MEMBRANES.	94

FIGURE 4-7. NEEDLE DIAMETER VERSUS SEALING PRESSURE FOR VARIOUS MEMBRANE THICKNESSES.....	96
FIGURE 4-8. SCHEMATIC OF FINITE ELEMENT ANALYSIS BOUNDARY CONDITIONS	96
FIGURE 4-9. SIMULATION OF LOWER EDGE INCISION VERSUS PRESSURE	97
FIGURE 4-10. SIMULATED VERSUS EXPERIMENTAL CRACKING PRESSURE OF 135 μm INCISION	97
FIGURE 4-11. SIMULATED AND EXPERIMENTAL DATA FOR A 311 μm INCISION	98
FIGURE 4-12. FABRICATED VALVE.....	100
FIGURE 4-13. VALVE FABRICATION PROCESS.....	100
FIGURE 4-14. INJECTION INTO FABRICATED VALVE.....	100
FIGURE 4-15. ONE HALF OF THE LENS MOLD.....	102
FIGURE 4-16. FABRICATION PROCESS	103
FIGURE 4-17. LENS PROTOTYPE	103
FIGURE 5-1. BASE POWER FOR SEVERAL CAPSULOTOMIES IN A PORCINE LENS.....	106
FIGURE 5-2. SIDE AND TOP VIEW OF THE CAPSULOTOMY	106
FIGURE 5-3. ACCOMMODATION LEVELS OF A PORCINE LENS WITH NO CAPSULOTOMY (LEFT), 5 MM ANTERIOR CENTRAL CAPSUOLTOMY (MIDDLE) AND 5 MM ANTERIOR AND POSTERIOR CAPSULOTOMIES (RIGHT)	108
FIGURE 5-4. ARROW MARKS THE DISCONTINUITY IN INK PLACED ACROSS CAPSULOTOMY.....	108
FIGURE 5-5. ARTIFICIAL CAPSULE WITH LENS IMPLANTED INSIDE.....	110
FIGURE 5-6. ARTIFICIAL CAPSULE ATTACHED TO THE STRETCHING APPARATUS WITH NO LENS IMPLANTED.....	110
FIGURE 5-7. ARTIFICIAL CAPSULE IN STRETCHING APPARATUS WITH LENS IMPLANTED...	111

FIGURE 5-8. FABRICATION FOR ARTIFICIAL CAPSULE	113
FIGURE 5-9. SLIT ILLUMINATION OF THE LENS IN THE ARTIFICIAL LENS CAPSULE	114
FIGURE 5-10. SCHEIMPFLUG (ABOVE) AND PICTURE (BELOW) OF SCHEIMPFLUG CAMERA SYSTEM	115
FIGURE 5-11. SCHEIMPFLUG PRINCIPLE [84]	116
FIGURE 5-12. IMAGES TAKEN FROM THE SCHEIMPFLUG IMAGING SYSTEM.....	118
FIGURE 5-13. TOP AND SIDE VIEW OF LENS WITH INSERTED PRESSURE TRANSDUCER.....	119
FIGURE 5-14. IMPROVED METHOD OF PRESSURE MONITORING	120
FIGURE 5-15. INFLATION OF THE LENS AT DIFFERENT PRESSURES. AT MAXIMUM INFLATION, THE LENS IS AT AN INTERNAL PRESSURE OF 41 MMHG.....	120
FIGURE 5-16. PRESSURE VERSUS VOLUME FOR THE INSERTED LENS TRANSDUCER FOR 8 TRIALS.....	121
FIGURE 5-17. LENS PRESSURE CHANGE DURING ACCOMMODATION	122
FIGURE 5-18 LENS DIAGRAM	125
FIGURE 5-19. LENS POWER VERSUS FILL WEIGHT.....	126
FIGURE 5-20. LENS POWER VERSUS REFRACTIVE INDEX OF FILLING MEDIA	128
FIGURE 5-21. BASE POWER VERSUS PERCENT FILL FOR SIX IMPLANTED LENSES.....	130
FIGURE 5-22. PERCENT OF MAXIMUM ACCOMMODATION VERSUS PERCENT FILL FOR SIX IMPLANTED LENSES	130
FIGURE 5-23. FINITE ELEMENT ANALYSIS MESH.....	132
FIGURE 5-24. MESH WITH BOUNDARY CONDITIONS	134
FIGURE 5-25. FINITE ELEMENT MODEL VERSUS RAW IMAGES FOR NON-STRETCHED AND STRETCHED CONDITION	135

FIGURE 5-26. ACCOMMODATION AMPLITUDE VERSUS TRIAL NUMBER FOR FOUR IMPLANTED LENSES STRETCHED AT 4 MM DIAMETER.....	137
FIGURE 6-1. CROSS SECTION OF A DUAL LENS.....	145
FIGURE 6-2. TWO PART LENS	146
FIGURE 6-3. SIMPLIFIED RAY TRACE THROUGH DUAL LENS.....	147
FIGURE 6-4. SCHEIMPFLUG IMAGE OF DUAL LENS IN THE NOT-STRETCHED AND STRETCHED CONDITION	147

List of Tables

TABLE 1. LE GRAND MODEL OF EYE [9].....	5
TABLE 1-2. CURRENT INTRAOCULAR LENS TECHNOLOGY	19
TABLE 2-1. GLASS TRANSITION TEMPERATURE PEAKS IN CURE SCHEDULES FOR MED4-4210.....	39
TABLE 2-2. TABULATED VALUES OF YOUNG’S MODULUS AT VARIOUS CURING CONDITIONS	41
TABLE 2-3. MODULUS OF ELASTICITY MEASURED FROM 5 WAFERS	42
TABLE 2-4. MODULUS OF ELASTICITY VERSUS MIX RATIO	45
TABLE 2-5. VISCOELASTIC PROPERTIES AT BODY TEMPERATURE (37 °C) UNDER DIFFERENT CURING SCHEDULES.....	51
TABLE 2-6. VISCOELASTIC PROPERTIES AT ELEVATED TEMPERATURE (100 °C) UNDER DIFFERENT CURING SCHEDULES.....	52
TABLE 2-7. STRESS VALUES AT 0, 2, AND 10 MIN FOR DIFFERENT CURING CONDITIONS	54
TABLE 2-8. DIFFUSION CONSTANTS FOR THREE SAMPLES	57

TABLE 3-1. WEIGHT VALUES FOR A TARGET WEIGHT OF 100 MG	79
TABLE 3-2. THE TABULATED POWER REFERS TO THE POWER STATED BY THE IOL MANUFACTURER.....	84
TABLE 5-1. VALIDATION OF SCHEIMPFLUG IMAGING SYSTEM	117
TABLE 5-2. LENS STRETCHING ON THE LASER SCANNING APPARATUS AND THE SCHEIMPFLUG IMAGING SYSTEM.....	117
TABLE 5-3. LENS DIMENSIONS, OPTICAL PROPERTIES, AND PRESSURE DURING STRETCHING IN ARTIFICIAL CAPSULE	123
TABLE 5-4. COMPARISON OF SCHEIMPFLUG IMAGING AND FINITE ELEMENT ANALYSIS FOR LENS STRETCHING	135
TABLE 5-5. PRESSURE OF LENS VERSUS FINITE ELEMENT SIMULATION.	135
TABLE 5-6 ACCOMMODATION LEVELS FROM 8 HUMAN LENS IMPLANT TRIALS WITH 5 MM CILIARY MUSCLE STRETCH	138
TABLE 5-7 ACCOMMODATION LEVELS FROM FIVE HUMAN LENS IMPLANTS WITH FIVE DISTINCT LENSES	139
TABLE 6-1. ACCOMMODATION POWER FOR LENSES WITH TWO DIFFERENT REFRACTIVE INDICES	143
TABLE 6-2. DUAL LENS POWER AS ASSESSED BY LASER SCAN AND THEORETICAL POWER WITHOUT THE INTERNAL DIVERGING LENS	148

1 BACKGROUND

Restoring youthful vision after lens removal is an active area of research and development [1-8]. Throughout life, the natural lens inside the eye ages and optical performance deteriorates. In humans, the lens loses its ability to dynamically change focal power in a process called presbyopia. Often, the lens will become opaque or cloudy during formation of a cataract. Currently, there are methods of replacing the natural lens with an optically clear lens after cataract formation. However, restoration of accommodation is currently an active area of research.

This work is aimed toward finding a biomedical solution to cure presbyopia. This thesis will address the clinical problem of presbyopia, current therapies for lens replacement, and then propose and evaluate a therapeutic solution for presbyopia. The solution is based on replacing the aged or cataracted lens with a biomimetic lens similar to the youthful lens. The field of microelectromechanical systems (MEMS) is used to fabricate the lens because of the small sizes that can be achieved. MEMS is especially well suited for a replacement human lens because of the small size of the human lens and

the intricacies of the device to make it surgically viable.

Chapter 1 presents the clinical picture of presbyopia and cataracts and discusses current treatment options for both. Chapter 2 develops the base materials for building an artificial lens. The processing techniques for a biocompatible silicone are developed. In addition, the effect of process parameters on material properties is determined. The viscoelastic properties of the material are evaluated to ensure long-term use of the device. Based on these results, silicone is deemed an acceptable material for the implant. Chapter 3 develops a method to test the prototyped lens in *ex vivo* human and porcine tissue. A stretching apparatus is built that attaches to the natural focusing muscles of the eye and stretches them to simulate *in vivo* accommodation. This method is adapted to be used with an implanted MEMS biomimetic lens. The artificial lens is described in Chapter 4 and its performance is evaluated using the methods described in Chapter 3. Data from implantation in human tissue demonstrates the lens' ability to adjust focus to levels that would alleviate presbyopia. Chapter 5 focuses on characterizing the biomechanics of the lens. The performance characteristics of the lens in the human eye as well as in an artificial tissue are evaluated. A finite element model of the lens is made and evaluated relative to cross-sectional imaging of the lens. Chapter 6 presents new advances in the lens technology based on what was learned from Chapter 5. Two lens concepts are built and tested for efficacy.

Much of the work done in this thesis was dependent on animal tissue or human donations. Animal tissue was procured from FDA slaughterhouses and no live animals were used in the studies. I am grateful that the eyes of these animals destined for our food supply could be used for the scientific purposes of alleviating presbyopia. As such I

would like to acknowledge the gifts that these animals gave us to benefit humanity in terms of food and scientific research.

This work is indebted to the kindness of the many human donors who gave their eyes as donations for others and scientific discovery. Your kindness is appreciated and we hope that your gift will serve others through this research. It should be noted that the eyes we received were not suitable for human transplantation due to low endothelial cell counts. Therefore, this work did not interfere with the most important part of donation, giving the gift of sight to another human.

1.1 Optical Characterization of the Eye

To understand the process of presbyopia and cataract formation as well as their clinical impact, it is important to understand the basic anatomy and physiology of the human eye. The cornea and natural lens of the eye are responsible for focusing light onto the photoreceptors in the retina. The cornea acts as a fixed focal length lens and provides most of the optical power of the eye. The lens has less refractive power. However, it provides a variable focal length. This allows the eye to focus on near and far objects.

Figure 1-1 shows the major anatomic components of the eye. Figure 1-2 shows a collimated light beam focused on the retina. As light passes through the eye, it first is focused by the cornea, which has a refractive index of 1.376 and an external radius of curvature of 7.8 mm [9]. After passing through the cornea, the light path traverses aqueous humor in the anterior chamber of the eye, which has an index of refraction of 1.336 and then passes through the lens. The Le Grand schematic eye model is shown in Table 1. The total power of the cornea in this model is 48.3 D while the lens itself

contributes 21.8 D of the total eye power. The high power of the cornea is due to the large difference in refractive indices when the light travels from air ($n=1$) to the cornea. Although the lens contributes less to the total refractive power of the eye, it provides the ability to adjust, allowing humans to focus on near and far objects.

The lens is contained within a lens capsule and has a gradient index. This gradient index accounts for the higher power observed from the lens than would be predicted from a uniform index. When the lens is modeled as having a uniform index of refraction, it is given a value of 1.42. However, in the actual lens, the maximum index of refraction is 1.406 in the center of the lens, and 1.386 in the cortex of the lens (Figure 1-3). Therefore, the gradient index provides a substantial amount of power to the lens.

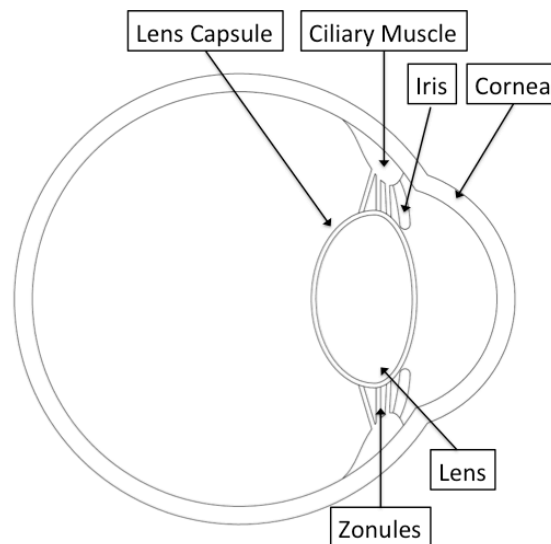


Figure 1-1. Anatomy of the human eye

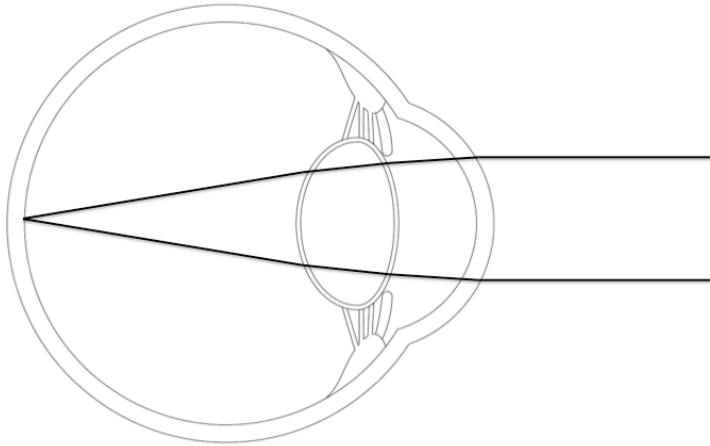


Figure 1-2. Light path passing through cornea, to aqueous humor, through the lens, and being focused on the retina

Table 1. Le Grand model of eye [9]

	Refractive Index (n)	Radius of Curvature (mm)	Surface Power (Diopters)	Total Power (Diopters)
Cornea Anterior Surface	1.3771	7.8	48.346	42.356
Cornea Posterior Surface	1.3771	6.5	-6.108	
Lens Anterior Surface	1.42	10.2	8.098	21.779
Lens Posterior Surface	1.42	-6.0	14.000	

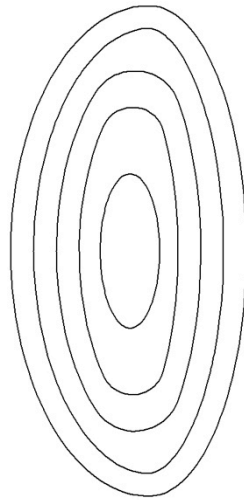


Figure 1-3. Diagram of the gradient index of natural lens [10]. Isoindicial lines of the lens are marked.

After passing through the lens, light travels through the vitreous humor, which has an index of refraction of 1.336 and is focused onto the retina, which contains the photoreceptors. The macula is 5.5 mm in diameter, located along the optical axis of the eye, and is responsible for high-acuity vision. The area of highest visual acuity in the macula is called the fovea and is slightly off center from the optical axis of the eye. However, when fixing on an object, the image is projected onto the center of the fovea. The fovea is 1.5 mm in diameter, which accounts for approximately 5 degrees of vision.

In order for the eye to focus, the natural lens needs to change shape through a mechanical interaction with the ciliary muscle. The lens is surrounded by a lens capsule, which is attached to the ciliary body via zonules extending from the periphery of the capsule (Figure 1-4). Changes in the ciliary muscle cause the lens to relax or to be pulled taut in the elastic capsule. This causes changes in the anterior and posterior radii of curvature, allowing the eye to focus.

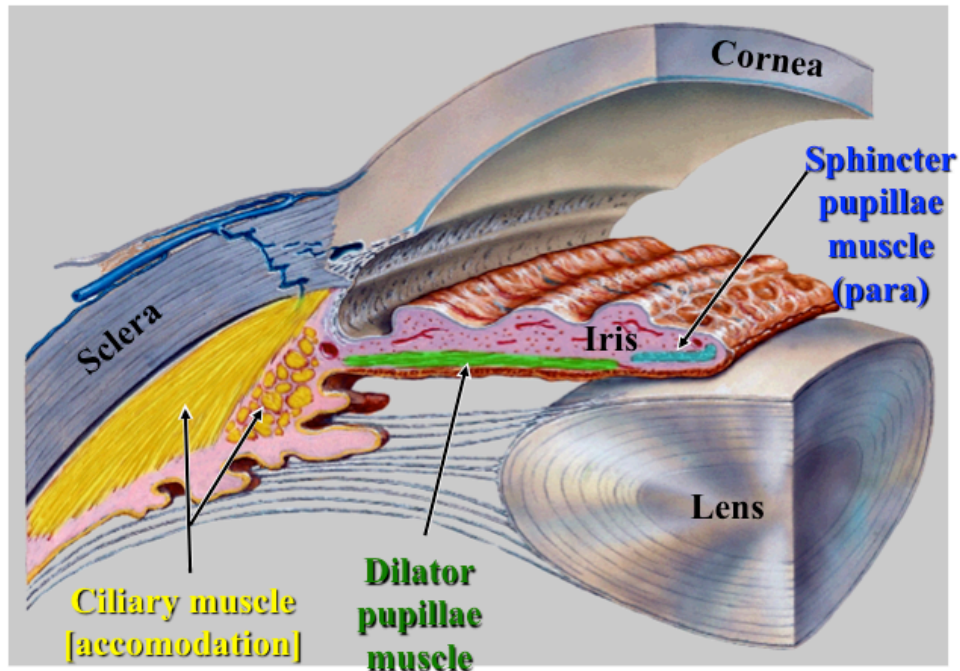


Figure 1-4. Closeup of ciliary muscle, iris, and lens

The ciliary body consists of three sections. The anterior section is known as the pars plicata and consists of 70 ciliary processes. The ciliary processes consist of vascularized stromal cores surrounded by an inner pigmented layer of epithelium and an outer nonpigmented layer of epithelium. The nonpigmented layer of epithelium secretes aqueous into the eye. The middle section of the ciliary body is the pars plana and is composed of pigmented epithelial cells and is continuous with the retinal pigmented epithelium. The nonpigmented cells on the exterior of the pars plana secrete mucopolysaccharide, a component of the vitreous. Adjacent to the pars plicata, is the ciliary muscle. This consists of three layers of smooth muscle. The majority of the ciliary muscle is an outer longitudinal layer that attaches to the scleral spur. The radial and circular muscle fibers are located adjacent to the longitudinal fibers [11].

The ciliary muscle acts in unison and is primarily innervated by the parasympathetic nervous system. Contraction of these fibers acts to move the lens forward and release tension on the zonules. Consequently, the lens rounds up, causing an increase in focal power known as accommodation.

The iris is located between the lens and the back of the cornea. It acts as an aperture to regulate the amount of light entering the eye known as the pupil. As the pupil becomes smaller, this acts to increase depth of field of the eye, which can bring previously blurry objects into focus.

The iris has an irregular and folded anterior surface, with melanocytes. The number and degree of melanin granules in the stromal melanocytes cause eye color. The posterior surface of the iris is smooth, and consists of pigmented cells to absorb incident light. The iris has two opposing muscles, which act to open and close the pupil. One smooth muscle layer forms dilator muscles, which are radially oriented (Figure 1-4) and cause the pupil to expand (mydriasis). They are innervated by the sympathetic nervous system. The other smooth muscle forms the circumferential pupillary sphincter, which is innervated by parasympathetic nerves from the third cranial nucleus and causes the pupil to constrict (miosis). Upon sympathetic stimulation, the radially oriented dilator muscles contract, causing the pupil to increase in diameter. Upon parasympathetic stimulation, the circumferential pupillary sphincter muscles contract, reducing the diameter of the pupil.

1.2 Accommodation Reflex

The accommodation reflex refers to the ability to increase the optical power of the eye by focusing from far to near. It consists of convergence of both eyes, pupillary

constriction, and contraction of the ciliary muscle. Convergence of the eyes is caused by extraocular muscles and is necessary to avoid diplopia. The pupil contracts, which causes an increased depth of field. The ciliary muscle contracts and allows the lens to round up and increase optical power.

As shown in Figure 1-5, the neural signal for accommodation consists of afferent signals from the retinal ganglion cells traveling through the optic nerve and synapsing on the lateral geniculate nucleus. The association limb of the reflex consists of cells from the lateral geniculate nucleus, which synapse with cells on the primary visual cortex, which then synapse with the visual association cortex and connections with the pretectal area. The efferent signal comes bilaterally from the oculomotor nucleus, which causes contraction of the medial rectus muscles. This leads to an inward tilt of the eye and convergence. Efferent signals from the accessory oculomotor nucleus then synapse on cells from the ciliary ganglion, which then provide parasympathetic stimulation to the ciliary body and the constrictor pupillae.

Accommodation Reflex

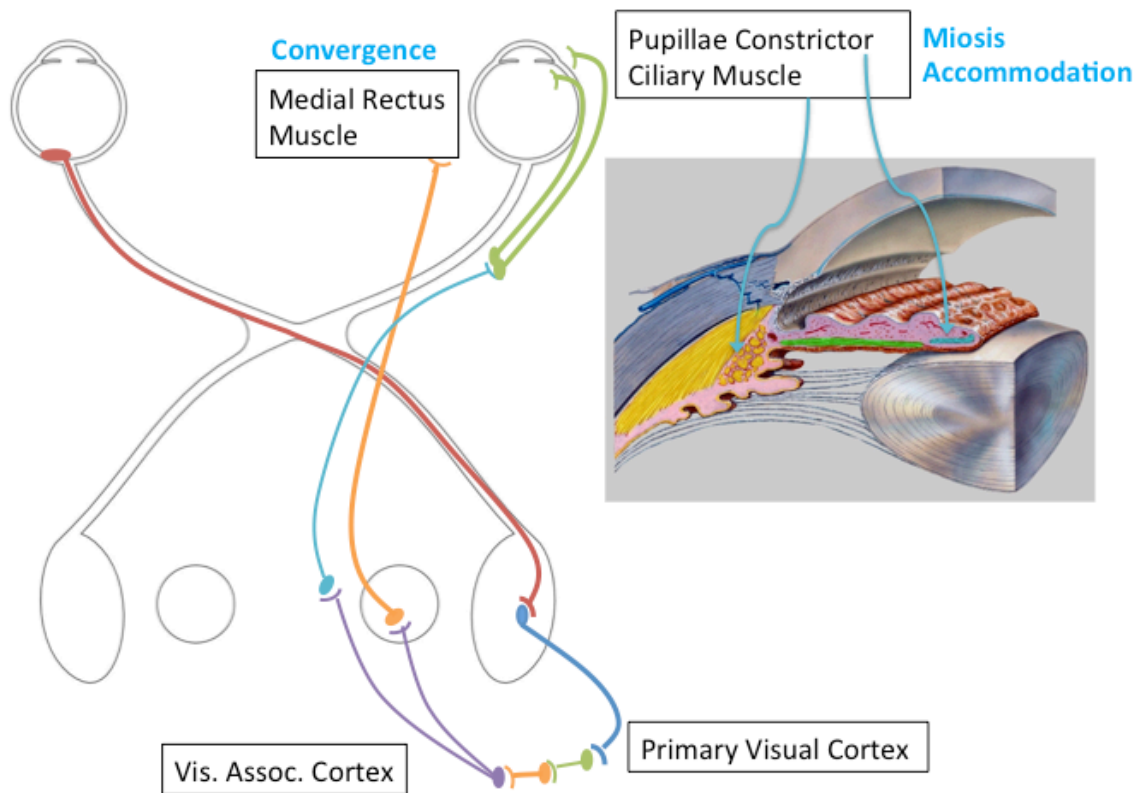


Figure 1-5. Neural accommodation reflex. Note only one side of the efferent signal is shown for clarity.

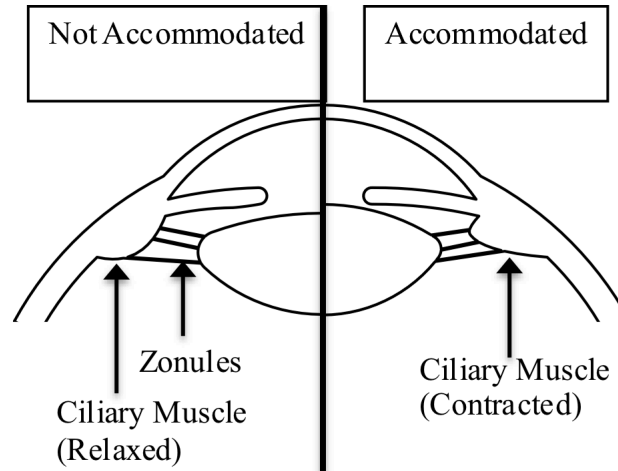


Figure 1-6. Accommodation mechanism

The focusing mechanism of the eye consists of a ciliary muscle attached to a series of zonular fibers, which connect the muscle to the lens capsule, a thin membrane that surrounds the lens. According to Helmholtz theory of accommodation, at rest the ciliary muscle is relaxed and the zonules maintain a constant tension on the lens capsule (Figure 1-6). The lens capsule transmits the force to the lens, flattening it [12]. This corresponds to a lower optical power. When the ciliary muscle contracts, it moves anteriorly and reduces its diameter, which releases tension on the lens capsule and lens. When tension is released on the lens capsule, it is able to mold the lens into a more spherical shape, causing focal power of the lens to increase [13], [14]. For a five-diopter accommodation the lens thickness increases 300 μm , the middle of the lens moves 100 μm anteriorly, the anterior surface moves towards the cornea 500 μm , and the posterior surface moves back towards the retina 50 μm [8]. During accommodation, the anterior surface of the lens changes more than the posterior surface. Dubbelman found the anterior radius of curvature of the lens changed -0.62 mm/D while the posterior radius of

curvature changed -0.13 mm/D [13]. Therefore, although both surfaces contribute to the accommodation of the lens, the anterior surface has larger changes in radius of curvature.

1.3 Pathology of the Eye: Presbyopia

Naturally, the human lens loses focusing ability with age in a process known as presbyopia. This is noticed in the fourth decade of life when eyestrain occurs during close visual acuity tasks, such as reading. Although subjectively, this often appears to be an abrupt event, the ability to focus is actually lost continually throughout life [9, 15, 16].

Presbyopia was quantified by Duane in 1912 with the push-up technique [15]. This technique consists of asking patients when a visual target becomes blurry as it is brought closer to the eye. Based on his work and subsequent work, a model for age-related accommodation has been made. A graph is shown Figure 1-7.

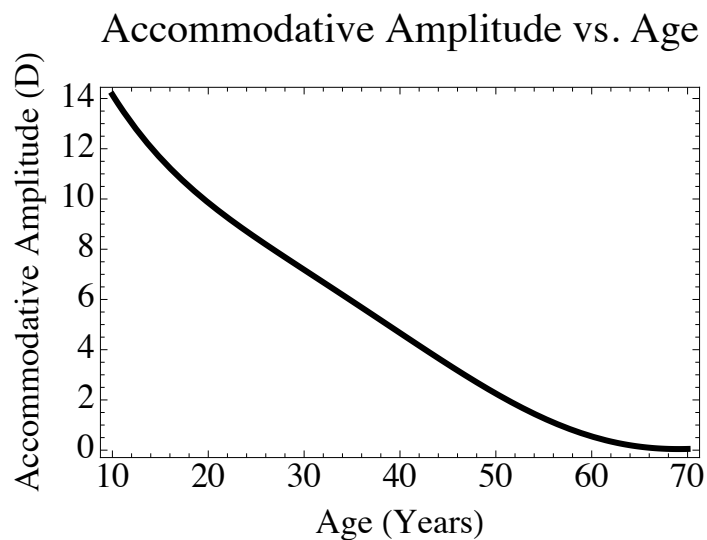


Figure 1-7. Accommodative amplitude versus age [17]

The mechanism of presbyopia is still actively being researched. There are three major theories of presbyopia: lenticular, geometric, and extralenticular.

Lenticular theory describes presbyopia as due to a progressive stiffening of the natural lens with age [18-20]. This theory states that the lens is less able to change shape under the forces applied by the ciliary muscle, and hence accommodation ability is reduced and eventually eliminated. This theory started with work by Fisher, who studied *in vitro* lenses and their ability to deform under external forces. By spinning the lens and measuring deformation he was able to show an age-related decrease in deformation, which he correlated to an increase in lens hardness. Later, Glasser developed a method to remove the focusing mechanism of a cadaver eye and apply external forces to the ciliary muscles to apply *ex vivo* accommodation, and measure the change in focal length of the lens. This work demonstrated an age-related decline in accommodation that coincided with clinical data taken by Duane (Figure 1-7). The data from Fisher correlates a decrease in ability of the lens to deform with age. In addition, Glasser demonstrates that even if there is sufficient force applied for the lens by the ciliary muscle and zonules to accommodate, it can no longer change focus. This points to a central pathology in the lens itself. Other lens stretching techniques and refinements have been developed that find similar decreases in accommodation amplitude with age and increased forces to deform the lens [21]. In addition to these studies, the basic mechanical properties of the isolated lens have been studied to demonstrate an increase in stiffness with age. These studies have shown an increase in lens stiffness with age using sectioned lenses [22, 23] as well as measurement on the intact isolated lens [24].

The geometric theories of accommodation describe a change in the geometric positioning of the lens and zonules. These theories are based on the fact that the lens continuously grows throughout life [16, 25-27]. As it becomes larger, the positioning of

the lens relative to the ciliary muscle changes. Although zonular tension increases, there is a decreased force in the radial direction. This geometric change makes the ciliary muscle ineffective at deforming the lens [28]. Therefore the focusing mechanism is unable to appropriately change the shape of the lens. Data from experiments on lens volume illustrate this theory. For example, Burd shows prior data demonstrating lens volume increasing from approximately 140 mm^3 at an age of 10 to 210 mm^3 at an age of 55 [29].

Extralenticular theories of presbyopia include reduction of ciliary muscle movement, which has been shown with MRI to occur as a part of aging. However, this reduction has been shown to occur after the age of 60, while accommodative amplitude decreases throughout life. In addition, even at age, a significant movement of the ciliary muscle has still been shown in these cases [30].

1.4 Pathology of the Eye: Cataract

Cataracts are characterized by a clouding of the natural lens, which lead to a progressive deterioration of vision. A cataract is medically treated by removing the cataracted lens and replacing it with an intraocular lens (IOL). Most commonly cataracts occur as an age-related process, with over 91% of the population having them at the age between 75-85 years [31]. Other causes can be from environmental exposures such as uv light, trauma, congenital, or related to other systemic diseases such as diabetes.

Cataracts are classified into several subtypes. Nuclear sclerotic cataracts are the most common type, and are considered a normal part of aging. The nucleus becomes dense, while the lens becomes brunescent. This can cause the iris to be displaced

anteriorly, potentially causing angle closure glaucoma. At advanced stages, the middle cortical layer of the lens may liquefy and the nucleus falls to the bottom of the capsular bag.

Posterior subcapsular cataracts are commonly in patients with diabetes, patients on steroids, or patients with a history of chronic ocular inflammation. Clinically scattered areas of opacity are seen in the lens.

Congenital cataracts often require lens replacement early in life. They have many causes, including congenital infection, retinoblastoma, and galactosemia (deficiency in enzymes breaking down galactose).

Cataracts can form at any age after injury to the eye. In many cases there is damage to the zonules, which could compromise the action of an accommodating intraocular lens.

Diabetic cataracts are due to high glucose levels, which cause a buildup of soribitol in the lens. This causes the lens to swell from an osmotic gradient. Eventually, a cataract is formed. Interestingly, aldose reductase inhibitors, which prevent glucose from being converted to sorbitol, are being evaluated as topical eye drops to prevent cataract formation in diabetic patients [32].

1.5 Lens Replacement

Lens replacement surgery, also generally known as cataract surgery, occurs most commonly after formation of a cataract. Cataract surgery is typically an outpatient procedure [31, 33]. Lens removal is most often performed using ultrasonic emulsification with a surgical handpiece known as phacoemulsification. The procedure begins with eye drops to dilate the pupil (mydriasis) and a sedative. A retrobulbar block is used to eliminate sensation and motion of the eyes. Next, the eye and skin around eye are cleansed and a sterile covering around the eye and head is placed. Then, a small incision is made through the cornea into the anterior chamber. This incision is normally 3 mm or smaller because smaller incisions help healing and prevent postoperative astigmatism. Viscoelastic is injected into the anterior chamber of the eye to stabilize the chamber.

Next, the natural lens is exposed to allow it to be removed from the lens capsule by tearing a circular hole in the anterior lens capsule. This procedure is known as a capsulotomy or capsulorhexis [34]. The size and shape of the capsulorhexis is important for placing the IOL. If the hole is irregular or too large, the IOL will be difficult to place accurately.

At this point, the surgeon breaks the lens free from the lens capsule using hydrodissection, removing any adhesions between the two. Then ultrasonic power is used to break up lens and aspirate fragments in a procedure known as phacoemulsification. During this process, first the nucleus of the lens is removed, followed by the cortex. The cortex of the lens may adhere to the surrounding lens capsule. If it is not removed, lens epithelial cells can proliferate after the procedure and cause posterior capsule opacification. In addition, during the phacoemulsification, the surgeon needs to be careful

to avoid damage to the posterior capsule, which would remove support for the IOL placement and may allow lens fragments to fall into the posterior chamber of the eye.

Then, the intraocular lens is injected into the capsule. The intraocular lens is then placed into the eye with a lens injector. IOLs are held in place by several haptics that press against the equatorial regions of the lens capsule. Once the lens is positioned, it is cleaned from any residual viscoelastic. The corneal wound is closed, usually without suturing. The patient is left with a protective eye shield, which is worn while sleeping for one week post-surgery.

The most common complication from cataract surgery is posterior capsular opacification (PCO) [35]. In addition, it is the most common reason for loss of vision after cataract surgery [36]. After removal of the natural lens, the surgeon attempts to remove all remaining lens epithelial cells in the periphery of the lens capsule. However, this is often technically difficult if not impossible. Therefore, if residual lens epithelial cells remain, they undergo a myofibroblastic or fibroblastic-like change and migrate to the posterior surface of the capsule. This causes the posterior capsular bag to opacify [37]. To alleviate this condition, the posterior capsule can be removed after surgery by use of a neodymium-doped yttrium aluminum garnet (Nd:YAG) laser operating at 1064 nm.

1.6 Current Intraocular Lens Technology

There are several types of intraocular lenses currently being developed or used. The most common IOLs are monofocal lenses, which provide a single focal length and no accommodation ability. Multifocal lenses provide simultaneous near and far vision,

increasing depth of field. Accommodating IOLs have a variable focus and can be categorized into vaulting lenses, dual-optic IOLs, and flexible lenses. Vaulting lenses consist of a single lens that moves anteriorly and posteriorly due to motion of the ciliary muscle. Dual-optic IOLs consist of two optics which change position relative to each other due to motion of the ciliary muscle. Flexible lenses use the ciliary muscle and lens capsule to exert a shape change on the optics.

Table 1-2 shows the different technologies of intraocular lenses.

Monofocal IOLs have been used in ophthalmology since 1949 [38]. Since then, the technology has evolved and there are many types of IOLs available on the market today. The first IOLs were made of PMMA, a rigid plastic material. These lenses were nonfoldable, requiring a large surgical incision. This type of incision was approximately 5-7mm, and as a result, sutures were used to close the wound.

Foldable monofocal IOLs are made of flexible materials. This allows the lens to be folded or compressed before insertion into the eye. Two surgical techniques are used to insert this type of IOL. Special forceps may be used or an inserter that folds and rolls the IOL for delivery into the capsule. When the foldable lens is placed in position, it opens up and retains its original configuration. Foldable IOLs allow a small incision for implantation. This is advantageous for several reasons including safety, less trauma to the eye, and less postoperative astigmatism. Foldable IOLs are made of materials including silicones and acrylics. These materials have shown superior safety and biocompatibility as an implantable material.

Monofocal lenses can provide excellent visual acuity, and the insertion of them is standard. It is routine for surgeons to determine accurate base power and good refractive

outcomes are typical. To correct for astigmatism, toric IOL designs were made. This type of IOL has an axis, which must be aligned to match the axis of the patient's astigmatism. The lens must be in proper alignment for the patient to have clear vision. In order to maintain proper alignment, this type of IOL has a plate haptic IOL design, with four pod anchors. This placement design prevents lens rotation from occurring when the capsule contracts or expands.

Currently most monofocal intraocular lenses have a square edge on the posterior surface that interacts with the posterior lens capsule. This is to cause an angular discontinuity in the lens capsule, which is thought to prevent or reduce lens epithelial cells from crossing from the periphery of the lens to the center [39] [40]. Therefore, this is used to reduce the postoperative incidence of PCO.

Table 1-2. Current intraocular lens technology

	Monofocal	Multifocal	Vaulting	Dual-optic [41] [42]	Flexible Lens [43]
Accommodation	No	No	1-2 D	2-3 D	> 2 D
Visual Acuity	Excellent	Halos, Glare, MTF low	Unknown	Unknown	Unknown
Incision Size	2-3 mm	2-3 mm	2-3 mm possible	~ 3.8 mm	Varies
Adjustable after Implantation	N	N	N	N	N
FDA Approved?	Y	Y	Y	Phase III	N

To provide patients with depth of focus, the multifocal lens was developed and FDA approved. Multifocal lenses contain two or more separate foci. Therefore, both an in focus and out of focus image are projected on the retina simultaneously. The brain separates the in focus image from the out of focus image. Therefore, it is possible to have

both near and far vision. A greater degree of spectacle independence has been seen with multifocal lenses than traditional monofocal lenses. However, there is a decrease in contrast sensitivity [44] and users often report having flare, halos and glare [45].

To leverage the optical quality of a monofocal lens and provide a limited amount of accommodation, vaulting type intraocular lenses were designed [46-48]. These move in the anterior and posterior direction with the motion of the ciliary muscle. This motion causes a slight amount of accommodation. Typically this is from 0 to 2 diopters. Like a monofocal lens, they can be inserted through small incisions. In addition, they retain the optical quality of a single lens.

The dual-optic design was made to provide higher levels of accommodation than the vaulting type lens [49] [50]. The most prominent of these designs is the Synchrony Lens, which is a dual-optic silicone accommodative IOL. It has two lenses that are separated by a spring-activated mechanism. The anterior lens is a +32 diopter optic and the posterior optic is a variable negative lens with an optical power that depends on the required power of the patient for emmetropia. Motion of the ciliary muscle causes the distance between the two lenses to change and provides accommodation. However, there are a few disadvantages with this design. The Synchrony lens is large, requiring a large surgical incision for implantation. This has the potential to result in postoperative astigmatism and reduced visual acuity. Also, base power is not adjustable after implantation. Other concerns include biocompatibility and lens integrity over time, such as the issue with development of opacification between the two optics [51]. The Synchrony Lens is currently under FDA review.

Flexible lens IOLs have a surface that changes curvature in response to motion of

the ciliary muscle. Therefore, these have the potential to provide high levels of accommodation. Several groups have used a fluid inside a lens to change the shape of the lens [52]. These lenses often require a large surgical incision to be placed.

Another approach taken is to refill the natural lens capsule with uncured polymers that eventually cure. Delivery of the polymers can be inserted directly into the lens capsule [53-57] or into an endocapsular balloon, which sits inside the lens capsule. However, for the endocapsular balloon approach, a filling tube was used, making the surgical approach complex [58, 59].

In all these approaches, base power of the lens is not adjustable after implantation. Therefore, if base power is not correct, a secondary vision correction may be required.

Although currently obtaining correct base power in a monofocal intraocular lens is routine, correct base power with an accommodating intraocular lens is inherently more difficult. This is because an accommodating intraocular lens requires a large optical power adjustment from a small motion of the ciliary muscle. Not only does the correct refractive power need to be determined, but the fit of the lens relative to the specific geometry of the ciliary muscle, zonules, and lens capsule complex needs to be defined as well [49].

1.7 Conclusion

To cure presbyopia, lens replacement is a viable option. Presbyopia research has indicated that the ciliary muscle continues to contract throughout life. In addition, there is substantial evidence that changes in the lens are a significant factor for a loss in ability to focus. Therefore, a replacement lens that interacts with the ciliary muscle through the

lens capsule would be expected to perform in a manner similar to the youthful human lens.

Current work on most accommodating intraocular lenses has not been FDA approved, and therefore, little data is available regarding optical quality, percent of patients who have emmetropia after placement of the lens, and clinical accommodation levels. Emmetropia refers to the ability to focus sharply on an object at far distances. In addition, many of these designs require large surgical incisions, which may cause postoperative astigmatism and worse wound healing. Many of the current designs do not have the ability to adjust base power to correct for emmetropia after the surgery.

Because accurate base power, sufficient accommodating amplitudes, small surgical incision, and optical clarity are inherently difficult to achieve with any of the existing accommodating or multifocal IOLs, there is a need for a new IOL design to alleviate presbyopia.

2 SILICONE AS A BIOMATERIAL

2.1 Introduction

Silicones are used as a biomaterial based on their flexibility, elongation, and proven biocompatibility. They consist of a repeating Si-O backbone and two organic groups, covalently bonded to the Si group. Polydimethyl siloxane, PDMS, is a common silicone and has two methyl groups covalently bonded to the silicon atom (Figure 2-1).

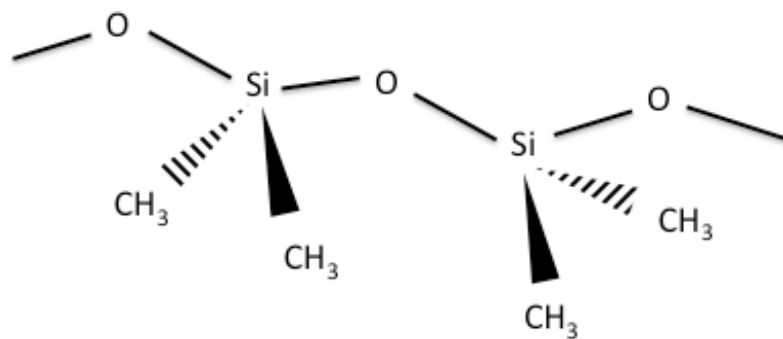


Figure 2-1. PDMS molecule

Many of the material properties of silicone, including flexibility, are largely due to the Si-O backbone. The length of a Si-O bond is long at 1.64 angstroms, which results

in low steric interference. In addition, the angle of the Si-O-Si bond is 147 degrees, which allows rotation around the bond and gives the molecule flexibility [60]. Because the atoms are free to move, silicone has a low glass transition temperature. However, the chain flexibility and low intermolecular forces of silicone also make it permeable to gases and some liquids.

2.2 Crosslinking Silicone Elastomers

To form an elastomer, the linear siloxanes have to be crosslinked together to form a covalently bonded network. Crosslinking occurs when there are functional silanes in the polymer, which allow neighboring polymers to react with each other.

Commonly silicones are crosslinked with a variety of methods. These include using a moisture cure at room temperature. For example, acetoxysilane is converted to acetic acid in the presence of humidity, which acts as a catalyst, allowing hydroxyl terminated siloxanes to react with silanes. Heat activated radical cure (HTV) silicones use alkyl peroxides as catalysts. These react with the hydrogen in methyl groups or with a vinyl group in the siloxane to form crosslinking [61].

Biomedical silicones often use an addition cure with a transition metal catalyst, such as platinum. This is because these addition cure systems do not produce by-products after curing. Typically, one part contains a silicone hydride, while the other contains a silicon-vinyl group. The catalyst is present in one of the parts and when mixed together, the reaction occurs at low temperatures. A diagram of this process is shown in Figure 2-2.

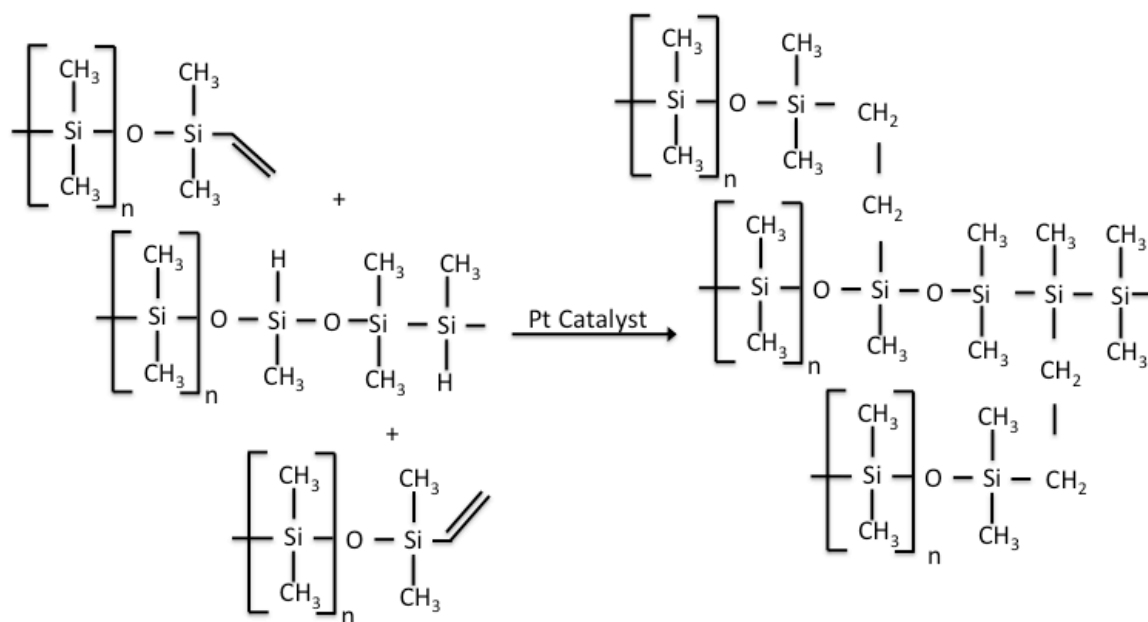


Figure 2-2. Platinum-catalyzed crosslinking reaction

For platinum-catalyzed addition cure the amount of crosslinking is related to the amount of curing as well as the number of vinyl groups and hydride groups which are available to crosslink. When there is an excess of vinyl groups and curing is complete, then the crosslink density will be determined by the amount of hydride groups. Likewise, if there is an excess of hydride groups, the number of vinyl groups will determine the crosslinking amount. The highest crosslinking density occurs when the hydride and vinyl groups are stoichiometrically matched.

During the curing process, linear PDMS strands are initially not crosslinked, and form a viscous fluid. Then as crosslinking occurs, the strands become intertwined and viscosity increases. Finally the process of gelation occurs as the viscosity approaches infinity and an elastic solid is formed. The modulus of elasticity of the solid is related to the crosslink density, which higher crosslinking corresponding to a higher modulus.

2.3 Resins and Fillers

In addition to a crosslinked siloxane backbone, silicone elastomers often also contain reinforcing fillers, extending fillers, curing agents, pigments, and processing aids. Fillers are used to increase mechanical strength and increase hardness as well as alter electrical properties, and alter silicone tackiness.

Fume silica is used to reinforce the mechanical properties of many silicones [62-64]. For example, it can be used to increase the modulus of elasticity, wear resistance, tear resistance, and surface hardness of the elastomer. Fumed silica is amorphous and small particles fuse in the semimolten state to form aggregates, which are intertwined, hydrogen bonded, or covalently bonded to the PDMS chains. This crosslinking or bonding causes an increase in strength of the elastomer. In addition, the molecular interactions between the silica filler and the PDMS backbone affect the mobility of the molecules and crystallization behavior.

2.4 Biocompatibility

Silicone has been a proven material for biomedical implants. Silicone has been used for biomedical applications and implants throughout the human body. Applications include maxillofacial implants, contact lenses, intraocular lenses, toe joints, hip implants, breast implants, and tracheal stents [65, 66]. In addition, silicone has been used for transdermal drug delivery. Its toleration in the body is due to its hydrophobic nature as well as its mechanical properties, including flexibility and elongation.

Biocompatibility of silicone can be affected by side groups on the backbone as well as residual molecules from processing, including catalysts and by-products from the reaction. Often processes such as extraction are performed on the implant to remove impurities from the silicone to ensure biocompatibility.

2.5 Implant Stability in the Body

The body environment affects implants in several ways. First, the body often mounts an immune response, known as the foreign body reaction. Second, the implant must operate at the temperature and mechanical loading conditions associated with a living organism. Finally, the implant must be stable to reactions that occur from the immune system and bodily environment.

The body reacts to an implant and forms a foreign body reaction. This begins with an immune response from the surrounding macrophages and T-cells. During this response, macrophages often coalesce and become giant cells. In the later stages of the foreign body reaction, a fibrous capsule is formed around the implant, walling it off from surrounding tissue. The amount of foreign body reaction depends on the tissue / location in the body, the biocompatibility of the material used, and the surface roughness of the implant.

Once implanted, the device must operate at the internal temperature (37 °C) and tolerate the body's mechanical loading. For example, prosthetic joints are cycled through strains as the joint moves and pacemakers need to move as the heart beats.

Because the body is a physiological environment, the implant will come into contact with enzymes, oxidizing agents, proteins, and other physiologic molecules.

Oxidizing agents and enzymes are secreted by immune cells such as macrophages. These reactions often degrade aromatic rings, alcohols, ethers, and phenols [60]. However, silicone is relatively stable against oxidation in the body. Proteins from the local environment or the immune system may adhere to the implant. In addition, calcium may deposit on the surface and form a plaque around the implant. This has been shown to happen in many implants including silicone breast implants.

2.6 Diffusion of Silicone Oil and Extraction

Low-molecular-weight silicone oils can diffuse through silicone implants if they are not crosslinked to surrounding molecules. Most notably, diffusion of low-molecular-weight silicone oil (especially D4–D8) through the shells of breast implants caused a series of implant recalls. To prevent this, later generation implants used a permeation barrier made of fluorosilicone to prevent diffusion. This design relies on the low surface energy of the fluorosilicone to prevent diffusion of low-molecular-weight silicone oligomers. Clinically, fluorosilicone-coated breast implants have demonstrated better biocompatibility, less of a foreign body reaction, and less silicone bleed than traditional implants.

Low-molecular-weight silicone oils arise inside the PDMS matrix from uncrosslinked remnant cyclic siloxane oligomers. These unreactive species cannot not cross link with surrounding silicone molecules and remain trapped within the silicone matrix. Consequently, they slowly released from the silicone matrix, especially if the crosslinking distances of the PDMS molecules increase due to swelling of the silicone. Swelling may occur from uptake of phospholipids into the silicone matrix. For silicone

intraocular lenses, low weight molecules are removed in an extraction step as part of the device manufacturing to prevent leeching.

2.7 Silicone Base Material: NuSil MED4-4210

The base silicone used for building the accommodating intraocular lens is chosen based on its biocompatibility, its modulus of elasticity, optical clarity, viscosity, and elongation. A USP class VI material is required for an implantable device, therefore only these materials were examined for use in the implant. The cured modulus of elasticity is chosen to be similar to the existing lens capsule (1 MPa) [29]. In addition, because the device is a lens, the silicone must have good optical transparency in the thicknesses used for the lens. Finally, the manufacturing process dictates a spin coat of the material, followed by a temperature cure. This requires a low enough viscosity to allow a thin 30 μm coating at normal spin coating speeds (up to 10 k rpm), but a high enough viscosity so that the silicone is retained to the side of the mold for a period of at least 15 minutes after spin coating. Elongation is dictated by the material's ability to flex during accommodation as well as its ability to be injected into the eye through a delivery device smaller than 2 mm in diameter. Therefore, ultimate elongations of over 100% were considered to have an adequate magnitude of safety.

Based upon these requirements, NuSil MED4-4210 was chosen. This is a USP VI silica reinforced silicone with an accessible Master Access File with the U.S. Food and Drug Administration. Cytotoxicity results, in vitro hemolysis, USP and ISO systemic toxicity extract, ISO intracutaneous study extract, ISO muscle implantation studies, genotoxicity, USP pyrogen studies, and maximization sensitization studies conducted for

the FDA are located in APPENDIX A: Biological Testing Data, MED4-4210. A full spectrum of tests conducted on the material, for which safety files are available is located in APPENDIX B: Index of Silicone Elastomer Testing, MED4-4210.

The modulus of elasticity is 1.3 MPa, which is similar to the lens capsule. The base viscosity of part A is 90 k cP and part B 5 k cP with a 10:1 mixed viscosity of 82,000 cP [67] which has been experimentally determined to provide a uniformly thick device. In addition, the work time of the silicone is 2.5 hours, which gives adequate time to mix, de-gas, spin coat, and then cure onto the device. The ultimate elongation of the device is tabulated at 450%, well above the required elongation of the device.

2.8 Experimental

Material properties of MED4-4210 were measured to evaluate suitability as an accommodating intraocular lens implant. The glass transition temperature was measured to ensure it was low compared with body temperature. The curing schedule of the silicone was determined by evaluating modulus of elasticity versus cure time and temperature. Repeatability of hand mixing was evaluated to estimate deviation in the mechanical properties base on manufacturing. In addition, the effect of part A to part B was evaluated by monitoring modulus of elasticity as the part A and part B ratios were changed. Creep and stress relaxation testing was completed to demonstrate the material is suitable for repeated load situations. Finally, the diffusion characteristics of silicone oil relative to the silicone were measured.

2.9 Glass Transition Temperature

Amorphous polymers exhibit different material properties at room temperature. Some, like polystyrene are hard and brittle, while others, like silicone, are rubbery and elastic. The difference between these two materials has to do with the glass transition temperature of the two materials. Below the glass transition temperature, T_g , amorphous polymers are in a glassy state, while above T_g , the material is in a rubbery state. The T_g of polystyrene is above room temperature, so it acts as a glass, while the T_g of silicone is well below room temperature, allowing it to act as a rubber. It should be noted that the T_g is not a change in state, but a transition. Therefore, the change between glassy and rubbery is not abrupt and there is a transition region between the two states.

The concept of free volume is useful to understand the glass transition temperature. The free volume is defined as the unoccupied space in a polymer, which is due to disordered chains and inefficient packaging of chains [68]. At temperatures above T_g both free volume and molecular motion increase with temperature. In this rubbery regime coordinated segmental motion of the polymer leads to the polymer's flexibility, reduced Young's modulus, and flow. Segments of molecules can jump leading to polymer flexibility, the uncoiling of molecules leads to elasticity, and translation of entire molecules leads to flow. The increased mobility of the polymer leads to a reduced Young's modulus. As temperature is cooled, eventually, the polymer chains are immobilized and coordinated segmental motion is no longer possible. This point is the glass transition temperature. As temperature is further decreased, there is no room for additional decrease in free volume, and it remains constant. Due to limited motion of the

polymer chains the material exhibits rigidity, an increased Young's modulus, and brittleness.

Above T_g a melting point is reached in some polymers. In this phase transition, there is large-scale slippage between molecules allowing them to flow across one another.

Figure 2-3 demonstrates the modulus of elasticity of a material as temperature is increased. In the glassy regime, the Young's modulus is high. As the glass transition temperature is reached, there is a sharp decrease of the modulus of elasticity, which occurs throughout the glass transition region. Finally, there is a rubbery region above the glass transition region.

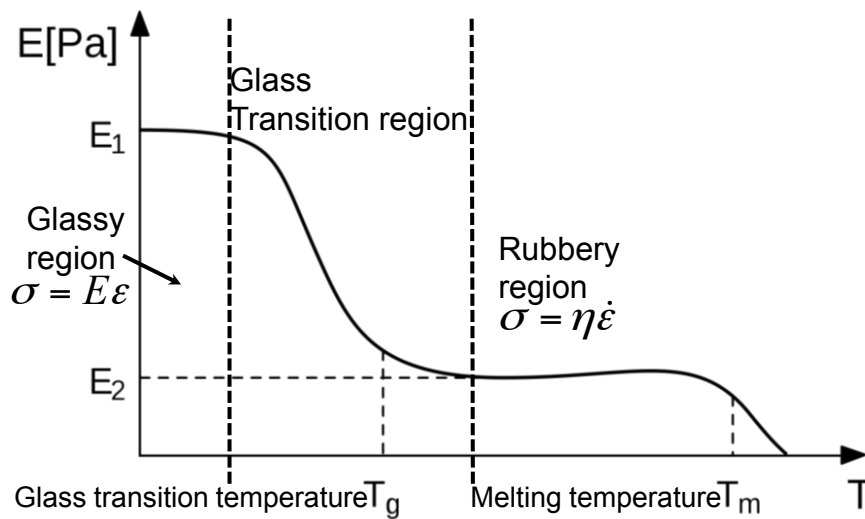


Figure 2-3. Glass transition temperature diagram

2.10 Dynamic Mechanical Analysis

To measure the glass transition temperature, a dynamic mechanical analysis (DMA) machine was used. The principle of the machine is to provide a sinusoidal stress on the sample and monitor the resulting strain on the sample. Strain in phase with the stress is due to elastic behavior of the material, while strain out of phase is due to a viscous behavior of the sample. By monitoring the in phase and out of phase strain as temperature is ramped, it is possible to determine how the material is changing with temperature and therefore determine glass transition temperature.

To understand this mathematically, the stress applied by the machine is given as

$$\sigma(t) = \sigma_o \sin(\omega t)$$

where σ is stress applied as a function of time, σ_o is the amplitude of stress applied, ω is the oscillation frequency, and t is time. For a material that exhibits Hookean characteristics, the resulting strain, ε , will be in phase with the stress and is expressed as

$$\varepsilon(t) = E \sigma_o \sin(\omega t) = \varepsilon_o \sin(\omega t)$$

where E is the Young's modulus of the material and ε_o , the amplitude of strain, is equal to $E \sigma_o$. However, if the material is purely viscous, then the stress is proportional to the strain rate and can be written as

$$\varepsilon(t) = \eta \omega \sigma_o \sin(\omega t + \frac{\pi}{2})$$

where η is the viscosity of the material. Note that this term is out of phase with the term corresponding to the Hookean material.

The DMA machine records the input stress and output strain along with the phase lag, δ , between the two signals. Using trigonometry, the resulting strain measured from the machine can be expressed as a combination of the viscous and Hookean terms

$$\varepsilon(t) = \varepsilon_o [\cos\delta \sin(\omega t) + \sin\delta \cos(\omega t)]$$

Based on this equation, the in phase, ε' , and out of phase, ε'' , amplitude of strain can be expressed as

$$\varepsilon' = \varepsilon_o \sin\delta$$

$$\varepsilon'' = \varepsilon_o \cos\delta$$

or expressed as a complex number

$$\varepsilon^* = \varepsilon' + i\varepsilon''$$

The in phase term can be viewed as the storage term, while the complex term is viewed as the loss term of the strain. Likewise, the storage modulus, E' , and loss modulus, E'' , can be calculated from ε' and ε'' . The tangent of δ , $\tan \delta$, represents how well the material returns energy (i.e., the ratio of the storage modulus to the loss modulus) and is often used to determine the glass transition temperature of the material. At the glass transition temperature, there is a peak seen in $\tan \delta$ that is often used to identify the glass transition temperature.

From the discussion there are a number of important things to note. First, $\tan \delta$ is independent of sample geometry, which prevents small variation in sample dimensions from affecting the measurements of glass transition temperature of samples. Secondly, although storage modulus measures the elasticity of a sample, it is not the same as Young's modulus measured with a stress strain curve. This is because Young's modulus is nominally calculated over a range of stresses and strains while E' comes from a single point on the line, often at small displacement. In addition, the testing parameters are different, with the DMA test being done in oscillation while the stress/strain curve is tested by applying a constant stretch to the material [69].

From DMA experiments, T_g can be reported several different ways including the onset or peak of the $\tan \delta$ curve, or drop in the storage modulus curve. In addition, T_g can be measured with different machines. Differences in the way T_g is reported as well as differing measurement techniques lead to differing measured values of T_g .

For example, measurements of T_g using differential scanning calorimetry (DSC) will differ from T_g measurements using DMA. In addition, scanning at different oscillation frequencies in a DMA will also change the values. Therefore, to compare measurements of T_g , the experiments should use identical methods of reporting T_g as well as identical measurement techniques. For frequency measurement in specific, it is ideal to measure the sample at its predicted operating value. However, this is often difficult to do, and often a frequency of 1 Hz is used to estimate a static case. Practically this has been shown to be a good estimate [69].

Although it may seem surprising that T_g value changes with measurement technique, it makes sense when glass transition temperature is considered. Glass

transition temperature is a range of behavior that is assigned a single temperature. Therefore, the measurement technique sets a point in that temperature range to characterize it. These points inside the region differ based upon what criteria are used to classify the point. For example, the onset of a decline in Young's modulus may be used. This point is in the transition region. However, it is different than the point associated with the peak of the $\tan \delta$ curve. Both measurement techniques are within the glass transition region but point to different aspects of the transition.

2.11 Glass Transition Temperature of MED4-4210

Glass transition temperature of MED4-4210 was determined by use of dynamic mechanical analysis (TA Instruments Q800) using the peak of the $\tan \delta$ curve to be compared with prior literature on a similar silicone elastomer as well as onset of the decline of the storage modulus. All experiments used a frequency of 1 Hz with a preload was 0.2 N to ensure the sample was taught, amplitude of oscillation was 20 μm , and the temperature scan was conducted from -150 to 30 $^{\circ}\text{C}$ at 3 $^{\circ}\text{C}$ per minute.

Figure 2-4 shows an example curve with $\tan \delta$ and storage modulus plotted versus temperature. Two peaks in $\tan \delta$ are seen in this figure. The nature of the peaks was determined by reviewing literature on MDX4-4210, an almost identical silicone elastomer with a fumed silica filler. From the literature, Stathi et Al. found two peaks in $\tan \delta$ to be at -113.36 $^{\circ}\text{C}$ and -34.87 $^{\circ}\text{C}$, referring to the former as a glass transition peak and the latter as a melting of the crystalline phase [70]. Their experimentation manner was similar to the techniques used in this study, with DMA operated at a frequency of 1

Hz and characterized by the peak of the Tan δ curve. The melting of the crystalline phase transition was demonstrated in prior work by Stevenson et al. with calorimetry [71]. Therefore, based on this literature, the higher temperature transition peak is referred to as a melting of the crystalline phase, T_m , while T_g is referred to as lower temperature peak.

Figure 2-4 also shows locations and values for the transitions based on the Tan δ peak and onset of the decline of the storage modulus. As described before, these two methods give different values of T_g for the same glass transition temperature profile. In addition, an increase in the storage modulus is seen before melting of the crystalline phase in Figure 2-4. This is not unusual and corresponds to a rearrangement of the molecules as they have increased mobility [69].

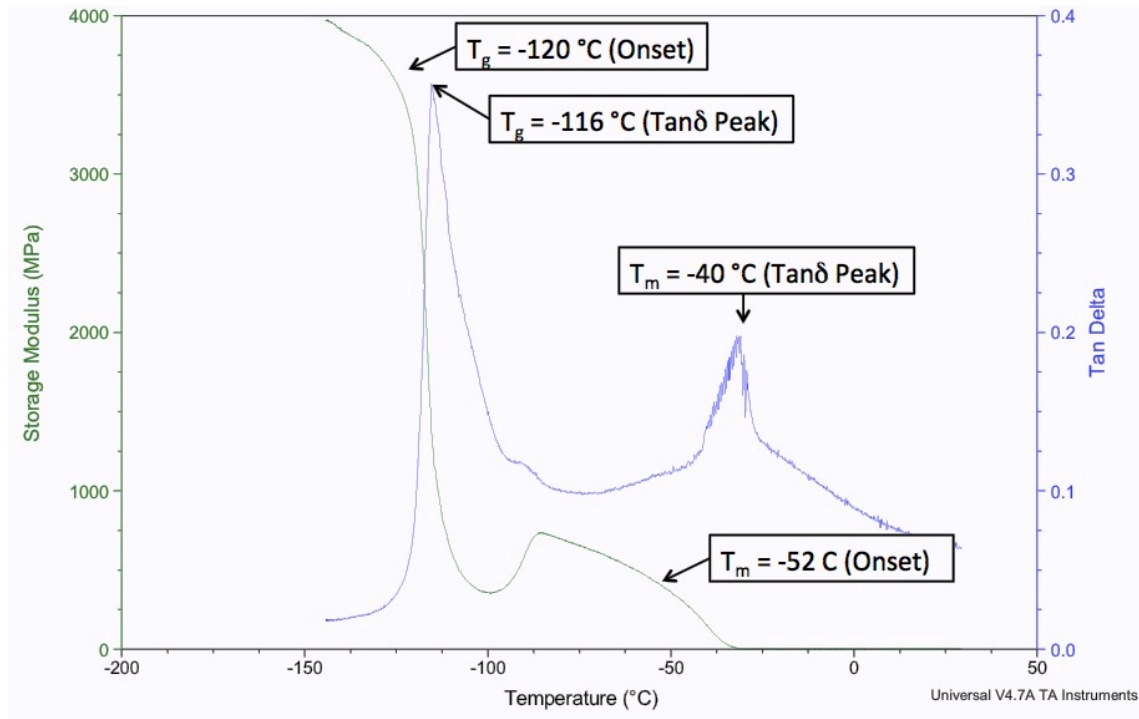


Figure 2-4. Storage modulus and Tan δ versus temperature for a sample of MED4-4210. The lower temperature peak corresponds to a glass transition temperature, while the peak seen at $-40\text{ }^{\circ}\text{C}$ corresponds to a melting of the crystalline phase, denoted T_m . Two methods are shown, the onset of the decline of the storage modulus, and the peak of the Tan δ curve. Although referring to the same transition region, the two methods of measurement produce different values.

DMA was performed on samples with different curing schedules to ensure there were no significant effects on glass transition temperature relative to curing in nominal ranges. Curing schedules of $150\text{ }^{\circ}\text{C}$ and 15 minutes, $150\text{ }^{\circ}\text{C}$ and 60 minutes, $100\text{ }^{\circ}\text{C}$ and 1 hour, and $25\text{ }^{\circ}\text{C}$ and 24 hours were all tested. Average values for T_m and T_g are shown in Table 2-1. T_g values of Tan δ varied from $-114.2\text{ }^{\circ}\text{C}$ to $-115.9\text{ }^{\circ}\text{C}$. T_m values of Tan δ varied from $-25.9\text{ }^{\circ}\text{C}$ to $-31.8\text{ }^{\circ}\text{C}$. With all transitions much below operating temperatures, the MED4-4210 will operate in the rubbery region, which is desirable for the mechanical

properties of the lens. Table 2-1 also indicates that in the range of curing schedules T_g and T_m remains low.

Compared with prior literature of MDX4-4210, the silicone that was replaced with MED4-4210 for long-term implantation, there is similarity between the two transition temperatures. Stathi et al. determined a T_g of -113.36°C versus our measured value of -114.2 and -115.9°C . Likewise Stathi's determination of T_m of -34.87°C is close to our measured value of -25.9 to -31.8°C [70]. This similarity of results illustrates that the two silicones, although made by different manufacturers, have similar glass transition temperatures as well as a similar temperature for crystalline melting.

Table 2-1. Glass transition temperature peaks in cure schedules for MED4-4210. Between 3 and 5 samples were measured and averaged for each point.

	T_g		T_m	
	Tan Delta	Onset Point	Tan Delta	Onset Point
150 C, 1 hr	-115.9	-120.5	-29.6	-53.0
150 C, 15 min	-115.9	-120.8	-31.8	-52.6
100 C, 1 hr	-115.3	-120.4	-30.7	-54.2
25 C, 24 hrs	-114.2	-121.1	-25.9	-52.3

2.12 Curing Schedule

In order to test optimal curing of silicone elastomers, silicone was cured under various temperatures and times while modulus of elasticity was measured at room temperature. At maximum crosslinking, a maximum modulus of elasticity is expected. Therefore, maximum crosslinking was assumed to happen when the material was completely cured.

A wafer coated with parylene was spin coated with an uncured MED4-4210 elastomer. After spin coating, the wafer was broken into four pieces, and each piece was cured in a different temperature oven. Curing intervals of 15, 30, 60, 90, and 120 minutes were used at temperatures of 80, 100, and 150 °C. After each curing time, a sample of the silicone was cut from the wafer for subsequent analysis on the DMA.

Samples were 285 μm thick x 5.5 mm wide. DMA testing occurred at a strain rate of 1 % per minute for a total strain of 10 % in air with the chamber at body temperature, 37 °C. The modulus of elasticity was determined as the slope from 0 to 10 % strain on the elongation curve. A graph of the data is shown in Figure 2-5 with corresponding tabulated values in Table 2-2.

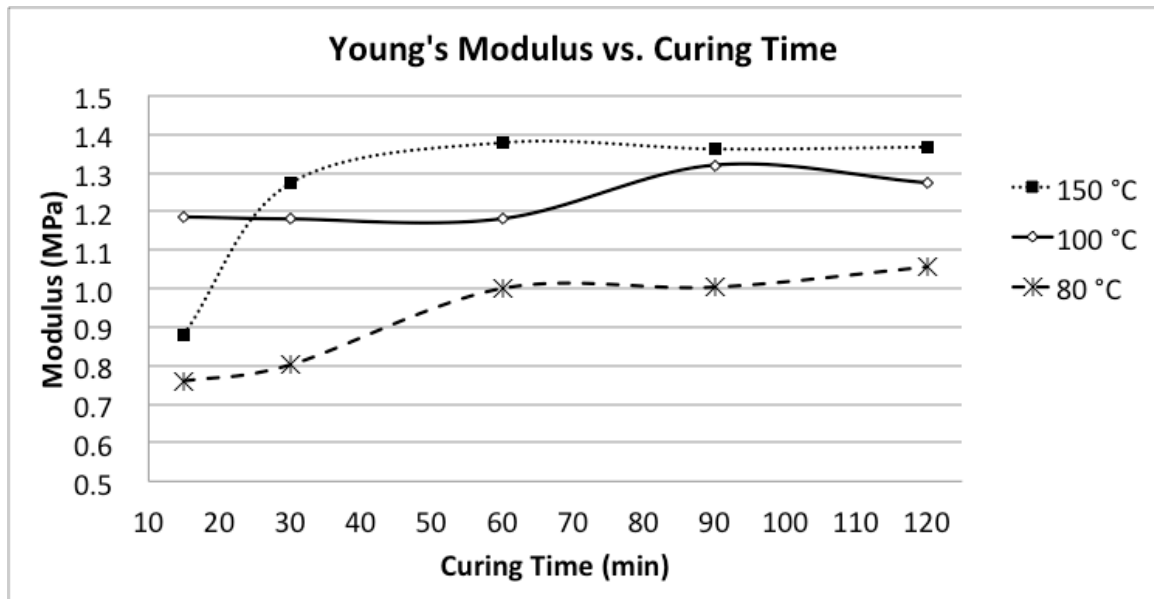


Figure 2-5. Young's modulus versus curing time for Nusil MED4-4210 at different curing temperatures

Table 2-2. Tabulated values of Young's modulus at various curing conditions

Modulus of Elasticity (MPa)					
Temperature	Time (min)				
	15	30	60	90	120
80 °C	0.76	0.80	1.00	1.00	1.06
80 °C	0.75	0.82	1.00	1.03	1.07
100 °C	1.19	1.18	1.18	1.32	1.27
150 °C	0.88	1.27	1.38	1.36	1.37

From the data, modulus of elasticity increases from a minimum of 0.75 MPa at 80 °C and 15 minutes to a maximum of 1.38 MPa at 150 °C and 60 minutes. Young's modulus increases with both cure time and cure temperature. Young's modulus levels out after 60 minutes for all samples.

One deviation from the general trend of higher modulus with higher temperature is seen at 150°C and 15 minutes. This discrepancy may have been caused by slight differences in the rate of cooling of the samples once removed from the oven, or from differences in convection coefficients from the differing ovens.

The curing data presented here can be used to determine a cure schedule for the silicone. At 150 °C the modulus reaches a maximum value of 1.38 MPa at 60 min. Within 30 minutes, the samples are close to maximum modulus at 1.27 MPa. Therefore, based on this data, curing of silicone elastomer should be done at 150 °C for 60 minutes for maximum curing.

2.13 Repeatability of Mixing

To determine the batch-to-batch variation in silicone used, a series of five wafers were prepared separately and modulus of elasticity was measured. Silicone was mixed in

a ratio of 10:1 part A to part B by hand for one minute. Silicone was poured on the parylene covered wafer, and then degassed in a vacuum chamber. After degassing, the wafer was spin coated with the silicone. Curing of the spin coated wafer occurred at 150 °C for 1 hour. Samples were cut into 5.5-mm-wide samples and were approximately 250 μm thick (from 240 to 280 μm thick) after spin coating. Thickness was measured with a caliper and accounted for during modulus testing. Five samples were taken from each of five wafers that were prepared. Samples were stretched at 1 % strain per minute to 10 % total strain at room temperature.

Repeatability is shown in Table 2-3. The maximum average modulus was found to be 1.35 MPa and the minimum modulus was 1.25 MPa. The average modulus from the 5 wafers was 1.31 MPa. Maximum error from the mean was 5 %, corresponding to wafer 5. Maximum error from the mean for all samples was 8.3 % corresponding to wafer 5, sample 5. Higher error from individual samples may be from measurement error in thickness across the wafer.

Table 2-3. Modulus of elasticity measured from 5 wafers

	Modulus (MPa) cured @ 150 °C 1 hr						
	Sample 1	Sample 2	Sample 3	Sample 4	Sample 5	Avg.	Stdev
Wafer 1	1.3132	1.3009	1.2809	1.3159	1.3141	1.305	0.013
Wafer 2	1.3246	1.2964	1.3393	1.3150	1.2847	1.312	0.020
Wafer 3	1.3308	1.3277	1.3681	1.4142	1.3258	1.353	0.034
Wafer 4	1.3762	1.3480	1.3452	1.3670	1.3148	1.350	0.021
Wafer 5	1.2147	1.2490	1.2824	1.2751	1.2038	1.245	0.031

2.14 Ratio of Part A to Part B

In order to determine the effect of cross linker on the mechanical properties of the silicone, experiments were completed to determine the change in modulus of elasticity relative to different crosslinking ratios. Part A to Part B ratios used were 10:30, 10:20, 10:10, 10:2.75, 10:2.5, 10:2, 10:1.5, 10:1.25, 10:1, 10:0.75, 10:0.5, and 10:0.25. All wafers were cured at 150 degrees C for 1 hour. Figure 2-6 and Table 2-4 show the results of the testing. At low A/B ratios, there is an excess of part B. This leads to a lower crosslink density per volume and therefore a lower modulus of elasticity. The samples were not noted to be tacky with excess part B. The curve reaches a maximum value of modulus when the part A and part B are stoichiometrically matched. When this occurs, there are an equal number of vinyl and hydride groups to crosslink and crosslinking per volume is a maximum. Stoichiometrically matching occurred at a A/B ratio of 8, with a corresponding modulus of 1.41 MPa. Above this, additional part A only decreases the crosslink density of the silicone elastomer [72]. With excess part A, the samples were noted to feel tacky. It was not possible to peel the wafers mixed at 10:0.25 even after additional curing at 150 degrees C.

Although the recommended mix ratio is 10:1, the stoichiometrically matched ratio corresponds to 8:1. Although this seems that 10:1 would be stoichiometrically matched, similar results were found for another 10:1 silicone which had a maximum modulus at 7.5:1 [72].

Based on these results, the 10:1 mixing ratio is close to stoichiometrically matched. However, it produces a modulus of 1.27 MPa, which is 10% lower than the

maximum modulus at 1.41 MPa. These results indicate that mixing ratios closer to 8:1 should be considered in final device design.

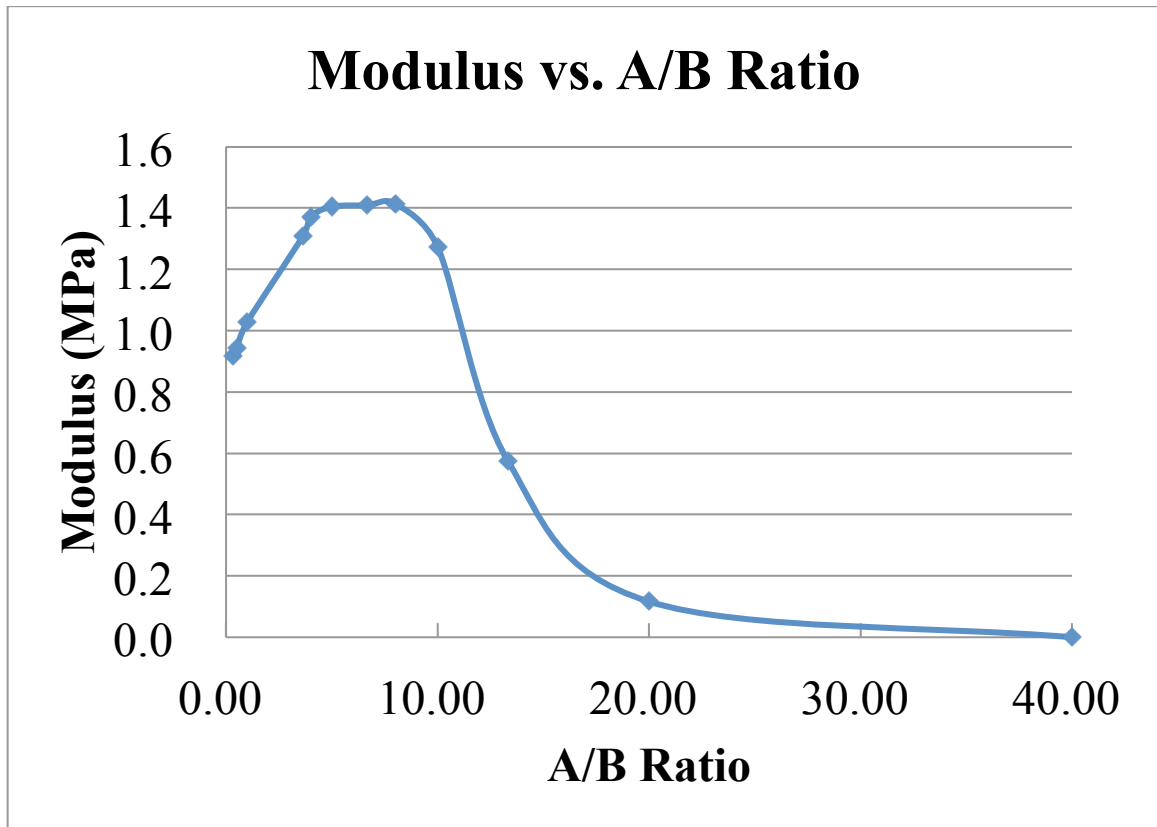


Figure 2-6. Modulus of elasticity versus A/B ratio of MED4-4210

Table 2-4. Modulus of elasticity versus mix ratio

Mix Ratio	Modulus (MPa)	
	Average	Stdev
10:30	0.92	0.03
10:20	0.94	0.04
10:10	1.03	0.04
10:2.75	1.31	0.05
10:2.5	1.37	0.04
10:2	1.40	0.02
10:1.5	1.41	0.01
10:1.25	1.41	0.03
10:1	1.27	0.03
10:0.75	0.57	0.02
10:0.5	0.12	0.00
10:0.25	0.00	0.00

2.15 Creep-Recovery Testing

Creep testing is used to demonstrate how the silicone elastomer strain relates to a constant stress over a period of time. This is tested by taking a known length of sample, applying a constant stress, and monitoring strain of the sample. A creep-recovery test follows the creep test with removal of the stress, and the strain is monitored again.

An ideal creep test uses an instantaneous stress applied to the sample, while strain is monitored. The stress is maintained until the material reaches equilibrium.

Viscoelastic materials are often represented in a four-element model to demonstrate their response to loading. In the four-element model, there is a spring and dashpot in parallel. This is in series with a spring and dashpot. The response of the dashpot allows for a viscous flow when a constant stress is applied to the material. This corresponds to a continuous expansion of the material when a constant stress is applied. The spring acts in a Hook's fashion, providing a linear instantaneous strain for a stress.

The four-element model is shown in Figure 2-7 and a typical stress versus time and strain versus time is shown in Figure 2-8.

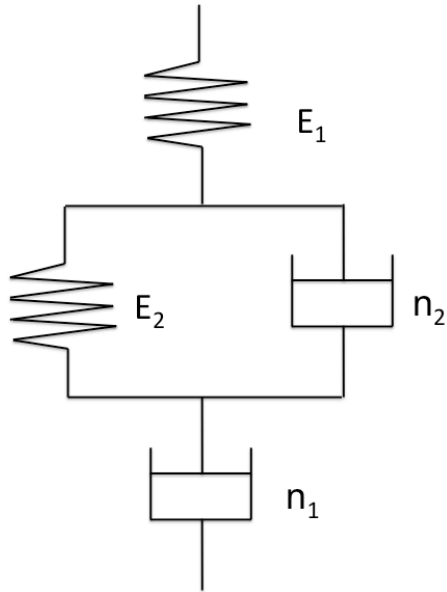


Figure 2-7. Four-element model

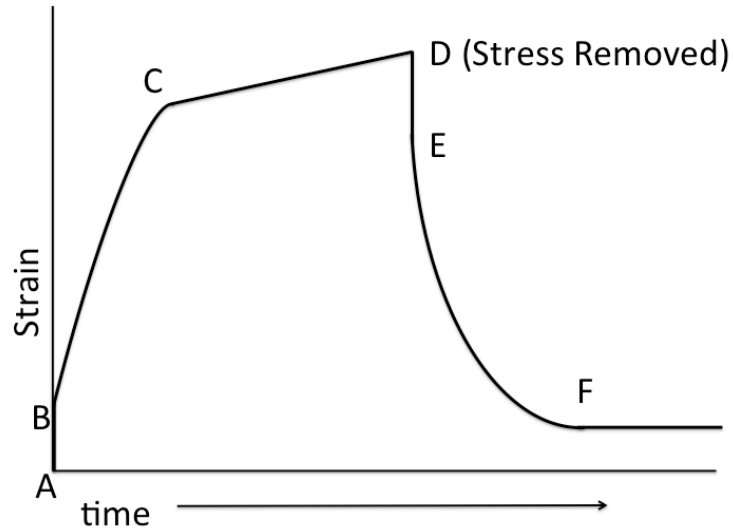


Figure 2-8. Typical creep-relaxation curve

Referring to Figure 2-8, stress is applied to the sample at point A (at time zero). Initially, there is an instantaneous strain on the sample (from A to B), which corresponds to the Maxwell element E_1 shown in Figure 2-7. Then the curved increase in strain from B to C is seen, which corresponds to E_2 and n_2 in parallel. From C to D, there is an increasing strain with the constant stress, corresponding to element n_1 . After the stress is removed at point D, relaxation occurs. As in the creep model, element E_1 is responsible for the immediate strain relaxation from D to E. Elements E_2 and n_2 are related to the recovery curvature from points E to F.

There are multiple methods to analyze a creep-relaxation curve as shown in Figure 2-8. The first method is to fit data to the four-element model. Another method is to analyze irrecoverable creep, viscosity, modulus, and relaxation time. Graphically, this is shown in Figure 2-9. Irrecoverable strain is found by measuring the final equilibrium strain and comparing it with the initial strain. Modulus of elasticity can be computed by extrapolating the strain in the linear region back to the time=0 using that as the strain

amount for the stress applied (modulus of elasticity = stress/strain). The relaxation time constant can be found from the curve after stress is removed. Viscosity is inversely proportional to the slope in the linear region of the curve (slope = stress applied / viscosity).

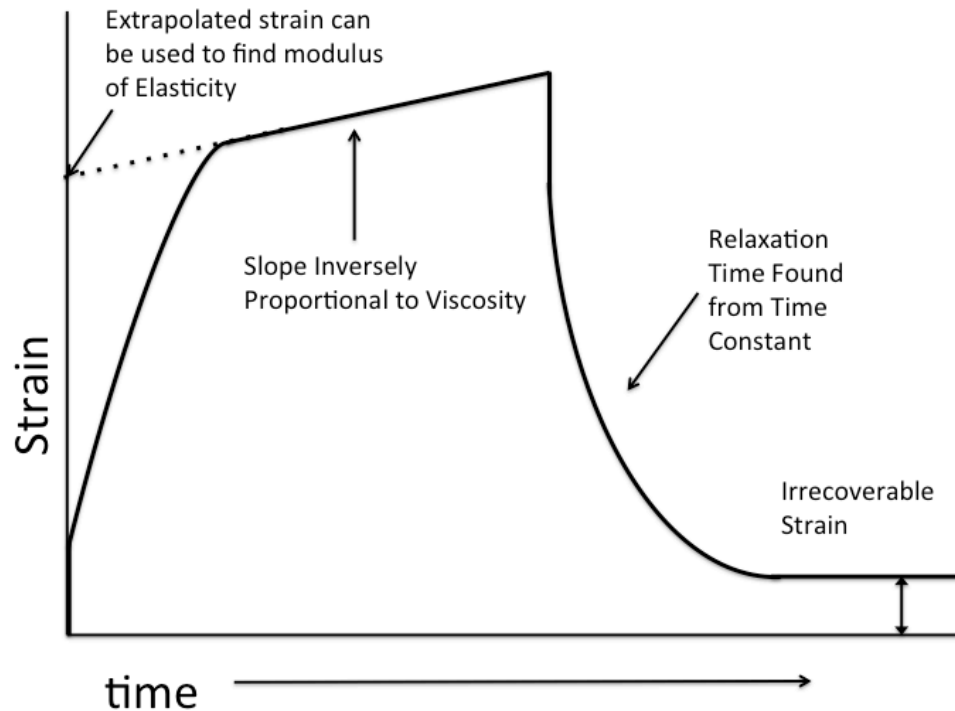


Figure 2-9. Diagram demonstrating how to calculate modulus of elasticity, viscosity, relaxation time, and irrecoverable strain

To simulate the cyclic loading conditions of the lens, stress relaxation was applied to samples of MED4-4210 four times before irrecoverable strain was measured. Cycling occurred in four 20-minute intervals of 0.05 MPa stress (10 min) followed by 0 MPa stress (10 min). All testing occurred in air at 37 °C. A typical experiment is shown in Figure 2-10.

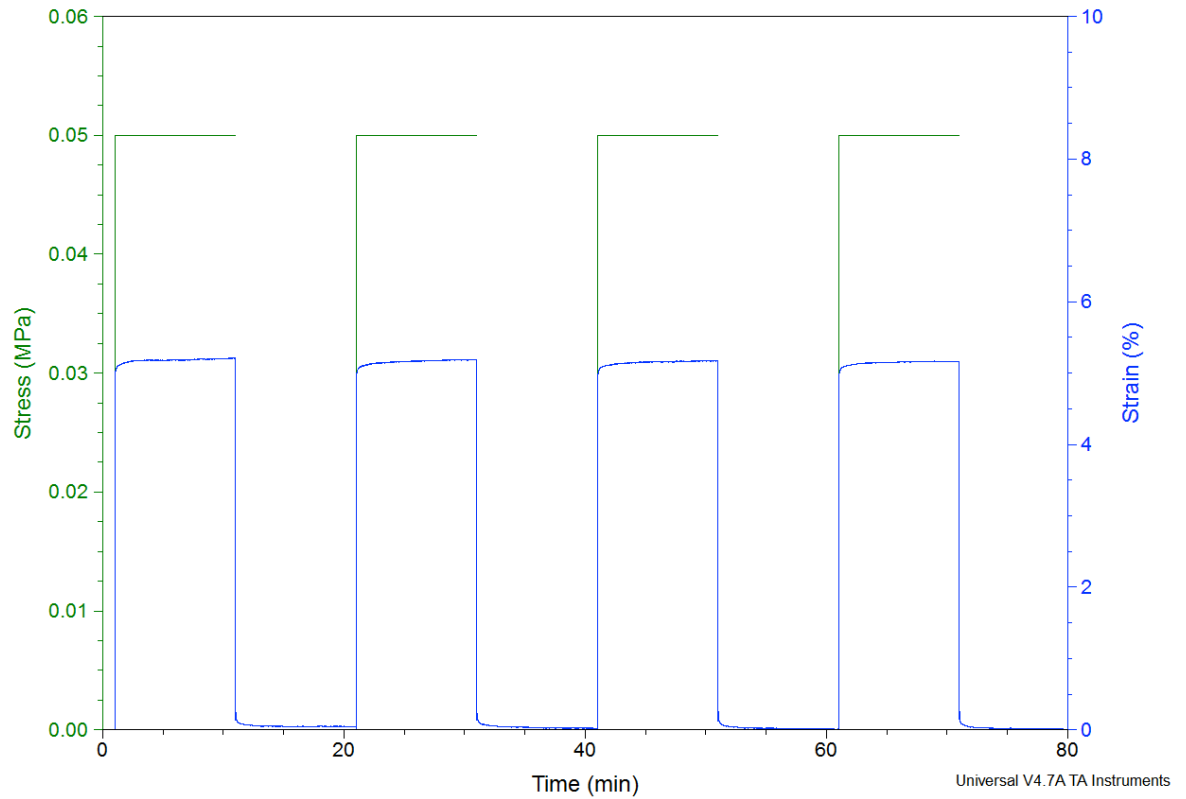


Figure 2-10. Creep experiment: Stress and strain versus time for an example experiment

Viscoelastic properties were measured with silicone samples cured under different conditions (80, 100, and 150 °C) at different curing times (15, 30, 60, 90, 120 min). Experiments were completed at body temperature (37 °C) to mimic implant conditions (Table 2-5). After little to no creep was seen at 37 °C experiments were conducted at 100 °C to examine creep at elevated temperatures (Table 2-6). Because creep testing was shown to deviate from the four-element model, viscoelastic properties were calculated using viscosity, relaxation time, modulus of elasticity, and strain recovery as illustrated in Figure 2-9.

As shown in Table 2-5, for all samples at 37 °C strain at recovery was negligible relative to the DMA repeatability, with a maximum of 0.05% strain (2.8 μm) and an

average value of 0.01% strain (0.6 μm). In addition, the large values determined for viscosity correspond with negligible displacements at .05 MPa. The average viscosity was 1.3×10^{11} Pa sec, which corresponds to an average length change of 1.4 μm for the 8 minutes in the linear region of the creep experiment.

At 100 °C the silicone demonstrated elastic behavior and very little viscoelastic behavior as well. This is shown in Table 2-6. After four creep / relaxation cycles, the strain at recovery was an average of 0.012% (0.7 μm) and a maximum of 0.05% (2.8 μm). The slope during the creep test was almost zero and corresponding viscosities were an average of 1.06×10^{12} Pa sec, which corresponds to an average length change of 0.8 μm for the 8 minutes in the linear region of the creep experiment.

Because all values of strain % at recovery were very small and almost zero, no trends were seen based on the various curing schedules. Likewise, the slope of the strain vs. time curve was very small during the period of applied stress as almost no displacement changed while the sample was held in tension. Therefore, no trends were seen relative to the curing data and viscosity as the material behaved almost entirely elastically.

Table 2-5. Viscoelastic properties at body temperature (37 °C) under different curing schedules

Cure Condition	Slope (sec⁻¹ x 10⁻⁷)	Viscosity (Pa*sec x 10¹¹)	Strain (%) at Recovery	Displacement at Recovery (μm)	Displacement during last 8 minutes of creep (μm)	Retardation Time (sec)
80 °C for 15 min	7.3	0.7	0.010	0.5	2.2	< 0.1
80 °C for 30 min	3.7	1.3	0.005	0.3	1.7	< 0.1
80 °C for 60 min	4.0	1.2	-0.003	-0.1	2.0	< 0.1
80 °C for 90 min	3.8	1.3	0.010	0.5	1.5	< 0.1
80 °C for 120 min	3.4	1.5	0.007	0.4	1.5	< 0.1
80 °C for 15 min	3.7	1.4	0.014	0.8	1.9	< 0.1
80 °C for 30 min	5.7	0.9	0.012	0.6	1.9	< 0.1
80 °C for 60 min	5.3	0.9	0.014	0.7	1.8	< 0.1
80 °C for 90 min	3.8	1.3	0.005	0.3	1.1	< 0.1
100 °C for 15 min	3.3	1.5	0.018	1.0	1.0	< 0.1
100 °C for 30 min	3.6	1.4	0.009	0.5	1.4	< 0.1
100 °C for 60 min	4.3	1.2	0.006	0.3	1.3	< 0.1
100 °C for 90 min	4.1	1.2	0.010	0.6	1.4	< 0.1
100 °C for 120 min	3.3	1.5	0.002	0.1	1.3	< 0.1
150 °C for 15 min	3.7	1.3	0.013	0.7	1.2	< 0.1
150 °C for 30 min	4.1	1.2	0.006	0.3	1.1	< 0.1
150 °C for 60 min	2.7	1.8	0.003	0.2	0.9	< 0.1
150 °C for 90 min	3.3	1.5	0.009	0.5	1.1	< 0.1
150 °C for 120 min	3.5	1.4	0.052	2.8	1.0	< 0.1

Table 2-6. Viscoelastic properties at elevated temperature (100 °C) under different curing schedules

Cure Condition	Slope (sec⁻¹ x 10⁻⁷)	Viscosity (Pa*sec x 10¹¹)	Strain (%) at Recovery	Displacement at Recovery (μm)	Displacement during last 8 minutes of creep (μm)	Retardation Time (sec)
80 °C for 30 min	4.8	1.1	0.002	0.1	0.6	< 0.1
80 °C for 60 min	4.0	1.2	0.015	0.8	0.4	< 0.1
80 °C for 90 min	2.3	2.2	0.003	0.2	0.6	< 0.1
80 °C for 120 min	1.3	3.9	-0.003	-0.2	0.5	< 0.1
80 °C for 15 min	4.7	1.1	0.043	2.2	1.3	< 0.1
80 °C for 30 min	1.3	3.9	0.054	2.8	1.1	< 0.1
80 °C for 60 min	2.4	2.1	0.034	1.7	0.8	< 0.1
80 °C for 90 min	1.9	2.7	0.035	1.7	0.9	< 0.1
80 °C for 120 min	2.2	2.3	0.020	1.0	0.6	< 0.1
100 °C for 15 min	0.9	5.8	0.009	0.5	0.9	< 0.1
100 °C for 30 min	0.0	100.7	0.006	0.3	0.6	< 0.1
100 °C for 60 min	3.2	1.5	0.004	0.2	0.6	< 0.1
100 °C for 90 min	1.3	3.8	0.005	0.3	0.7	< 0.1
100 °C for 120 min	2.8	1.8	-0.004	-0.2	1.0	< 0.1
150 °C for 15 min	0.8	6.0	0.031	1.6	1.3	< 0.1
150 °C for 30 min	1.3	3.9	0.009	0.5	0.8	< 0.1
150 °C for 60 min	1.1	4.6	0.007	0.3	0.7	< 0.1
150 °C for 90 min	1.5	3.3	0.004	0.2	0.8	< 0.1
150 °C for 120 min	0.1	50.5	-0.031	-1.5	0.6	< 0.1

This data demonstrates that all cure schedules tested produce a silicone with low viscoelastic properties. In fact, due to the extremely small displacements measured, the behavior may be from a slight slipping of the sample against the clamp, thermal expansion of the DMA / sample, or measurement variation in the DMA linear encoder. Therefore, very little to no viscoelasticity was seen during this experiment. In addition, these tests indicate that the material is acceptable for an environment with cyclical stress, such as in the condition of an intraocular lens.

2.16 Stress Relaxation

Stress relaxation experiments involve quickly applying a strain to a material and observing the change in stress with time. Stress relaxation experiments were carried out with 10 % strain held for 10 minutes. Samples with different curing schedules were used to screen for variation in silicone properties based upon curing. All tests were performed at 37 °C to mimic the natural environment of the body.

For all samples, stress remained fairly constant and displayed elastic behavior. Therefore, the four-element model was a poor fit for the data and was not used. Initially, there was a very small relaxation within the first two minutes. However, from the last 8 minutes, stress changed an average of less than 1% (corresponding to 1.6 mN force difference). Because so little viscoelasticity was seen, the four-element model did not fit the data well. Data from the experiments is shown in Table 2-7.

Table 2-7. Stress values at 0, 2, and 10 min for different curing conditions

Cure Condition	Stress (MPa) at 0 min	Stress (MPa) at 2 min	Stress (MPa) at 10 min
80 °C for 15 min	0.088	0.083	0.083
80 °C for 30 min	0.108	0.107	0.107
80 °C for 60 min	0.122	0.121	0.121
80 °C for 90 min	0.128	0.128	0.127
80 °C for 120 min	0.122	0.117	0.117
80 °C for 15 min	0.084	0.081	0.080
80 °C for 30 min	0.083	0.078	0.076
80 °C for 60 min	0.109	0.104	0.102
80 °C for 90 min	0.116	0.112	0.110
80 °C for 120 min	0.115	0.109	0.107
100 °C for 15 min	0.136	0.132	0.131
100 °C for 30 min	0.137	0.133	0.132
100 °C for 60 min	0.123	0.119	0.118
100 °C for 90 min	0.040	0.039	0.038
100 °C for 120 min	0.102	0.099	0.099
150 °C for 15 min	0.123	0.121	0.121
150 °C for 30 min	0.140	0.136	0.135
150 °C for 60 min	0.151	0.146	0.146
150 °C for 90 min	0.150	0.146	0.145
150 °C for 120 min	0.156	0.152	0.151

Stress relaxation experiments demonstrate that under the various cure schedules the silicone demonstrates very little to no viscoelasticity. This is similar to creep experiments. This indicates that silicone should behave in essentially an elastic manner for the implant.

2.17 Permeability of Silicone

The permeability of silicone was tested using an uptake method. A description of this method is found in Wolf [73].

Samples of silicone were spin coated on a parylene-coated wafer. The thickness of the silicone sheets was measured with a caliper and samples were weighed for base weight. All weight measurements were taken with a Mettler Toledo balance AB204-S, which is accurate to 0.2 mg. Next, the samples were immersed in a vial containing silicone oil. The samples were removed from the silicone oil bath, blotted dry, and then weighed. After weighing, the samples were returned to the silicone oil for further testing and measurement. Weight measurements were taken every five minutes for the first 30 minutes of testing to provide an accurate measurement of slope. After this, measurement intervals were decreased. Weight measurement continued until sorption leveled off, and a measurement of final sorption was taken.

To use sorption curves to calculate diffusion constants, Fick's laws of diffusion were used. Fick's first law states that flux, F is proportional to the diffusion concentration gradient, ∇C , multiplied by the diffusion constant, D :

$$F = -D(\nabla C)$$

From Fick's second law where D is independent of time, and concentration varies with time:

$$\frac{\partial C}{\partial t} = \nabla F = -D(\nabla^2 C)$$

If the sample is considered to have diffusion only in one direction and the side effects are neglected (i.e. for a thin film), then Fick's laws can be rewritten as:

$$F_x = -D \frac{\partial C}{\partial x}$$

$$\frac{\partial C}{\partial t} = \frac{\partial F_x}{\partial x} = -D \left(\frac{\partial^2 C}{\partial x^2} \right)$$

Fick's second law can be solved for fractional mass uptake [74-76].

$$\frac{M(t)}{M_{\infty}} = 1 - \frac{8}{\pi^2} \sum_{n=0}^{\infty} \frac{1}{(2n+1)^2} \exp\left(-\frac{(2n+1)^2 \pi^2 D t}{l^2}\right)$$

For short times this is linear and simplifies to

$$\frac{M(t)}{M_{\infty}} = \frac{4}{l} \left(\frac{D t}{\pi} \right)^{\frac{1}{2}}$$

Solving for diffusion constant yields:

$$D = \frac{\pi l^2}{16} (S / M_{\infty})^2$$

where S is the slope in the initial linear portion of the uptake curve, and M_{∞} is the final solubility. This solution allows the diffusion constant of a liquid in a thin sheet to be found from the uptake curve.

Four samples were tested in 100 cst silicone oil (Dow Corning 360 medical fluid). One sample of MED4-4210 was tested in 1000 cst silicone oil (Nusil, MED 360). Figure 2-11 shows graphs of uptake while Table 2-8 shows the calculated diffusion constants.

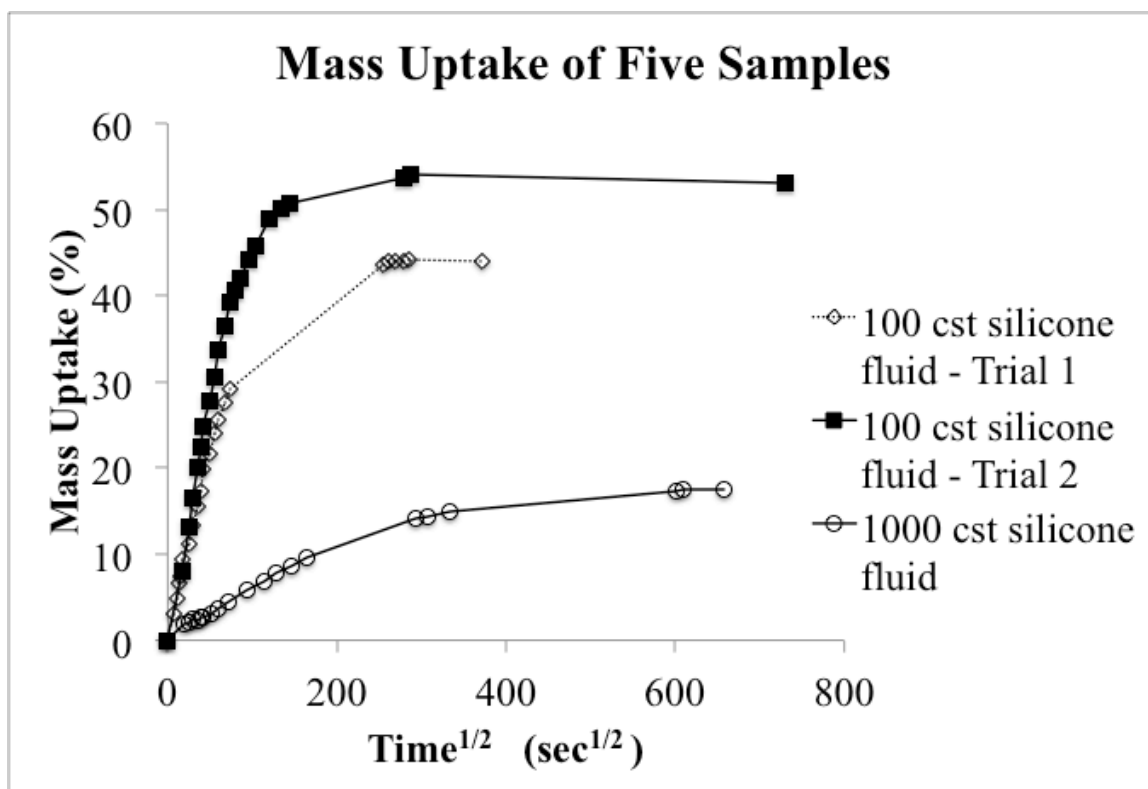


Figure 2-11. Uptake experiment from three samples

Table 2-8. Diffusion constants for three samples

Sample	Thickness (mm)	S(%/sec ^{1/2})	M_{∞} (%)	D (10 ¹² m ² s ⁻¹)
MED4-4210 in 100 cst Silicone Oil (Trial 1)	0.4318	0.43	44.0	3.5
MED4-4210 in 100 cst Silicone Oil (Trial 1)	0.4318	0.58	53.1	4.3
MED4-4210 in 1000 cst Silicone Oil	0.4826	.055	17.6	0.44

These results demonstrate that using a higher centistoke oil reduces diffusion into the samples. For example, the diffusion constant for a MED4-4210 with 1000 cst oil is 8.9 times less than with the 100 cst silicone oil. This data indicates that using a higher viscosity silicone oil inside a silicone shell will significantly reduce diffusion of the oil through the wall of the shell.

2.18 Lens Accelerated Aging Tests

Based upon uptake experiments, lenses were built and soak tested for leakage in an accelerated environment. Lenses underwent accelerated aging testing to monitor weight and optical clarity at 85 °C. Each lens was placed into separate containers partially filled with saline solution. Then, these containers were placed into an 85 °C preheated oven. After each week (288±4 hours) and at the end of this test period, each lens was removed from the oven, rinsed with sterile water, and placed in a fume hood to dry for four hours. After the lenses dried, they were weighed on a ±0.0002 g accuracy scale to detect weight differences in the lens and monitored for optical clarity.

All lenses tested remained visually clear throughout the test period. In addition, lens weight changes were different for the 100 cst and 1000 cst oil. Data is shown in Figure 2-12 and Figure 2-13.

	Measurement	100 cst Lens 1	100 cst Lens 2	1000 cst Lens 1	1000 cst Lens 2
0 Time Weight (g)	Average	0.1766	0.1741	0.1040	0.1058
1 Week Weight (g)	Average	0.1747	0.1731	0.1040	0.1057
2 Week Weight (g)	Average	0.1738	0.1719	0.1040	0.1055
3 Week Weight (g)	Average	0.1732	0.1710	0.1040	0.1055
4 Week Weight (g)	Average	0.1703	0.1703	0.1040	0.1055
5 Week Weight (g)	Average	0.1701	0.1701	0.1040	0.1055
6 Week Weight (g)	Average	0.1690	0.1697	0.1040	0.1055
7 Week Weight (g)	Average	0.1681	0.1693	0.1040	0.1055
8 Week Weight (g)	Average	0.1673	0.1687	0.1040	0.1055

Figure 2-12. Lens weight versus time for lenses filled with 100 cst silicone oil and 1000 cst silicone oil

Lens	Weight Loss (g)	% Weight Loss
100 cst Lens 1	0.0093	5.25
100 cst Lens 2	0.0054	3.08
1000 cst Lens 1	0.0000	0.00
1000 cst Lens 2	0.0003	0.28

Figure 2-13. Summary of weight loss for lenses after 8 weeks of accelerated testing

While lenses filled with 100 cst oil have weight losses between 3.1-5.3% of total weight, the lenses filled with 1000 cst oil have between 0 and 0.28% weight loss. Furthermore, for the weight loss of 0.28%, it can be seen that this occurs within the first two weeks of testing and then the lens remains stable. Therefore, it is possible that this was remnant oil from the filling process, which diffused into the surrounding saline.

This data demonstrates the possibility of minimal leak when using a 1000 cst oil with a MED4-4210 silicone elastomer.

2.19 Summary

Based on its FDA documented biocompatibility, optical clarity, elongation characteristics, Young's modulus, and base viscosity, MED4-4210 was screened as a possible material for a biomimetic accommodating intraocular lens.

Extensive mechanical testing was completed on MED4-4210 to demonstrate its viability for use as a biomedical implant. The glass transition temperature was found to be far below any temperature seen in the body / eye, making it operable in the rubbery region of performance. An optimal curing schedule was determined based on Young's modulus measurements of the material at different curing temperatures and times.

A series of five wafers were mixed and cured to demonstrate repeatable processing of the silicone. From wafer to wafer, the maximum deviation of the average Young's modulus was determined to be 5%, indicating that current processing techniques are adequate to build lenses repeatably.

The mix ratios of part A and B were studied to demonstrate the effect of changing mix ratio on material properties. A large decrease in Young's modulus along with a tacky surface was seen as the A/B ratio was increased. Less of a decrease in Young's modulus was seen as the A/B ratio was decreased. In addition, qualitatively, there was less tackiness felt on the surface.

Viscoelastic properties were measured at various cure schedules to demonstrate the ability of the material to withstand implantation conditions. Both creep and stress relaxation experiments demonstrated very low viscoelasticity of the material under various curing schedules. This indicates that the device can be expected to perform in an elastic and repeatable manner under cyclical loading.

Finally, the diffusional properties of the silicone were examined with both 100 and 1000 cst oils. The diffusion constant of 1000 cst oil in the silicone was found to be $0.44 \times 10^{12} \text{ m}^2\text{s}^{-1}$ which is almost 10 times smaller than the diffusion constant of the 100 cst oil (between 3.4 and $4.3 \times 10^{12} \text{ m}^2\text{s}^{-1}$). Based on this experiment, the lenses were soak tested at elevated temperature, filed with 100 and 1000 cst silicone oil. The 100 cst oil was shown to permeate the wall of the lens after 8 weeks, while, little to no leakage was seen with the 1000 cst silicone oil. Therefore, initial testing demonstrates promise in using a 1000 cst oil with the MED4-4210 silicone elastomer.

3 MEASURING ACCOMMODATION IN A EX VIVO SETTING

3.1 Introduction

As discussed in previous chapters, the main goal of this work is to develop an accommodating intraocular lens to restore focusing ability after lens replacement surgery. However, in order to evaluate performance of an accommodating intraocular lens, an *ex vivo* test fixture is required. Although testing can be done in an *in vivo* setting, most animals either have differing accommodation mechanisms than humans, or have little accommodative power. For example, rats and rabbits have little to no accommodative power [77]. Canines have approximately 1 diopter of accommodative power, which is much less than humans, who can have 10 or more diopters [77]. Cats have accommodation levels of 4D. However the mechanism is different than in the human [77, 78]. Squirrels have accommodation values between 2 and 6D and the Indian Mongoose has accommodation levels close to humans, at 11-13.5 D [77]. Guinea pigs may have accommodation similar to the human with reduced amplitude and different eye

sizes [79]. Although birds have high accommodative amplitudes, the mechanism of accommodation is different than the human mechanism [77, 80]. Due to a paucity of animals with similar accommodative anatomy to the human, the primary model for testing is the Rhesus monkey. However, due to the cost and development time associated with testing on primates, it is desirable to prove the lens concept on an *ex vivo* model that mimics the natural anatomy as close as possible.

The testing apparatus is designed to objectively measure accommodation amplitude of the developed accommodating IOL. To be relevant to the human anatomy, the testing apparatus should mimic human tissue as much as possible. This includes mimicking the mechanical properties such as Young's modulus, as well as the geometry of the focusing mechanism. In addition, it needs to supply forces that are the same levels as the natural human lens.

To meet these needs, a testing apparatus is designed that tests the human focusing mechanism in a manner similar to the natural mechanism of accommodation based on work from Glasser [17] and similar to other prior work [81-83]. To do this, the human focusing mechanism of the eye is surgically removed and mounted in an external stretching device. The stretching device interacts with the ciliary muscles to actuate them in a manner similar to natural actuation. At the same time, the focal length of the lens is measured. By testing focal length and accommodation, it is possible to determine the change in focal length of the lens as accommodation occurs. In addition, by using human and porcine tissue, the geometry of the tissue is accurate. The loads are considered close to physiological based on the inability of dead tissue to transmit large loads. In addition, the procedure followed work from Glasser [17] demonstrating a similar method to

determine accommodative power of various age natural lenses, which was correlated to clinical data.

3.2 Surgical Implantation and Mounting of Lens

Lenses were initially implanted in cadaver human eyes for subsequent optical evaluation. Human eyes were obtained from several eye banks and were used within 3 days postmortem. The cornea and iris were removed to expose the lens (Figure 3-1 and Figure 3-2). A capsulorhexis consisting of a small circular incision was made slightly decentered in the lens capsule. The capsulorhexis was between 3.0 to 3.5 mm in diameter. The natural lens was removed through the capsulorhexis (Figure 3-3). This left the ciliary muscle, zonules, and most of the lens capsule intact for implantation and testing of the accommodating intraocular lens.

The evacuated lens was manually placed into the lens injector (Figure 3-4, Figure 3-5). The evacuated lens was inserted through the capsulorhexis into the capsular bag (Figure 3-6). The injection port was accessed again with the fluidic injector handpiece and silicone fluid was infused into the lens to fill it to the proper weight (Figure 3-7). Then, the fluidic injector handpiece was removed from the valve.

After implantation, the eye was dissected and mounted on a stretching / testing apparatus in a manner similar to Glasser [17]. The sclera of the eye was removed to expose the ciliary muscle (Figure 3-8). The anterior portion of the eye was cut away from the posterior portion of the eye to isolate the ciliary muscle, zonules, lens capsule, and IOL from the posterior portion of the eye (Figure 3-9). Any vitreous adhesions to the lens were cut (Figure 3-10). The focusing mechanism was mounted on a post and the anterior

ciliary muscle was glued with cyanoacrylate to a special stretching apparatus to mimic the natural accommodation of the eye while optical measurements were taken on the lens (Figure 3-12-Figure 3-13). The stretching apparatus was then put in a saline filled tank for optical measurements.

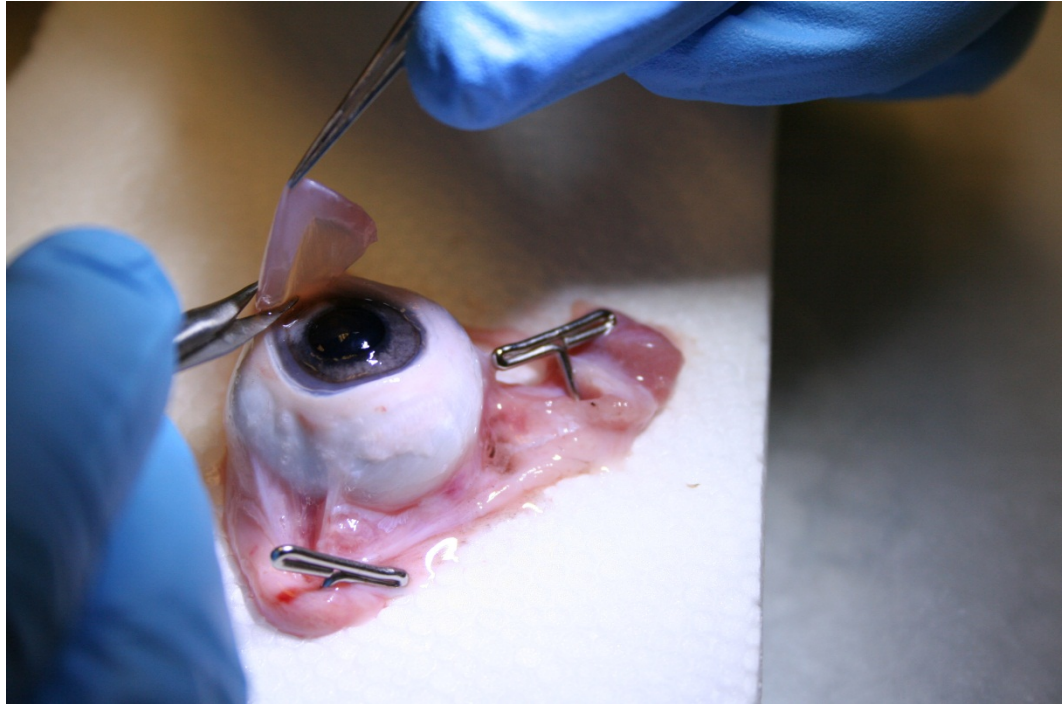


Figure 3-1. Keratectomy, continuous circular capsulorhexis and lens extraction is performed

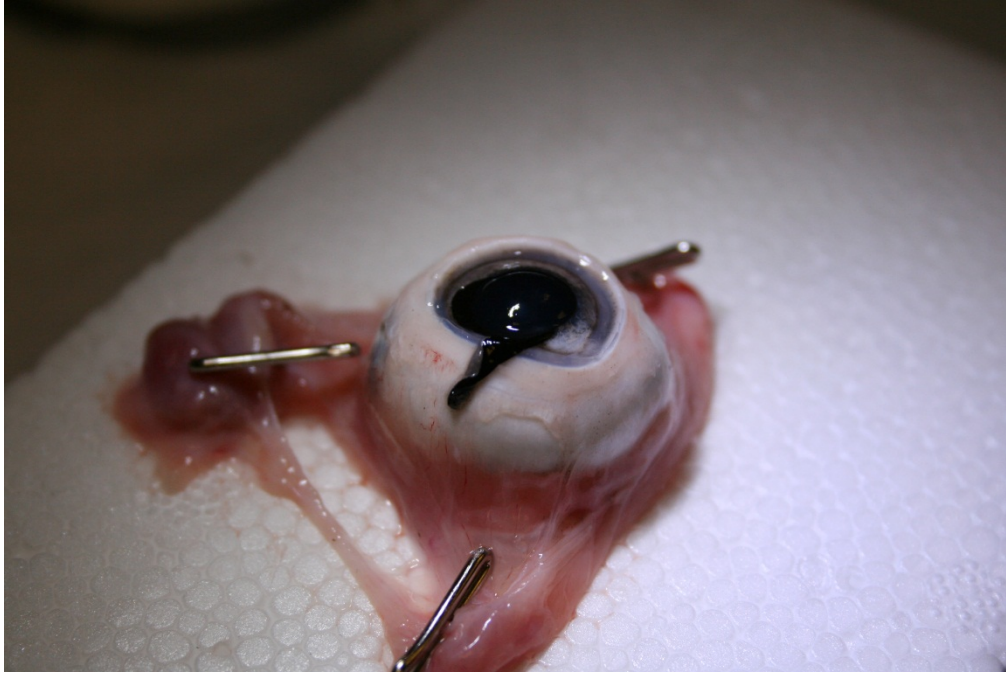


Figure 3-2. Removal of the iris



Figure 3-3. Removal of the lens. Here, this is shown as an extracapsular technique, however, with human eyes, phacoemulsification is used exclusively.

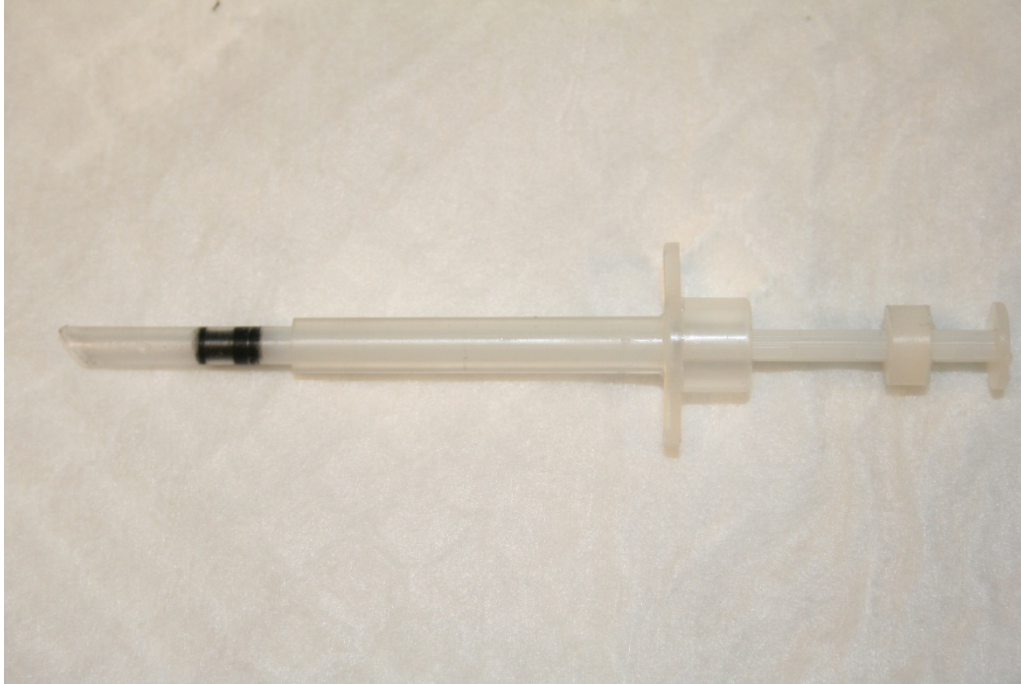


Figure 3-4. Lens injector, developed to place lens inside lens capsule

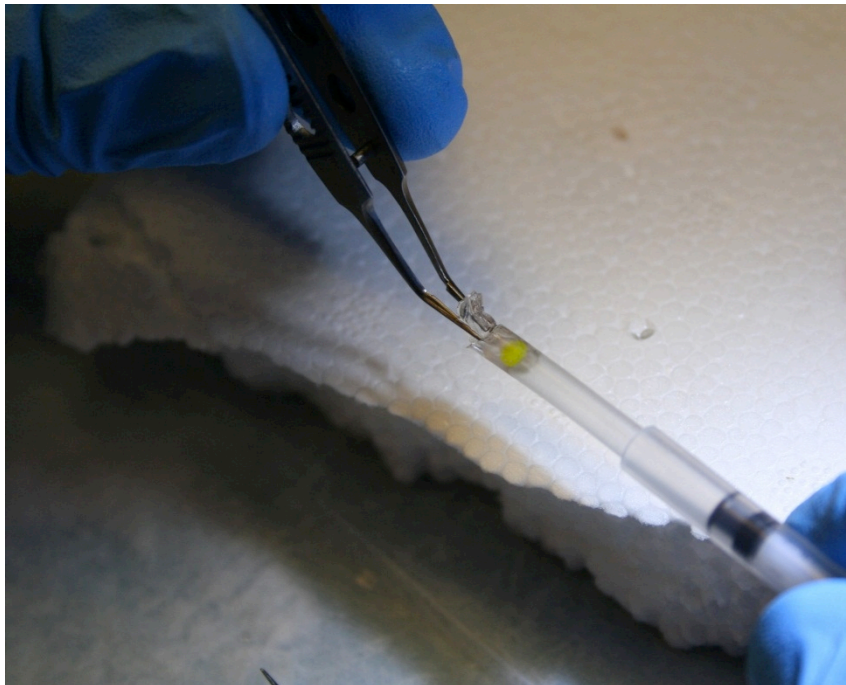


Figure 3-5. Manual insertion of the lens into the lens injector

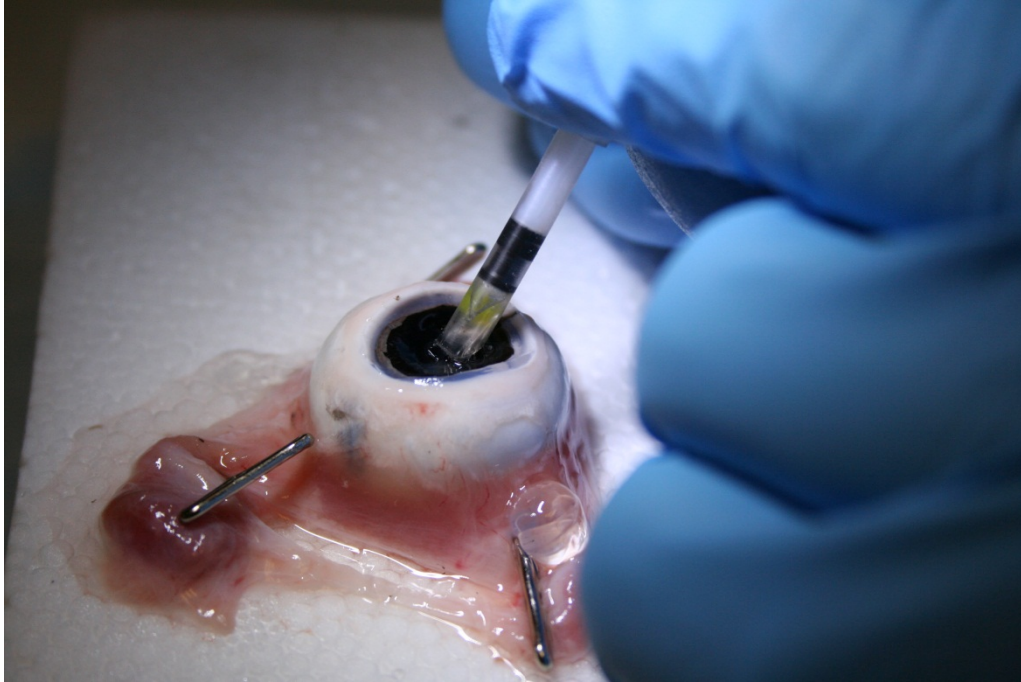


Figure 3-6. Injection of the lens into the lens capsule

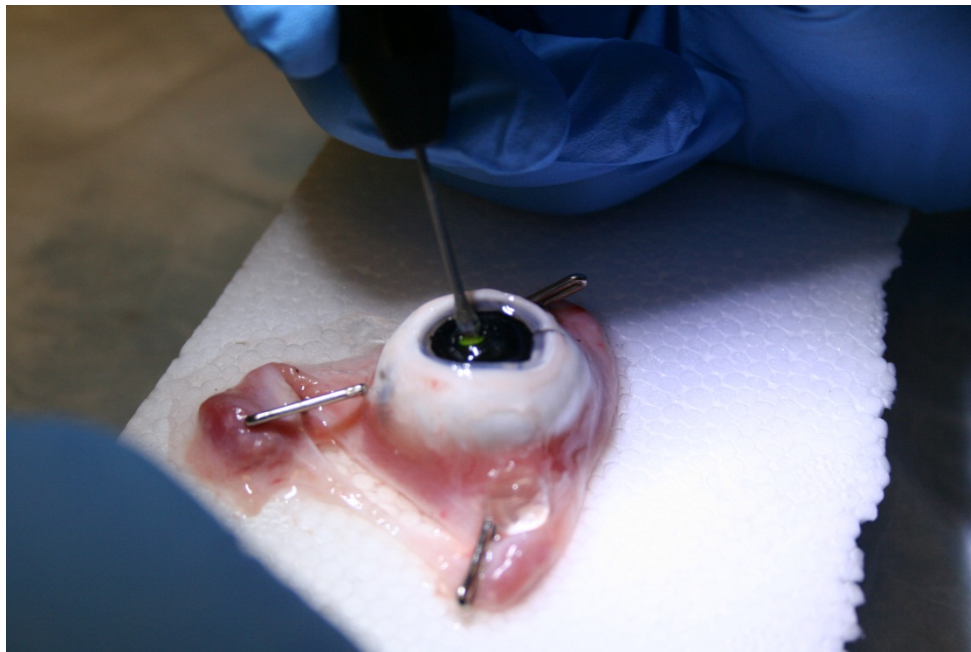


Figure 3-7. Injection of fluid into the implanted lens after accessing the lens refill valve

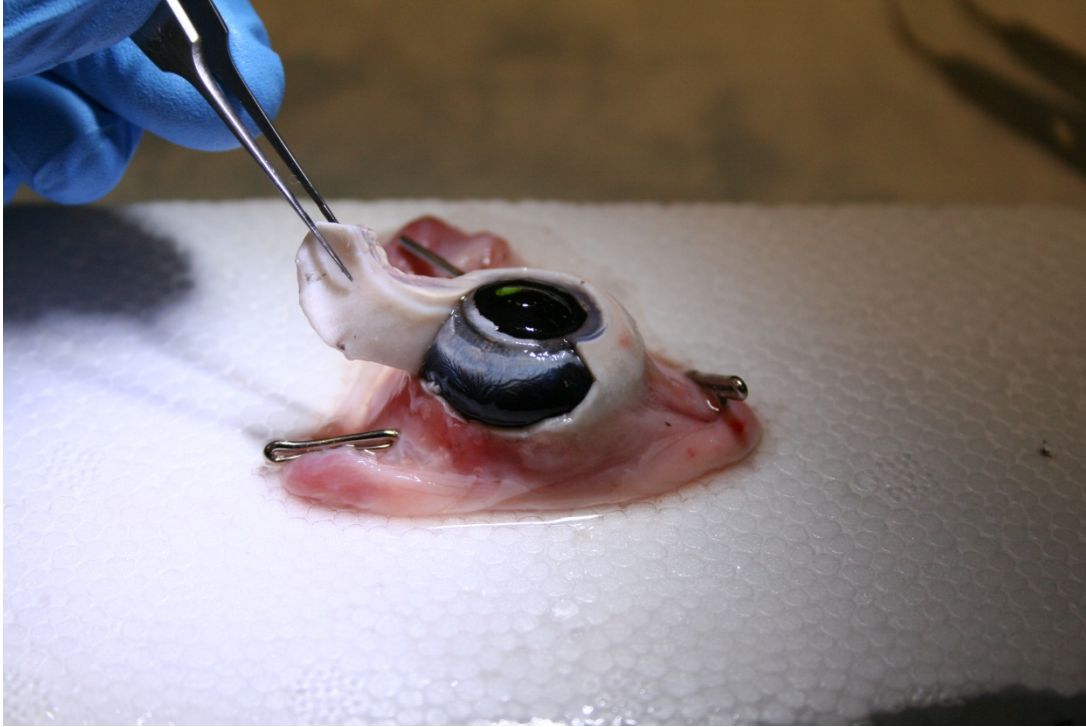


Figure 3-8. Sclerectomy

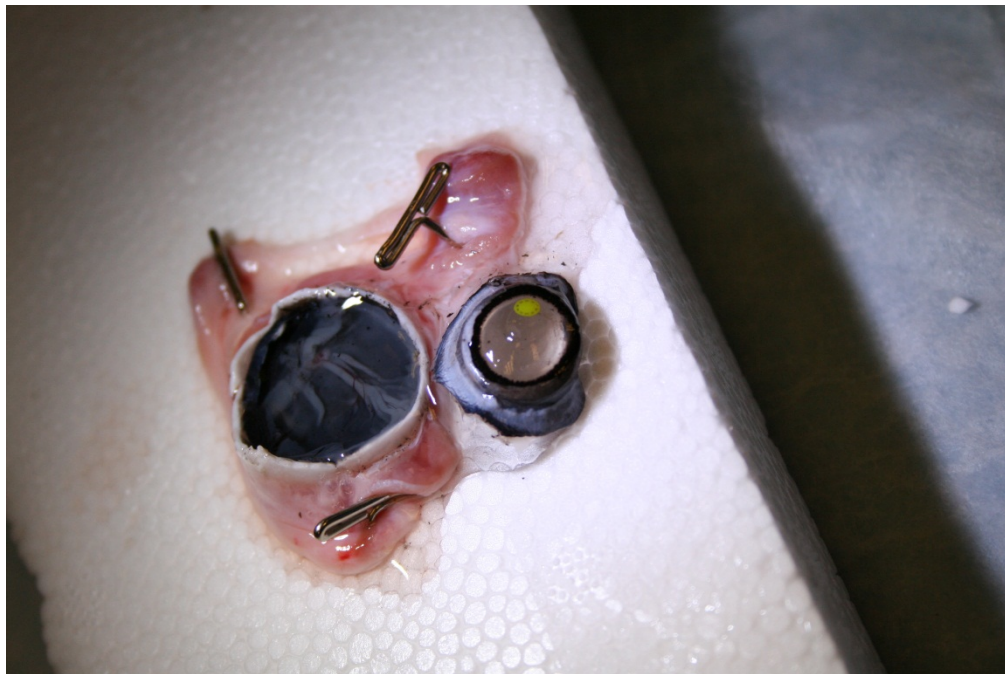


Figure 3-9. Removal of the focusing mechanism, including the ciliary muscle, zonules, lens capsule, and implanted lens

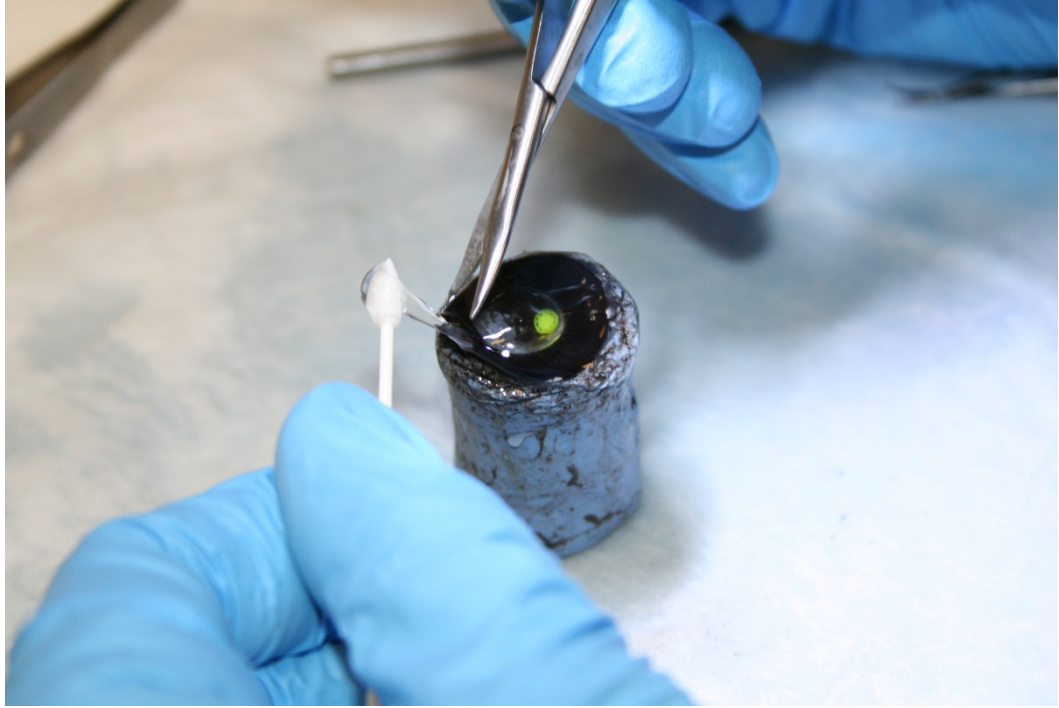


Figure 3-10. Removal of residual vitreous from the posterior pole of the lens capsule



Figure 3-11. Preparation for gluing the ciliary muscle to the stretching apparatus



Figure 3-12. Gluing the ciliary muscle to the stretching apparatus. Cyanoacrylate is applied to the jaws of the stretching apparatus before mounting.

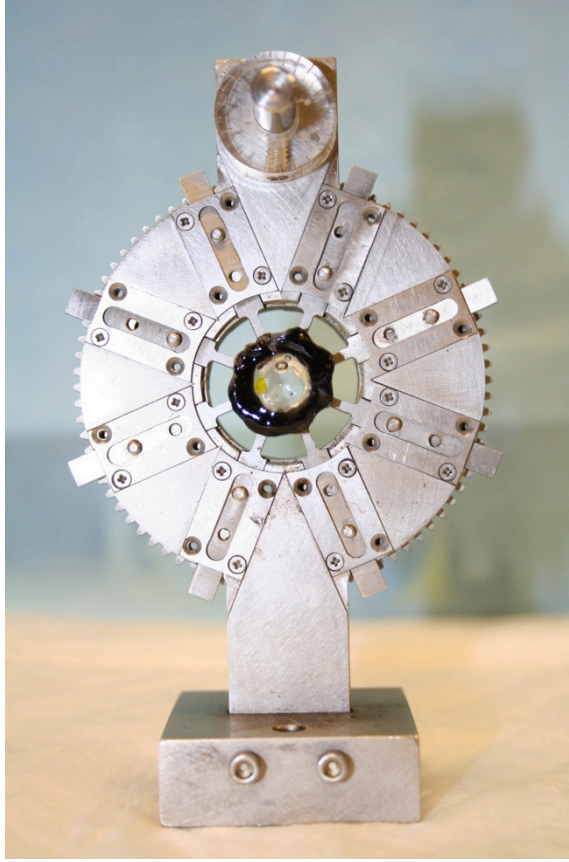


Figure 3-13. Lens mounted and prepared for optical testing

3.3 Stretching Apparatus

A stretching apparatus similar to the one used by Glasser was used to simulate accommodation in the cadaver eye [17]. Glasser characterized the amount of stretch on the ciliary muscle relative to presbyopic changes in the lens. With a stretch of 5 mm, his data demonstrated that accommodative amplitude decreased in an age-related manner similar to clinical data taken by Duane [15]. Therefore, a diameter stretch of 5 mm was used for testing in cadaver human eyes. In addition, a stretch of 3 mm was shown to not damage pig eyes, and for pig eyes 3 mm stretch was used.

The stretching apparatus consists of eight arms radially aligned. The arms are attached to a spur gear with helical paths machined into the face. These paths determine the eccentricity of the mounting arms. As the spur gear is rotated, the arms are moved further away or closer to the center (Figure 3-14). The motion of the arms mimics the pull of the zonules on the natural lens. Therefore, it was expected that as the jaws increase in diameter, the focal power of the natural lens would decrease in a manner similar to the natural human lens.

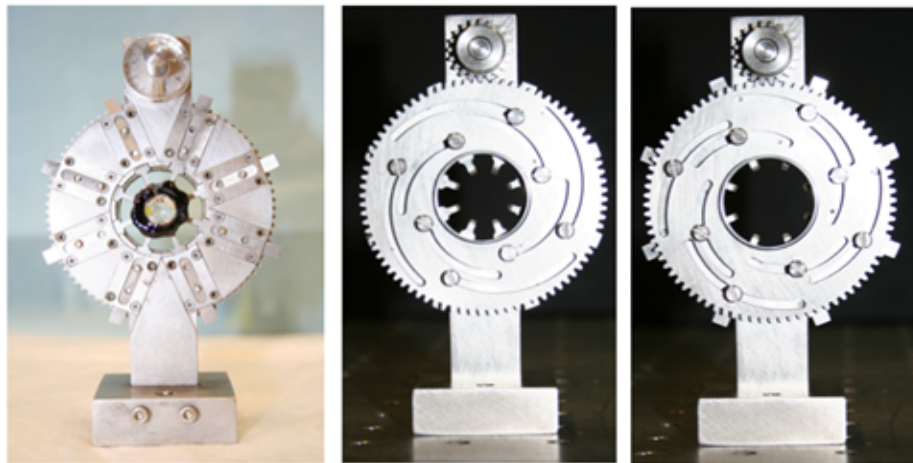


Figure 3-14. Stretching apparatus

Mechanically, the stretching apparatus is made of stainless steel to prevent corrosion while in the saline tank and allow autoclaving after use. A base plate is on the bottom and used to hold the stretching apparatus vertical as well as to position it relative to the water tank (with two dowel pins). Eight jaws 0.040 inch thick are mounted to the tissue with cyanoacrylate. They are bent to conform to the angle of the tissue during mounting and to protrude from the stretching apparatus. This gives visualization of the tissue from a side view. The jaws are retained in grooves cut in the stationary portion of

the stretching apparatus. The center of the stationary part has a one inch hole machined and is threaded at 100 threads per inch.

A series of 8 grooves are machined in the stationary portion of the stretching apparatus to allow the jaws to slide radially. A second spur gear is made with a wire electrical discharge machine (wire EDM). This allows tolerances of .002 inch or less to be machined, and reduces warping of the material during cutting. A 1.035-100 thread is put in the center of the spur gear and the stationary portion allowing them to be held together with a threaded insert. This allows the spur gear to rotate relative to the stationary plates.

The spur gear has eight helical grooves that allow shoulder screws to slide along them. The shoulder screws are bolted into the jaws. Therefore, a rotation of the spur gear causes the radial arms to slide in and out. A second smaller spur gear mates with the larger spur gear. This smaller gear is attached to a belt drive and stepper motor (256 k steps / rev). Therefore, rotation of the stepper motor causes the jaws to move in and out. The stepper motor actuates the tissue in a smooth and slow expansion to minimize tissue damage. The resulting stretch rate is 1 mm per minute.

3.4 Lens Insertion Tool

In order to insert the lens into the lens capsule, a special insertion tool was designed and fabricated. It was sized so that the lens could be placed within a 5 mm capsulotomy. The insertion tool (Figure 3-15) is manually actuated. It has an outer diameter of 3.8 mm to allow insertion through capsulotomies of 4 mm in diameter. The insertion tool outer diameter can be made smaller in line with existing other insertion

tools. A beveled end on the insertion tool allows the lens to be placed naturally in the capsule. This lens insertion tool demonstrates feasibility of delivering an accommodating intraocular lens.

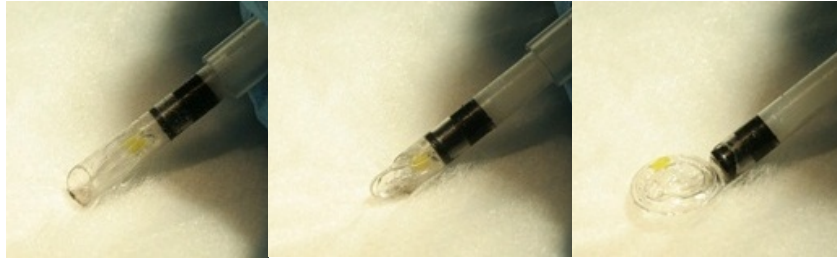


Figure 3-15. The lens inserter is shown with the lens loaded (left) and being delivered (middle and right)

3.5 Infusion / Aspiration System

The infusion / aspiration system was designed to allow inflation and deflation of the lens after it is inserted into the lens capsule. Schematically, the infusion / aspiration module consists of a venturi aspiration system, syringe infusion pump, and a fluidics handpiece used to deliver fluid to and from the lens. It is operated with two footswitches that allow switching between standby, infusion mode, and aspiration. Standby condition corresponds to no fluid flowing through the handpiece. Infusion corresponds to filling the lens with silicone oil and aspiration corresponds to evacuating the lens. A schematic of the inflation of the lens is shown in Figure 3-16.

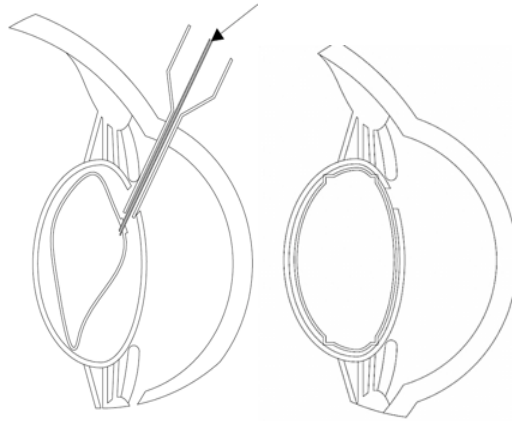


Figure 3-16. Filling of the accommodating IOL. The fluidic injector handpiece is used to access the injection port in the accommodating IOL. Infusion of silicone oil is used to fill the lens to the correct dioptric power (left). Finally, the fluidic injector handpiece is removed from the lens (right).

The fluidic injector handpiece is used to access the lens via the lens injection port after insertion (Figure 3-17). A 36-gauge blunt tip on the fluidic injector is used to enter through the injection port and then inflate the lens. The system is first primed so that silicone oil fills the lines. Next, the fluidics handpiece tip is inserted into the injection port in the lens and the lens is inflated. A syringe pump is used to dispense the correct level of silicone fluid to fill the lens.

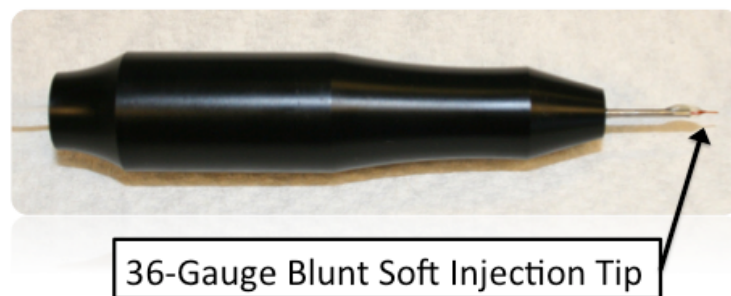


Figure 3-17. Fluidic injector handpiece

A schematic of the fluidics system is shown in Figure 3-18. The syringe pump and vacuum cassette are attached to the fluidics injector handpiece via a valve. Silicone oil is loaded in a syringe attached to the syringe pump. Upon actuation, the syringe pump dispenses a predefined amount of silicone oil. If aspiration is required, the syringe pump is turned off. Then, the valve is switched to allow fluidic connection between the vacuum cassette and the fluidics handpiece.

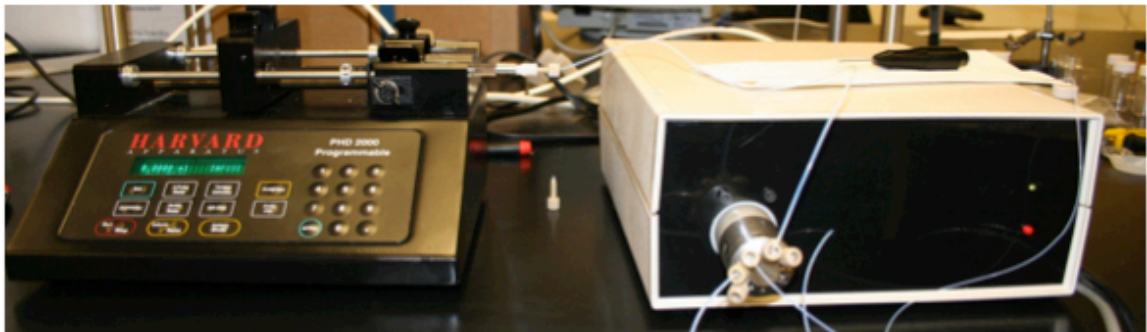
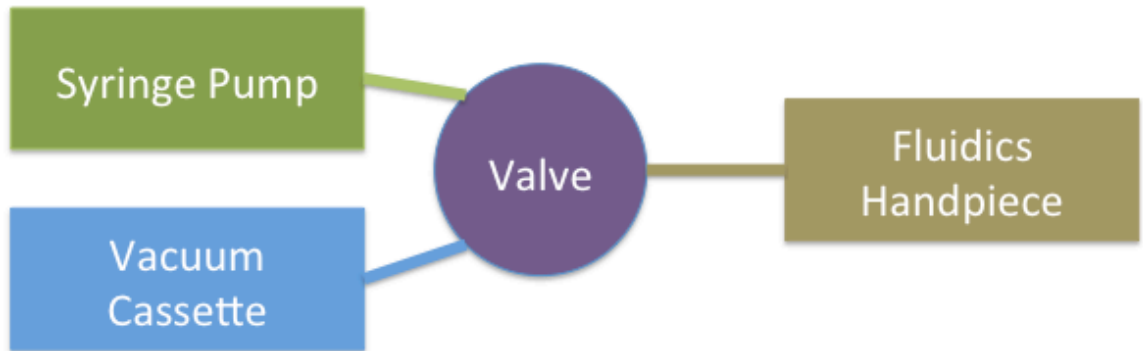


Figure 3-18. Diagram of the infusion / aspiration system (top). Photograph of the infusion / aspiration system (bottom). On the bottom left is the syringe pump. On the bottom right is the module with venturi cassette inside.

A diagram of the infusion / aspiration system is shown in Figure 3-19. 80 psi is brought into the console and is regulated to the venturi pump through a solenoid valve.

When the solenoid is open, the air is used to drive a venturi pump, providing vacuum for a surgical cassette. After leaving the venturi pump, the air passes through a silencer to lower noise from the high velocity air.

A syringe pump is used to infuse silicone oil into the lens. The vacuum cassette and the syringe pump attach to a syringe pump valve, which switches between the two lines and connects to the fluidic injector handpiece.

As shown in Figure 3-19, the switching happens with TTL logic. In addition, there is a NAND gate and hex inverter to prevent the syringe pump from actuating (or remaining on) when the valve is set to aspiration. This is so the syringe pump does not apply a high pressure to the valve when and potentially damage it when it is in the closed position.

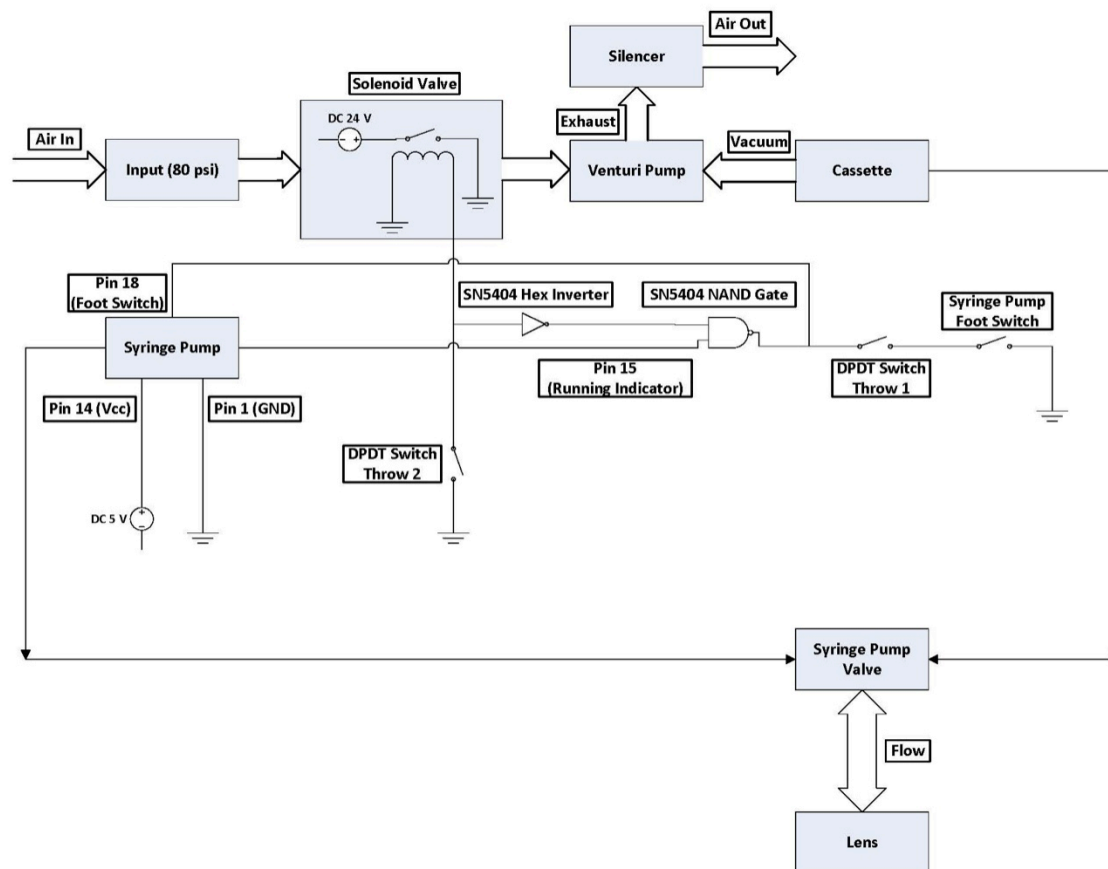


Figure 3-19. Schematic of infusion / aspiration system

The filling system was quantified in terms of accuracy with a series of lenses. Five lenses were measured on an analytical balance, then a target weight of 0.100 g was set based on the density of the silicone oil (0.967 g/ml). After infusion of the pump stopped, the infusion handpiece was left in the valve for two more minutes. This allows all capacitive pressure and volume in the lines to be released. With this technique, the final weight was measured and recorded after filling (Table 3-1). Table 3-1 demonstrates that the filling system is able to accurately inflate with a maximum error of 9 mg with these measurements.

Table 3-1. Weight values for a target weight of 100 mg

Trial	Weight (mg)	Error (mg)
1	101	1
2	91	9
3	104	4
4	104	4
5	91	9

3.6 Optical Test Methods

The optical test setup was modeled after Glasser [8] and was used to measure focal length of the lens. A 532 nm laser was scanned vertically along a diameter through the center of the lens. A few drops of fluorescein were added to the tank to visualize the beam as it traveled through the lens. A camera placed 90 degrees from the laser was used to capture an image of the laser as it passed through the lens.

The laser was scanned through the central 4 mm of the lens and 100 images were captured during the scan. A series of three scans were completed and the average power of the lens was reported.

A camera placed in line with the laser was used to visually inspect the tissue and lens during stretching. A schematic of the test setup is shown in Figure 3-20, a simplified picture of the testing setup is shown in Figure 3-21, and the full test setup is shown in Figure 3-22.

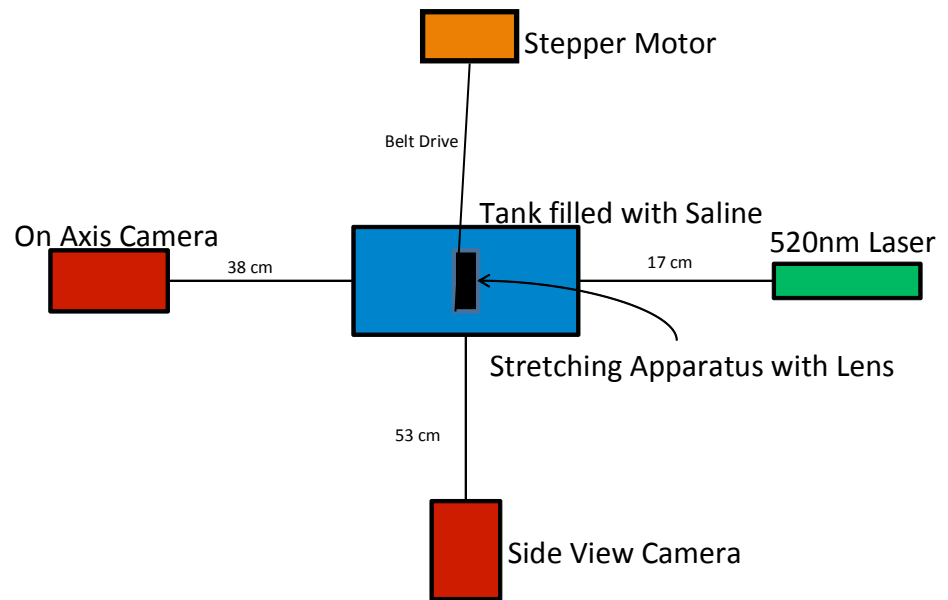


Figure 3-20. Accommodation test setup diagram.

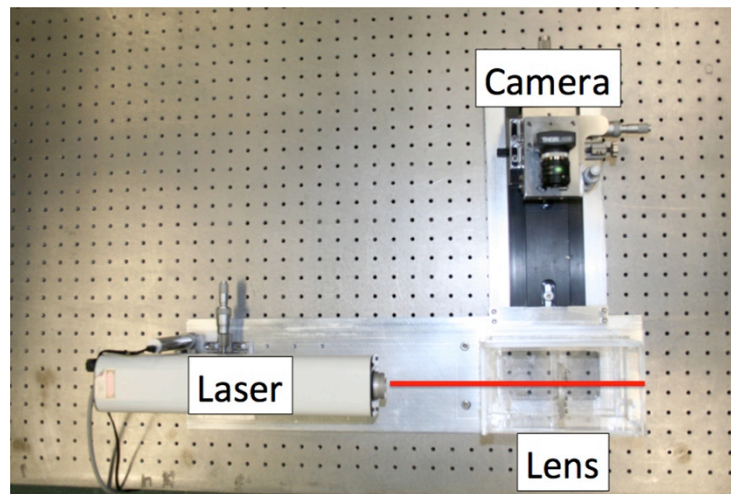


Figure 3-21. Basic test setup for measuring focal length of a lens. (On-axis camera and motorized stretching are removed for clarity). Side-view camera, laser, and unfilled tank are shown. The laser scans in and out of the page across a lens.

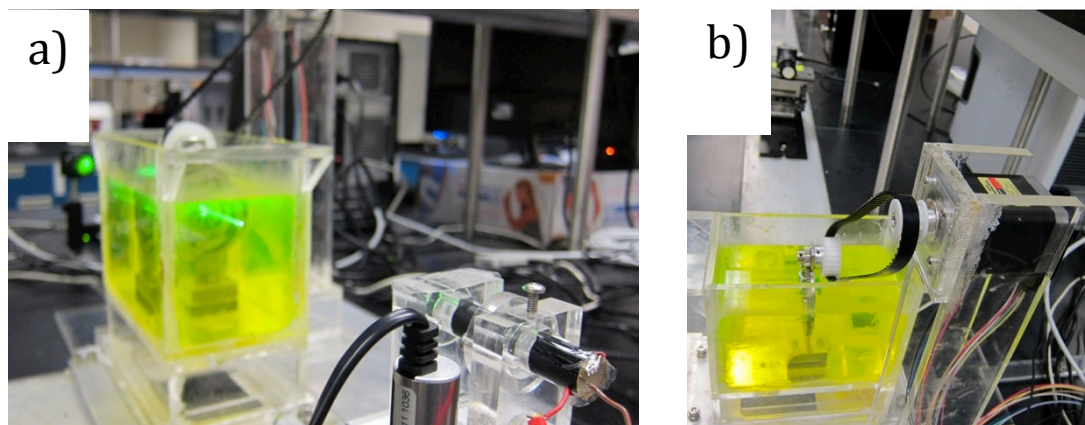


Figure 3-22. Accommodation test setup picture. a) Laser (bottom right) excites fluorescein in tank. b) View of belt drive attached to stretching apparatus

Image processing was completed to determine the focal length of the lens in water. After a series of 100 pictures were captured of the laser going through the lens across the central 4 mm, analysis was complete. An automated testing program was made to analyze the data.

As shown in Figure 3-23 a best-fit line was made through the center of the ingoing and outgoing ray for each of the 100 images. Then, these rays were combined onto a single image (Figure 3-24). The focal point was calculated as the point with the least spread in the y-direction of the image. The lens center was taken as the average center based on the images. However, lens centers that were outside the area between the two regions of interest were removed. This is because the lens sits between the incoming and outgoing beams. Therefore, if a lens center is found anywhere that is not between these two areas, it is known to be inaccurate and removed. Erroneous calculations of lens center are most prevalent when the beam is close to the center of the lens and the input / output beams are close to parallel.

The focal length was calculated as the distance between lens center and the focal point. However, to be comparable with ISO standard 11979-2, the focal power was taken as the inverse of focal power times the index of refraction of the saline tank. This is because IOLs are typically measured in air or in a small water tank, with focal point measurements taken in air.

To automate analysis, a program was made that brings up an overlay of the top and bottom images. A region of interest is asked for the incoming and outgoing beams. These are selected with a mouse as shown in Figure 3-25. This is done to remove analysis errors from stray light. Then the images are batch processed.

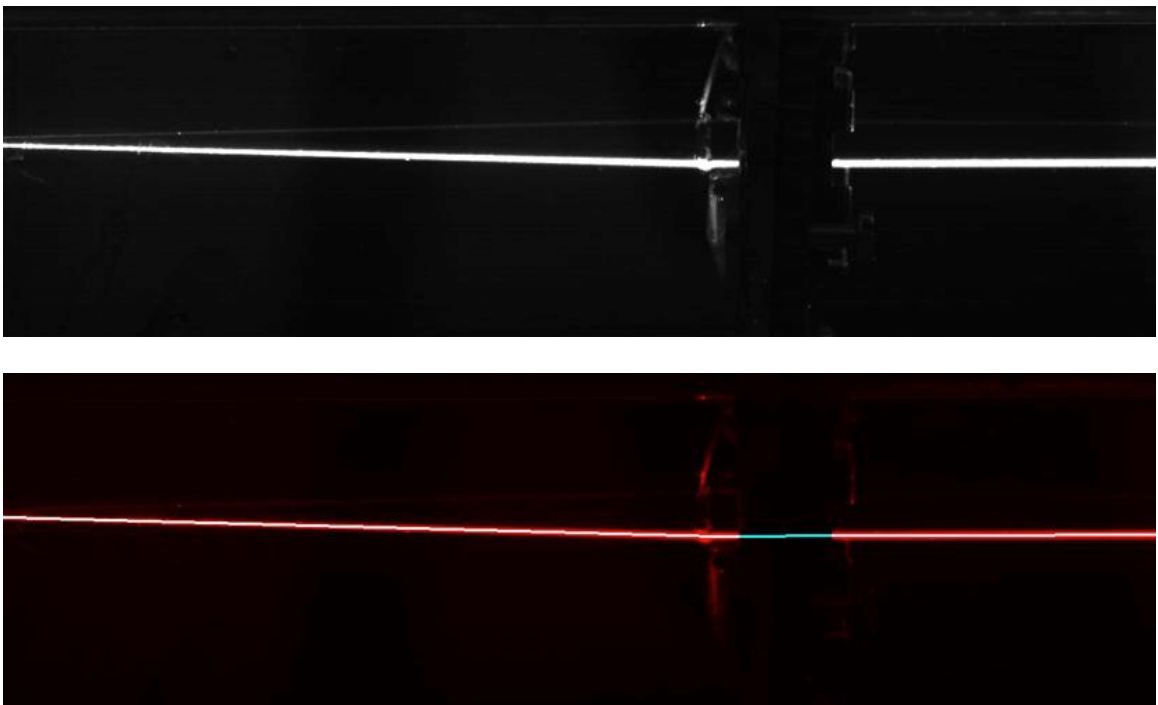


Figure 3-23. Single image of a laser going through lens (top). The beam passes from the right-hand side of the image into the lens and is deflected to an outgoing angle after passing through the lens. The detected incoming and outgoing laser beams are fitted with regression analysis (bottom). The intersection between the incoming and outgoing beams is recorded as the lens center for this particular image.

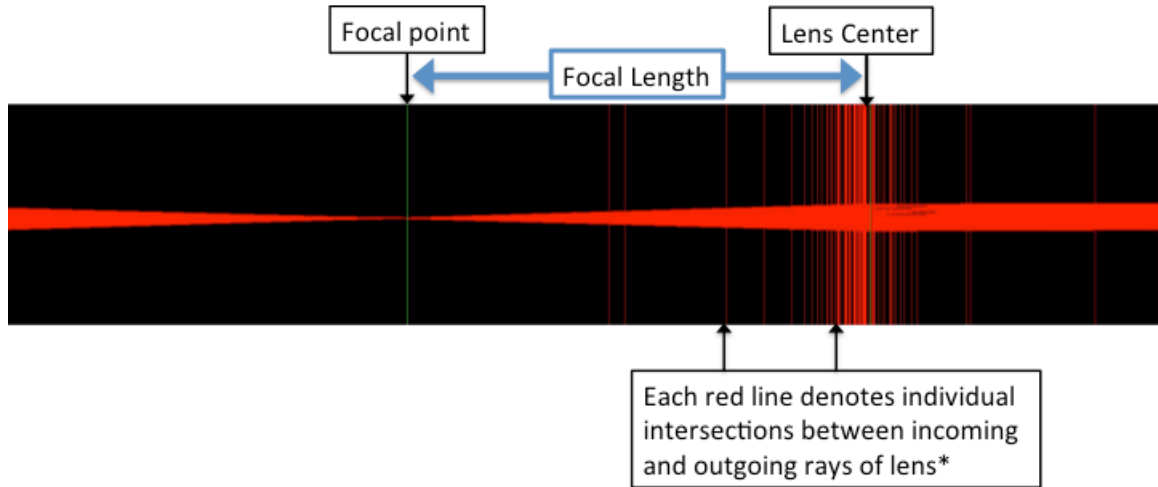


Figure 3-24. Analyzed data. The center of the beam for each image is detected and a line is fit. After all 100 images have been analyzed, they are overlaid on each other as shown. The focal point is determined as the point where the rays converge. The lens center is the average position where the ingoing and outgoing rays of the laser intersect. The focal length is the distance between these two positions.

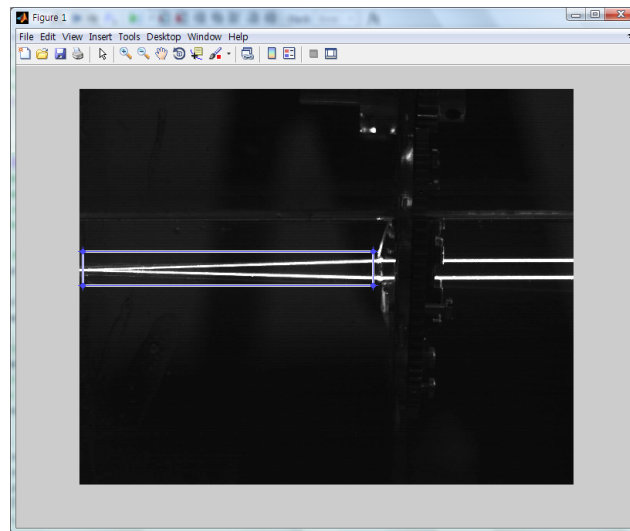


Figure 3-25. Automated analysis. The highest and lowest beams are projected onto the analysis program screen. The user selects a region of interest around the outgoing beam (shown here) and the incoming beam. All subsequent analysis for the pictures occurs in these regions of interest. This prevents stray light and scatters from damaging beam fit integrity.

3.7 Optical Test Setup Validation

The optical measurement system was validated with a series of six commercially available monofocal IOLs (AMO Technis Z9000, Z9001). IOL lens power varied from 17.5 to 26.0 diopters to ensure a similar range of power that would be tested on the accommodating IOL. The commercially available lenses were first measured directly. Then, three lenses were chosen to be measured after implantation into a porcine lens capsule. All power measurements were within 0.5 diopters of actual lens power (Table 3-2).

Table 3-2. The tabulated power refers to the power stated by the IOL manufacturer. The power was measured with the lens alone (not implanted) and implanted in a porcine lens capsule after the natural lens was removed. All values are within 0.5 D from the tabulated power.

TABULATED AND MEASURED POWER OF INTRAOCULAR LENSES		
Tabulated Power (D)	Measured IOL Power (D): Not Implanted	Measured IOL Power (D): Implanted
17.5	17.4	
18.0	17.9	17.9
19.0	19.2	
20.0	20.5	20.4
21.0	21.2	20.7
26.0	26.3	

3.8 Bench-Top Testing of Lens for Accommodation

To test the accommodation, a lens was implanted into the ciliary body of a cadaver eye. The ciliary body and lens complex was attached to a stretching apparatus (Figure 3-14) using cyanoacrylate and the entire assembly was submersed into a tank filled with 0.9% Sodium Chloride Irrigation Fluid that contained a fluorescent solute (fluorescein). A laser was then positioned outside of the tank so that the beam traveled through the central axis of the lens (see Accommodation Test Setup Diagram Figure 3-20). The lens was then stretched from 0 mm to 5 mm. The beam traveled 4 mm vertically across the center of the lens with 100 images taken incrementally showing the path of the beam as it passed through the lens. The images of the convergences of exiting rays were analyzed using a matlab script.

3.9 Conclusion

The procedure to test an accommodating intraocular lens has been developed. This work consists of developing a method to insert and inflate the intraocular lens inside a cadaver eye. In addition, the cadaver eye is dissected to remove the focusing mechanism. A stretching apparatus is used to actuate the dissected ciliary muscle to mimic the natural motion of the ciliary muscle. An optical system consisting of a laser scanner is used to ray trace ingoing and outgoing beams through the lens. This data is used to find the optical power of the lens. This system provides an automated method of testing a lens in a nonaccommodated and accommodated state. The difference in optical

power between the two states is found and considered optical power change due to accommodation.

4 ACCOMMODATING INTRAOCULAR LENS

4.1 Introduction

This chapter develops the requirements for an accommodating intraocular lens in terms of patient needs and surgical needs. Based upon these requirements, a lens consisting of a valve attached to a fluid-filled silicone bag is proposed and built. The valve is used to access the internal contents of the silicone lens for filling and refilling. It is characterized by finite element analysis and tested for adequate sealing pressures.

The lens is then implanted and inflated in porcine and human lens capsules using a custom-made lens inserter and fluidics system. Testing is performed on the lens to demonstrate accommodation. Methods to tune the lens power are discussed. Finally, experiments are conducted to demonstrate feasibility of lens tuning based upon fill volume and refractive index adjustment of the filling liquid.

The results from these experiments demonstrate a lens that can accommodate to clinically relevant levels, can be injected through a small incision, and has adjustable base power.

4.2 Requirements for an Accommodating Intraocular Lens

For an accommodating intraocular lens to be clinically useful to patients, it has several surgical and functional requirements. Surgical requirements describe how the implant is placed within the eye while functional requirements describe how the lens operates as an implanted device.

Surgically, the accommodating intraocular lens needs to be inserted in a manner consistent with current procedures. This allows surgeons to use their current surgical techniques to implant the device instead of requiring new training and a learning curve for a new device. As described in Chapter 1, a corneal incision diameter less than 3 mm is preferable as it leads to less postoperative astigmatism and allows wound closure without sutures. In addition, the device is injected through an IOL injector to enable the surgeon to deploy the lens in a simple manner. The total time to insert and inflate the accommodating intraocular lens should be less than 2 minutes, which is similar to existing intraocular lens implantations. In addition, shorter surgical times are correlated with better patient outcomes and lower operating room costs.

Functionally, the lens needs to accommodate at least 2 diopters after implantation. In addition, once implanted, the lens needs the correct base power within 1 diopter to provide emmetropia.

Optically, the lens needs to be at least 4.25 mm in diameter to prevent halos or light scatter. The lens optical quality needs to match the quality of existing intraocular lenses. ISO 11979-2 provides guidance for modulation transfer function (MTF) of a monofocal lens, and ISO 11979-3 provides guidance of optical characteristics for a

multifocal lens. As an accommodating lens, the MTF should be better than current multifocal lenses, although not necessarily as good as a rigid monofocal lens. This is because rigid materials and thin lenses allow very high resolution and MTF with monofocal lenses. However, with an accommodating lens, some of the optical resolution may need to be traded for accommodation ability.

To be implanted in the body, the implant must be made of biocompatible materials, preferably materials that have already been used for ophthalmic purposes. In addition, the lens must be able to be sterilized.

4.3 Overview of Lens Design

The biomimetic accommodating IOL is comprised of the accommodative lens and peripheral units. The biomimetic accommodating IOL is designed to mimic the natural crystalline lens. This design allows the entire optic to change anterior and posterior lens curvature for accommodation (Figure 4-1).

The optic body is constructed of a thin balloon that is filled after implantation with silicone oil through a peripheral injection port (Figure 4-2). This allows the lens to be used in small incision surgeries. The periphery of the lens is anchored to the lens capsule by a conformal fit.

The injection port allows addition or removal of the fluid inside the lens after lens insertion. The injection port is used during surgery as well as postoperatively to adjust base power of the lens to provide accurate and adjustable refractive power.

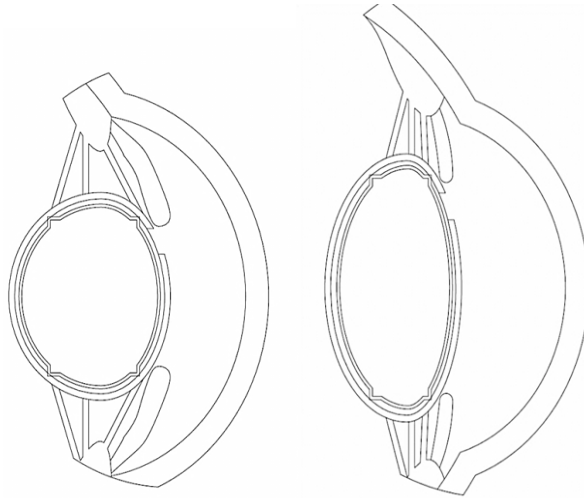


Figure 4-1. Biomimetic accommodating IOL: accommodated (left) and non-accommodated (right)

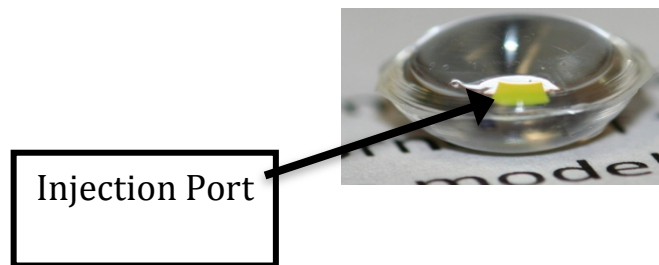


Figure 4-2. The injection port and accommodating intraocular lens

The lens is introduced through a small corneal incision into the lens capsule after removal of the natural lens as shown in Figure 4-3. During insertion and inflation, the lens sits within an injector with a fluid feed line attached to the lens injection port. After the lens is implanted into the lens capsule, the lens is filled with silicone fluid to the correct power. The lens inserter has the ability to insert and inflate the lens to the required dioptric power after insertion as shown in Figure 4-4. A self-sealing injection port closes after removal of the injector (Figure 4-5). This port is resealable and can be accessed for either lens adjustment post-implantation or to deflate the lens in the rare case that this

should become necessary. Therefore, the port allows postoperative adjustment to obtain emmetropia for patients even after the initial implant procedure.

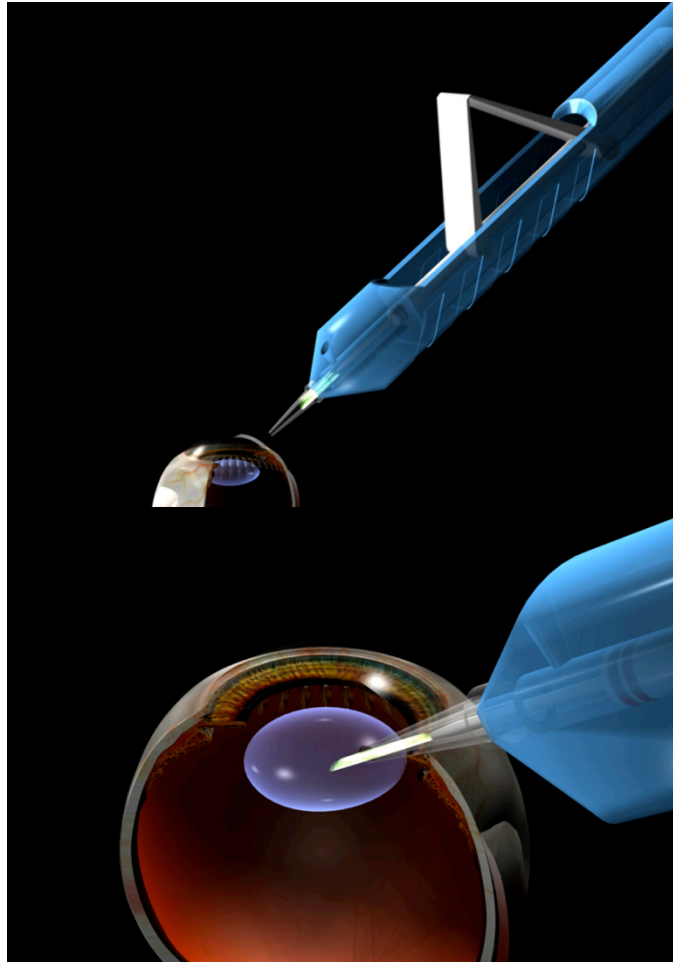


Figure 4-3. Insertion of the lens through a small corneal incision. After insertion, the lens is filled to the proper volume.

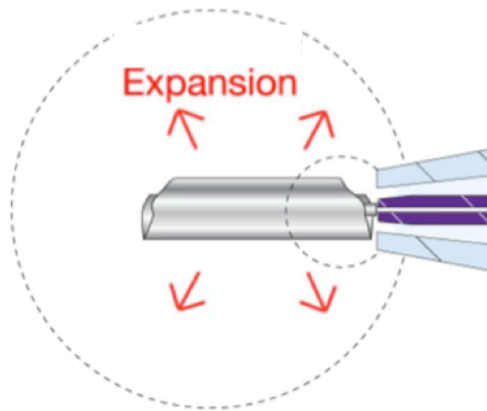


Figure 4-4. Lens filled to required optical power after insertion into the lens capsule (shown in dotted lines)

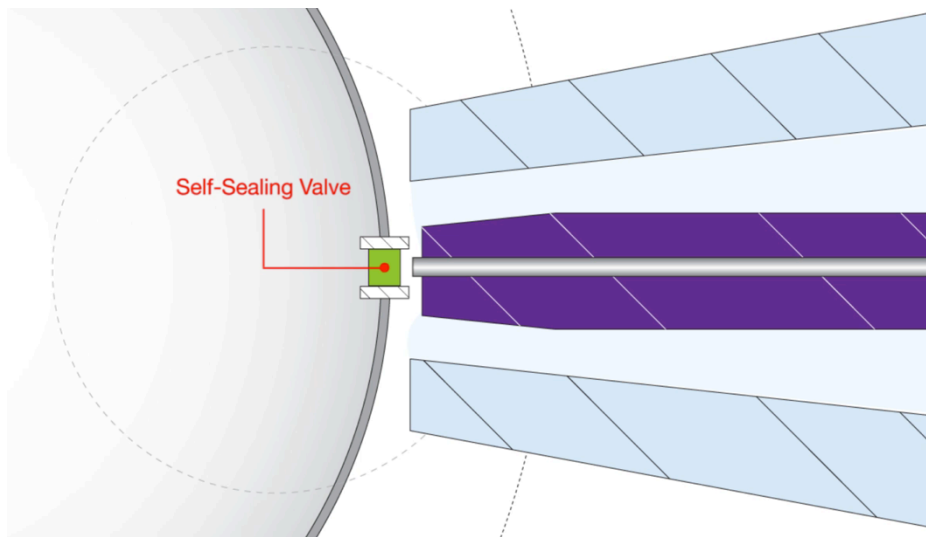


Figure 4-5. The self-sealing injection port closes once the lens inserter is finished filling. This port is accessible after insertion for subsequent adjustments to base power.

The following sections describe the design of the MEMS-enabled self-sealing injection port, the lens design, lens assembly, and performance characterization of the lens.

4.4 MEMS-Enabled Injection Port

The MEMS-enabled injection port was designed to allow inflation after insertion of the lens into the lens capsule. In addition, the port was designed for accessibility at a later date if more or less fluid inside the lens was required. The requirements of the port were to seal at a pressure higher than 1 psi, and to be accessible multiple times.

This MEMS valve is important because it allows a simpler and safer surgical procedure of inserting a deflated lens into the lens capsule before filling the lens. In addition, the colored valve allows the surgeon to identify the valve during the implantation and inflation procedure.

Two similar seal designs were examined. The first relied on a self-sealing silicone membrane and was used for the accommodating IOL. The second design is intended for use in higher-pressure applications. It is based on a composite silicone / parylene design.

4.4.1 Design for Use with Accommodating IOL

To determine the sealing efficacy of the MEMS valve, a series of various thickness membranes were made and tested for leaking pressure after an incision was made.

The resealable micro membranes were fabricated from a USP VI (implantable) silicone elastomer to ensure biocompatibility with cells and other media. Thickness of the membranes varied from 28 μm to 160 μm and incisions were made with stainless steel hypodermic needles ranging from 110 μm to 514 μm . Thin membranes were fabricated by spincoating a USP VI silicone elastomer (i.e., NuSil 6015) on hexamethyldisilazane-

treated silicon wafers. After curing, small sections were cut and peeled from the wafer and mounted on a pressure chamber (Figure 4-6). The membranes were fixed between two plates with coinciding 1/16 inch diameter holes. An incision was made in the center of the membrane with a hypodermic needle. A drop of water was applied to the top side of the membrane and pressure was applied to the bottom. Pressure was raised in 0.1 psi increments while an observer checked for leakage.

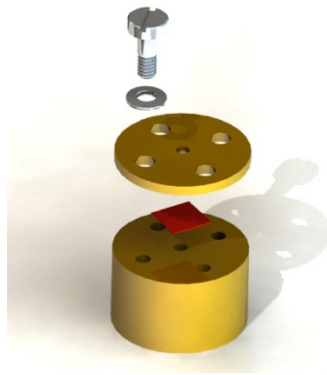


Figure 4-6. Pressure chamber used to measure resealable membranes.

Experimental data demonstrated that the sealing/cracking pressure of the membrane increased dramatically as the membrane thickness increased (Figure 4-7). For a 210 μm incision, leakage occurred at 0.46, 0.86, and 5.74 psi for 28 μm , 105 μm , and 160.5 μm thick membranes, respectively. Similarly, smaller diameter incisions held higher pressures than larger diameter incisions. In the 160.5 μm thick membrane the 110, 185, 311, and 514 μm incisions had respective cracking pressures of 11.7, 6.5, 4.9, and 0.6 psi.

Large displacement finite element analysis was performed in Comsol Multiphysics to explain the results. For an example, simulation was performed with a

311- μm -long by 1- μm -wide incision on membrane thicknesses of 28, 54.5, 105, and 120 μm . To increase stability and reduce computation time, one quarter of the circular valve was modeled, with symmetry constraints along the radial edges and a free edge along the incision (Figure 4-8). The circumferential peripheral edge of the membrane was assumed to be clamped at zero displacement and slope. Because the incision was a free edge, it was able to move across the symmetry plane, causing negative incision widths. This physically represents a compression of the incision. Pressure was varied from 0 to 2 psi in 0.2 psi increments and the incision width at the top and bottom surfaces of the membrane were measured. Finite element analysis showed the top incision continually widening. For thicker membranes at low pressure, the lower surface initially underwent a negative displacement (negative incision width), which would represent a compression of the lower portion of the seal, followed by expansion (Figure 4-9). The pressure required for the entire seal open (both upper and lower incision widths greater than zero) was plotted next to the experimental data. Simulated data correlated well with experimental data and displayed the same trend of increasing rapidly with membrane thickness (Figure 4-10, Figure 4-11). Simulated data was slightly lower than experimental data, which is consistent with stiction in the membrane seal during the experiments.

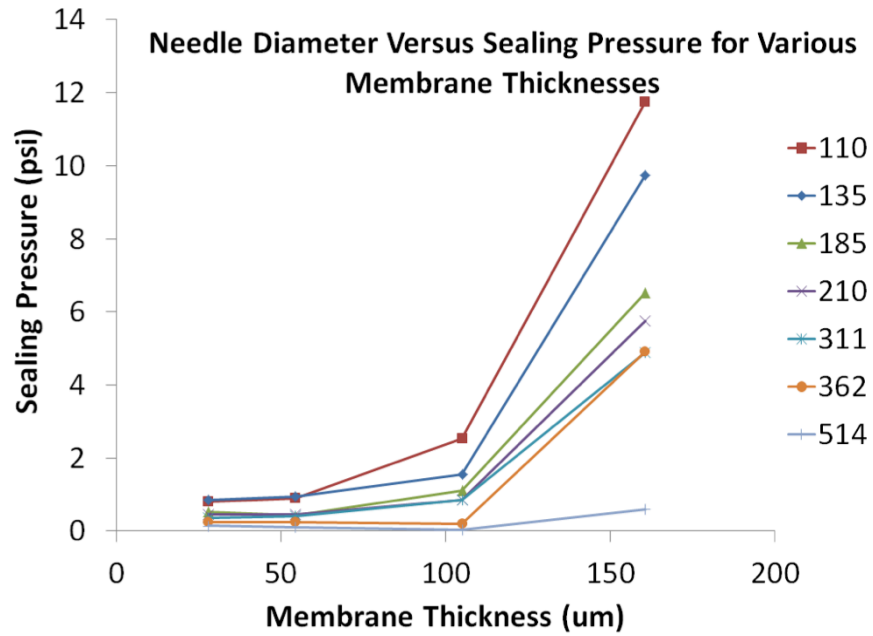


Figure 4-7. Needle diameter versus sealing pressure for various membrane thicknesses. Membrane thickness is listed on the horizontal axis, while sealing pressure is on the vertical axis. The differing curves correspond to differing incision diameters, which are listed on the right-hand-side legend.

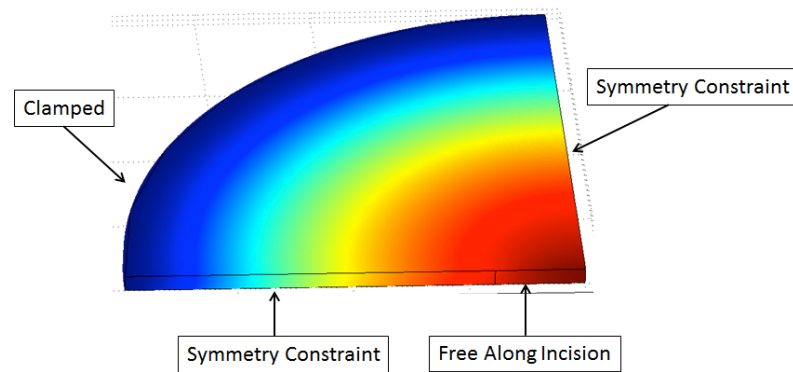


Figure 4-8. Schematic of finite element analysis boundary conditions

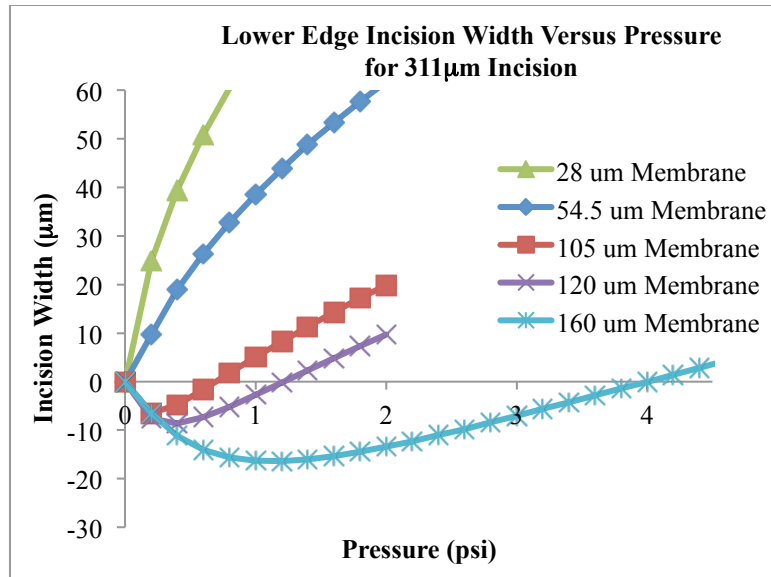


Figure 4-9. Simulation of lower edge incision versus pressure. When the incision width is positive, the seal is assumed to be leaking. When the incision width is negative, the seal is assumed to be sealed. 28 through 160 μm membranes are shown. Both the 28 and 54.5 μm membranes do not seal at any pressure from these simulations. From observing where the lines cross the x-axis, it is evident that the 105 μm seals to 0.7 psi, the 120 μm seals to 1.2 psi, and the 160 μm seals to 4 psi.

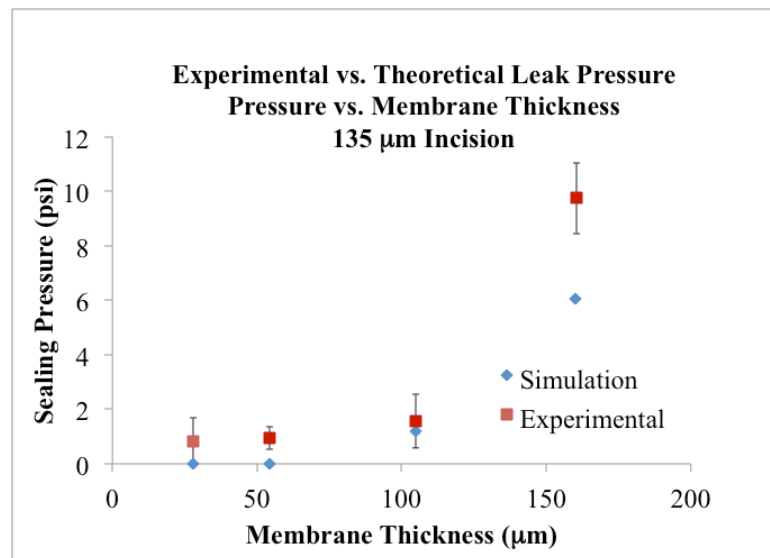


Figure 4-10. Simulated versus experimental cracking pressure of 135 μm incision

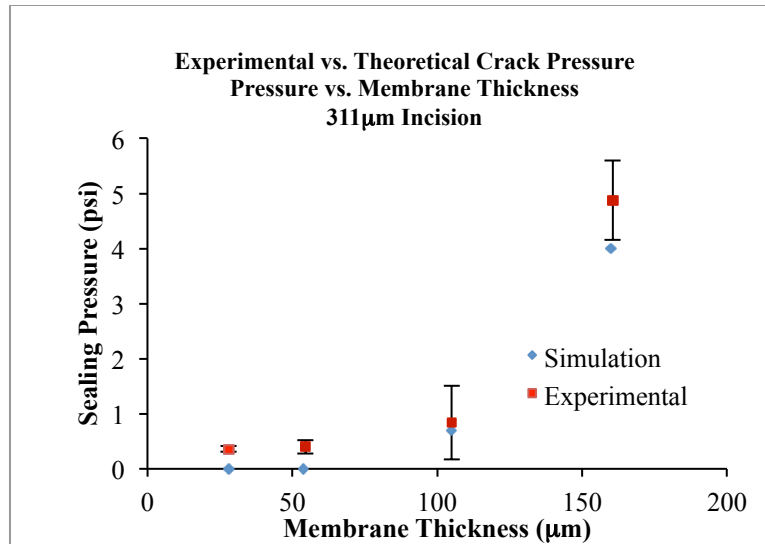


Figure 4-11. Simulated and experimental data for a 311 µm incision. Based upon this data, sealing pressure increases with membrane thickness. Therefore, to allow a factor of safety in the valve design, a 250 µm valve was fabricated.

Based on the experimental and simulated data, the thickness of the MEMS refill valve was determined to be 250 µm to ensure sealing of the valve at nominal lens pressures with a factor of safety.

4.4.2 MEMS-Enabled Injection Port for High-Pressure Applications

Although not used on the current intraocular lens, further testing of resealable membranes was completed for use in other high-pressure applications. The finite element analysis of the valves demonstrated that the valve leaks due to deformation of the valve surface and the incision. When deformation is too high, the incision goes from compression to tension and opens. Therefore, a valve was designed encapsulated in parylene to prevent deformation, and hence leakage. In addition, this valve was tested for resealing capability.

For operation at high pressure, a seal thickness of 250 μm and a 110 μm injection needle were used. Additionally, parylene-C was used to encapsulate and reinforce the valve. This was intended to reduce deformation of the valve and therefore increase the leaking pressure. The periphery of the seal had an outer ring to mechanically retain the seal in the parylene (Figure 4-12). Fabrication of the device is shown in Figure 4-13.

The valve was tested for sealing on both sides. A 110 μm incision was made, the valve was mounted on a pressure chamber, 20 psi was applied, and the seal was visually inspected for leakage. The valve was flipped and pressure was raised until the valve failed. In half the experiments, the valve was set in the nominal configuration first. In the other half, it was set in the flipped configuration first.

In addition, the valve was tested for its ability to seal after multiple insertions. An initial 110 μm incision was made. The valve was evaluated for its ability to seal with 10 psi of water pressure after repeated insertions with a blunt injection needle. The valve was tested at least 20 times or until it leaked.

Four of five tested valves sealed to 20 psi in the nominal configuration, while none sealed to 20 psi while flipped. Sealing pressure was 16 \pm 3 psi when the valve was in the flipped configuration. Four of the five valves tested were able to reseal 20 times, while one leaked after the second re-insertion (Figure 4-14).

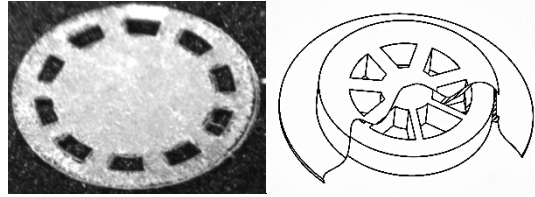


Figure 4-12. Fabricated valve. Parylene encapsulates and reinforces a silicone elastomer valve. The central section is the injection port. The surrounding annulus is used to retain the valve in the parylene.

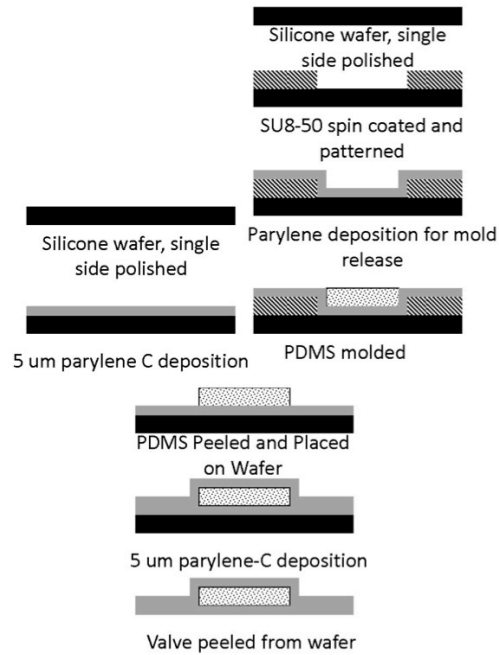


Figure 4-13. Valve fabrication process

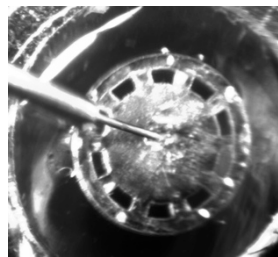


Figure 4-14. Injection into fabricated valve

This data indicates that parylene can be used to reinforced the valve and increase sealing pressure. Pressures over 20 psi were demonstrated with this seal design. Uses for a high-pressure seal include microfluidics as well as drug delivery systems.

4.5 Lens Body and Assembly

The lens body is designed to emulate the natural eye. When used with 100 cst silicone oil, the dimensions of the lens are a 90% scaled 29-year-old human lens to ensure a good fit inside the lens capsule. When used with 1000 cst silicone oil, the dimensions of the lens are a 100% scaled 29-year-old human lens. Dimensions for the lens were taken from Burd [29].

The lens is constructed of a silicone elastomer (Nusil, MED4-4210) to mimic Young's modulus of the human lens capsule (1.3 MPa silicone versus 1.5 – 6 MPa in human [29]) and capsular thickness (30 μm versus 3 - 21 μm in human [29]).

This lens body is fabricated by spin coating the silicone elastomer on two molds, one corresponding to the anterior half of the lens, the other corresponding to the posterior half of the lens. After spin coating, the two halves are clamped/fused together and placed in a convection oven to cure. An image of one half of the lens mold is shown in Figure 4-15.



Figure 4-15. One half of the lens mold

The MEMS refill valve is fabricated by molding using the sealing characteristics described previously. It consists of a colored silicone molded in a 250- μm -thick SU8-100 mold. The valve is peeled from the mold, and glued to the anterior segment of the lens (Figure 4-16). The valve is placed away from the central 5 mm of the lens to prevent visual disturbances. After attaching the MEMS refill valve to the lens, an incision is made in the refill valve to allow silicone oil to be injected into the body of the lens after surgical implantation. An image of a filled lens is shown in Figure 4-17.

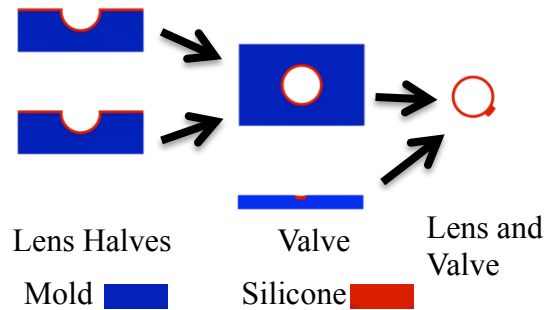


Figure 4-16. Fabrication process. The anterior and posterior lens halves are spin coated with silicone. Next, the two halves are fused together and the silicone is cured. A MEMS refill valve is molded from an SU8 mold and then glued onto the lens for the last step.

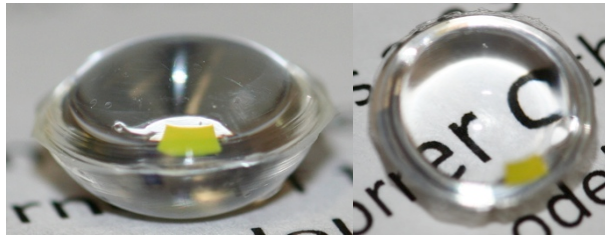


Figure 4-17. Lens prototype. The lens consists of a 30 μm silicone elastomer shell fused on two halves around the equator. The entry valve (yellow) is used to inject silicone fluid into the lens.

4.6 Conclusion

An accommodating intraocular lens design, which allows for accommodation, tunable base power, and implantation through a small surgical incision, is disclosed. Biocompatible materials are used to build the device in the cleanroom. A MEMS-enabled refill valve is modeled using finite element analysis and tested for sealing pressure and repeated punctures. By fusing the MEMS-enabled refill valve to the lens body, a lens is constructed that can be inserted and then inflated. In addition, the internal contents of the lens can be accessed at a later date for adjusting power.

5 LENS MECHANICS

5.1 Introduction

Previous chapters discussed the need and requirements for an accommodating intraocular lens, materials that can be used for such a lens, and a lens design that meets the requirements. This chapter discusses how the lens functions within the lens capsule. To study this, the natural lens is observed in the lens capsule during stretching experiments. Next, an artificial lens capsule is developed and stretched in a manner similar to tissue. Lens deformation and internal pressures are observed by using a custom built Scheimpflug imaging system and pressure monitoring system. Methods to adjust base power are explored and the effect of fill volume on accommodation and base power is studied in human ocular tissue. A finite element model is made of the lens to compare deformation measured with simulation. Finally, lens performance is validated in porcine and human eye tissue.

5.2 Natural Lens Stretch with Different Capsulotomies

A natural porcine lens was used as the experimental model to determine the effect of the capsulotomy on accommodation of the lens. Base power and accommodation of the lens were monitored before capsulotomy, after an anterior capsulotomy, and after anterior and posterior capsulotomy. The data from this study was used to design the surgical incision used with the biomimetic accommodating intraocular lens.

A natural porcine lens under 7 months of age was mounted into the stretching apparatus and evaluated for base power, accommodation level at 3 mm of ciliary muscle stretch, and slippage of the lens with respect to the lens capsule. The lens was tested in three configurations: no capsulotomy, anterior capsulotomy, anterior and posterior capsulotomy. An ink mark extending across the lens and the capsule was used to check for lens slippage with respect to the capsulotomy. Any discontinuity in the ink mark was indicative of slippage between the lens and lens capsule.

Base power for the three configurations is shown in Figure 5-1. An increase in base power was seen after the anterior capsulotomy was made. Base power increased further with both the anterior and posterior capsulotomies. Photographs of the natural lens indicated a bulging of the natural lens after the capsulotomy was made (Figure 5-2). This bulging from the capsulotomy site changed the curvature of the lens; and therefore, changed the base power. The increase in power seen as the capsulotomies were performed is consistent with the decreased radius of curvature due to the bulging.

Base Power: Natural Porcine Lens

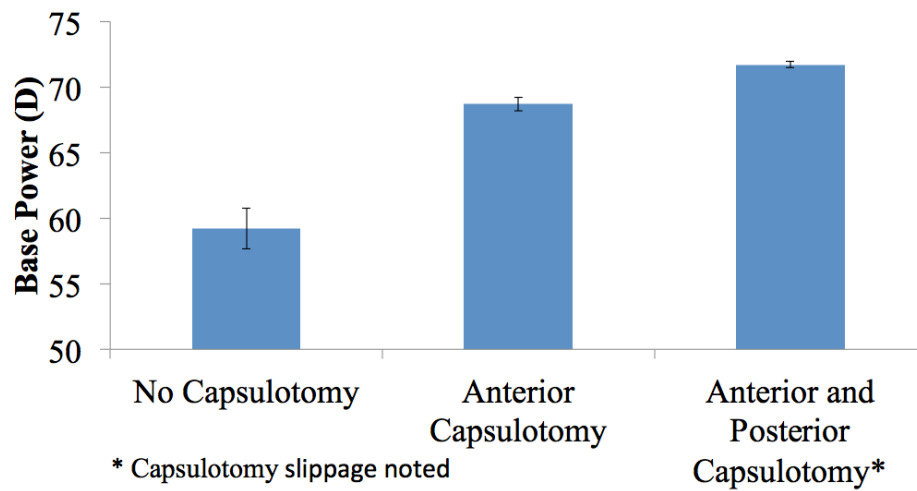


Figure 5-1. Base power for several capsulotomies in a porcine lens. Base power increases with capsulotomies. This is consistent with bulging of the lens at the capsulotomy site seen from photographs of the lens.

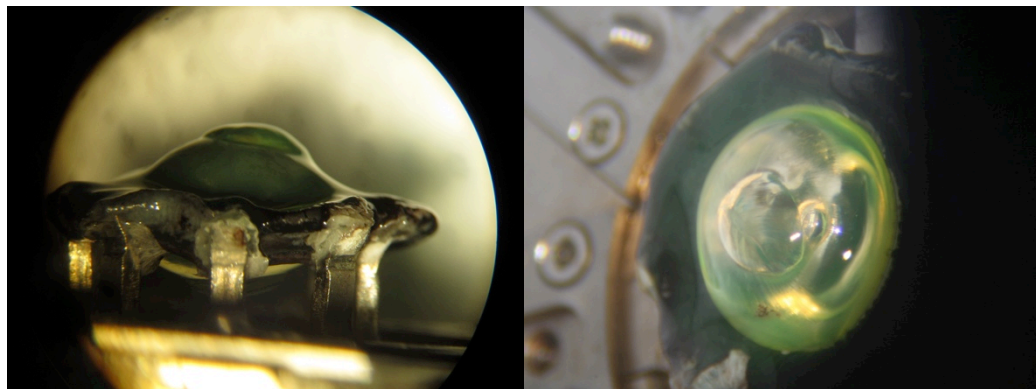


Figure 5-2. Side and top view of the capsulotomy. The lens is seen to bulge from the capsulotomy, increasing base power.

Accommodation for the three lens configurations is shown Figure 5-3. Accommodation was positive for the natural lens and the natural lens with the anterior capsulotomy. However, a negative accommodation was seen with both the anterior and the posterior capsulotomy. This indicates that the lens worked in a manner opposite to the

intact natural lens. In addition to reverse accommodation, a discontinuity was seen in the line crossing the capsule when there was both anterior and posterior capsulotomies (Figure 5-4). This indicated a slippage of the lens across the capsulotomy. Therefore, it is believed that once the lens has a slip condition with the lens capsule, instead of being pulled flat from the tensional forces of the lens capsule, the lens bulges out and increases in optical power during stretching.

No slippage was seen when only the anterior capsulotomy was made. This indicates that if there is stiction between the lens and the lens capsule, the lens capsule adequately applies a tensional force to the lens, causing it to flatten out. This can occur, even if there is a hole in the capsule, such as in the case of a capsulotomy. This is seen because accommodation between no capsulotomy and anterior capsulotomy are similar. However, if the lens begins to slip across the capsule, it is free to bulge out of the aperture with increased pressure and reverse accommodate. This causes an increase in optical power, and accommodation in the reverse direction as seen by the natural lens.

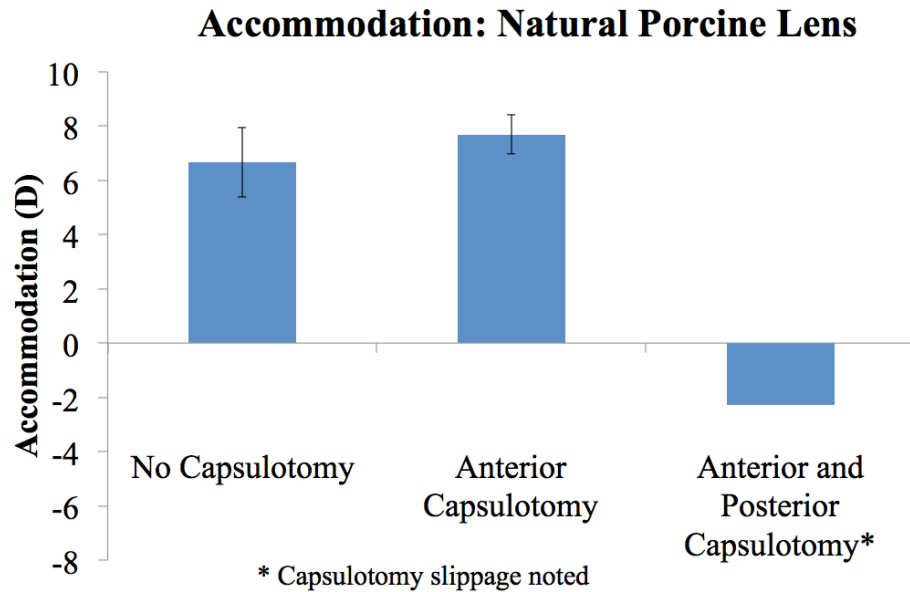


Figure 5-3. Accommodation levels of a porcine lens with no capsulotomy (left), 5 mm anterior central capsulotomy (middle) and 5 mm anterior and posterior capsulotomies (right)

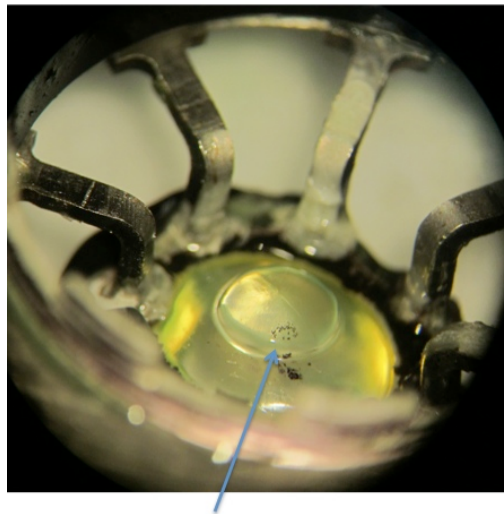


Figure 5-4. Arrow marks the discontinuity in ink placed across capsulotomy. This indicates a slippage of the lens through the capsulotomy during stretching.

The data taken from the natural lens and the capsulotomy indicates that the capsulotomy can interfere with optical performance of the natural lens. This is especially

evident when the lens slips across the lens capsule. Here, this is believed to have caused reverse accommodation. Therefore, with the biomimetic accommodating intraocular lens, a capsulotomy is placed slightly off center.

5.3 Artificial Lens Capsule

An artificial lens capsule was developed in order to study lens mechanics in a repeatable manner. The capsule is built with a slightly decentered capsulotomy to allow insertion and subsequent inflation of the biomimetic accommodating intraocular lens. In order to stretch in a manner similar to the existing lens capsule, an equatorial Saturn ring is placed on the artificial capsule, with a series of eight holes that attach it to the stretching apparatus described in Chapter 3: Measuring Accommodation. By stretching the equatorial ring of the lens capsule, the lens capsule deforms in a manner similar to tissue mounted in the stretching apparatus.

An image of the isolated artificial capsule with a lens implanted is shown in Figure 5-5. Figure 5-6 shows the artificial capsule mounted to the stretching apparatus with no lens implanted and Figure 5-7 has the artificial capsule attached to the stretching apparatus with the lens implanted.

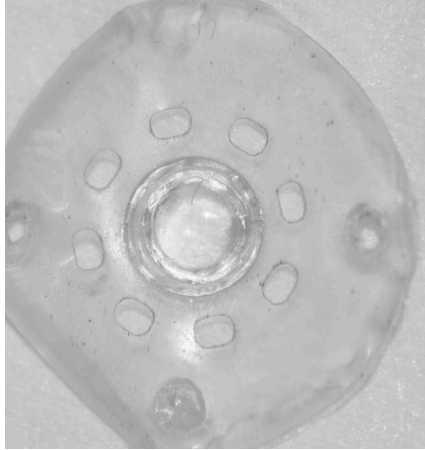


Figure 5-5. Artificial capsule with lens implanted inside

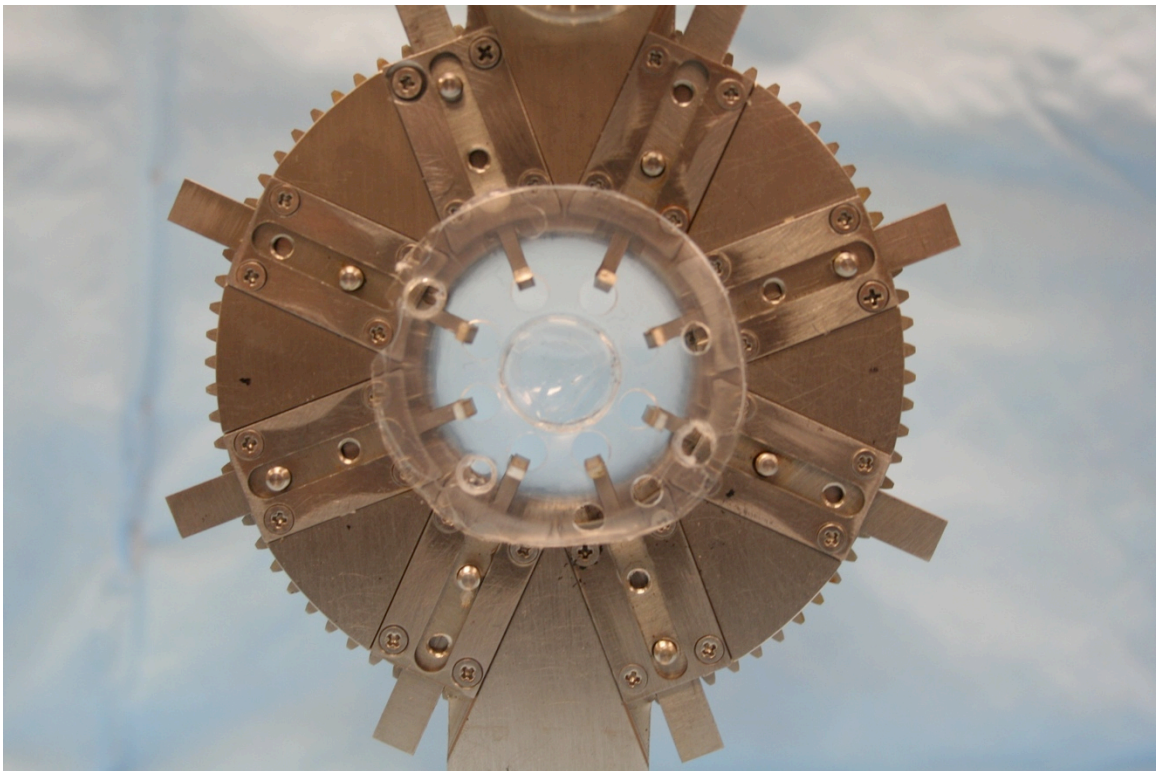


Figure 5-6. Artificial capsule attached to the stretching apparatus with no lens implanted

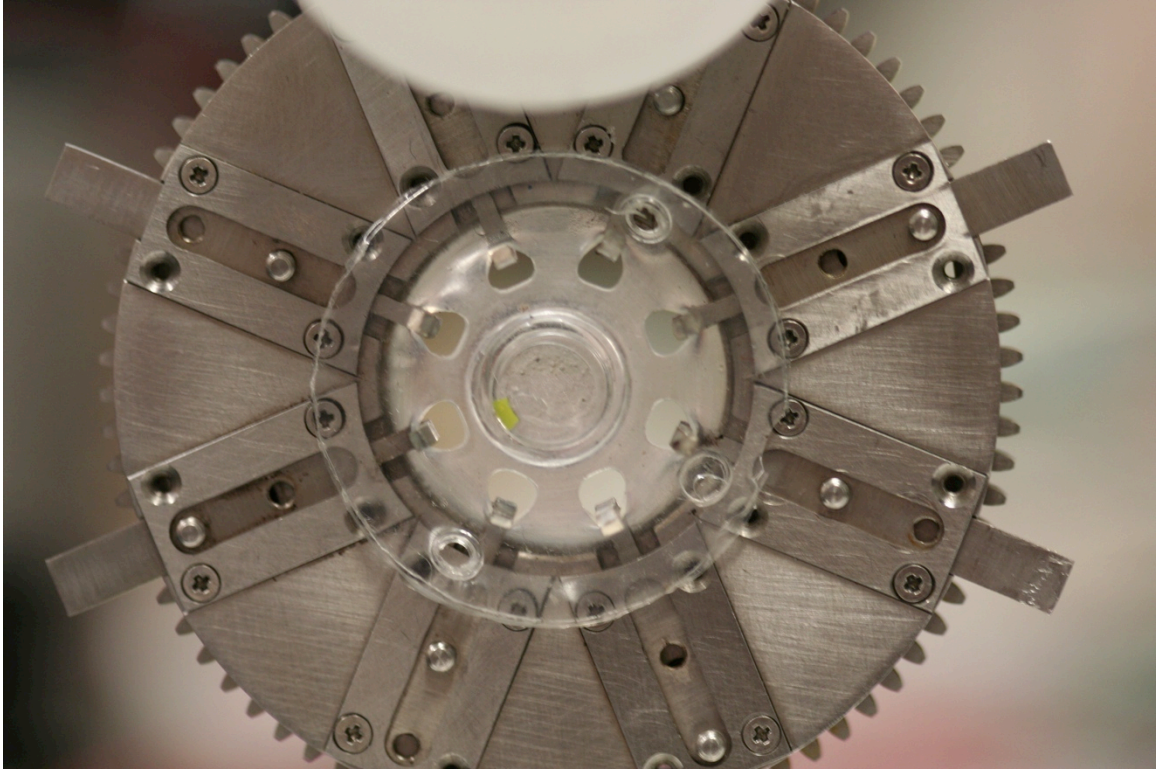


Figure 5-7. Artificial capsule in stretching apparatus with lens implanted. Artificial capsule is being stretched by jaws in this image.

Although the artificial lens capsule is an approximation of the human tissue, it has several advantages. First, because it is fabricated in the cleanroom with controlled conditions, the capsule has less variance than surgically dissected tissue. Second, because the equatorial ring on the artificial lens capsule is similar from capsule to capsule, and mounting holes are cut directly into the capsule itself, there is less variability in mounting into the stretching apparatus. In addition, an artificial capsule is robust and allows many measurements without degradation of the tissue.

Due to the increased repeatability of the artificial capsule relative to real tissue, refinements in lens design can be tested in the artificial capsule in a more efficient manner. Finally, the artificial capsule does not require a donor, saving precious tissue and

conserving cost. Therefore, the artificial capsule is viewed as a promising technology for future accommodating intraocular lens development.

The artificial capsule geometry is modeled after a 100% scaled 29-year-old human lens capsule. It is made with an equatorial ring with eight holes that attach into the jaws of the stretching apparatus. In this manner, it is stretched as shown in Figure 5-7. The thickness of the artificial capsule is 60 μm , which is thicker than the natural human capsule.

As shown in Figure 5-8, the artificial capsule is fabricated with a process of spin coating and laser cutting. The left side of Figure 5-8 shows the anterior side of the artificial capsule fabrication, while the right side shows the posterior side of the artificial capsule. First, the anterior side of the capsule is spin coated and cured. Then, a capsulotomy is laser cut into the anterior half of the artificial capsule with a laser cutter. Then, the posterior side is fabricated. First, a thick Saturn ring is spin coated and cured outside of the lens area. Then, a second thin layer is spin coated to make the posterior lens. While still uncured, the two halves are pushed together and cured, forming the artificial capsule. Finally, a laser cutter is used to place the eight mounting cutouts in the Saturn ring.

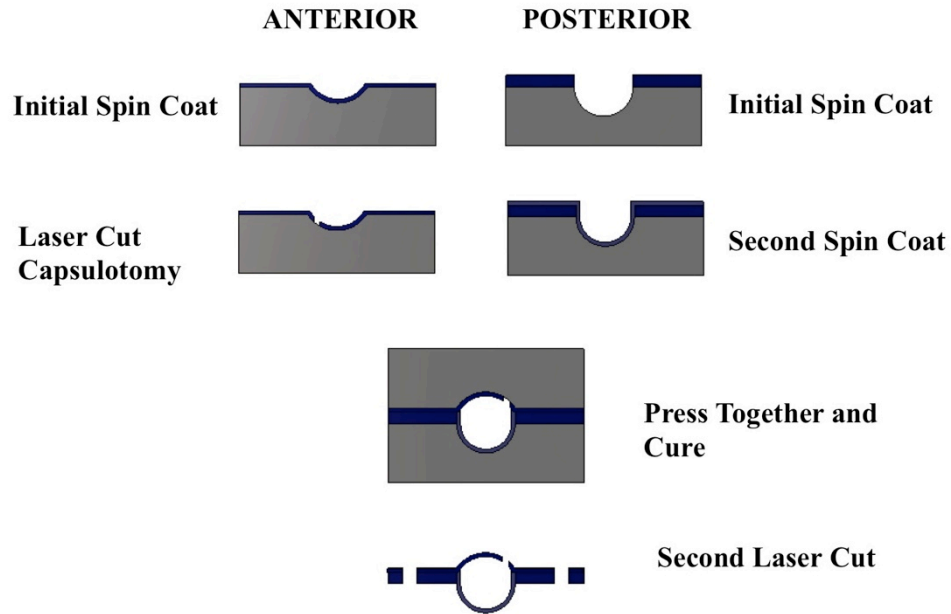


Figure 5-8. Fabrication for artificial capsule. Gray corresponds to the lens mold. Blue corresponds to silicone.

5.4 Scheimpflug Camera System

In order to measure the profile of the lens during accommodation a Scheimpflug imaging system was made. This system consists of a laser line illumination that is shined through the lens to illuminate a cross-sectional view of the lens, and a camera to capture the image. An image of the artificial lens capsule and slit illumination source are shown in Figure 5-9.

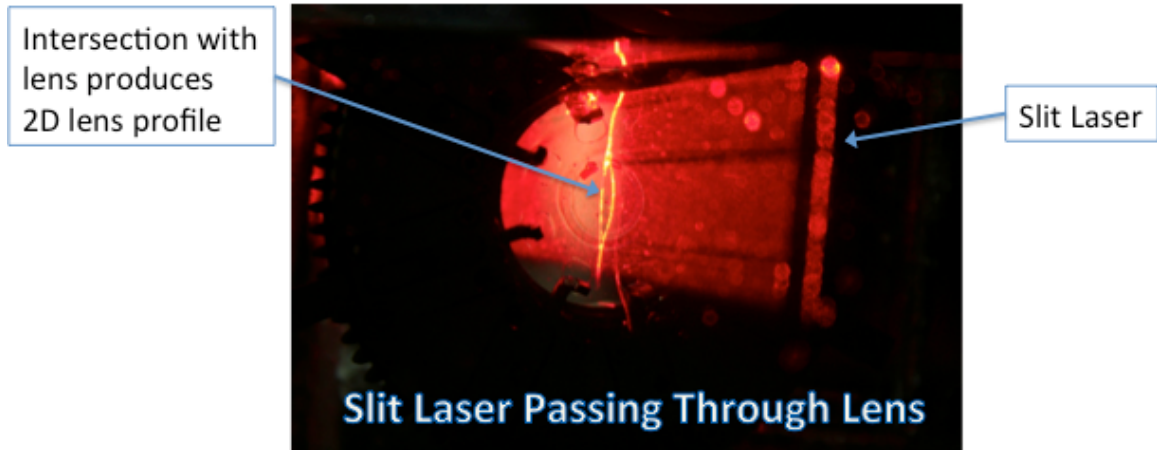


Figure 5-9. Slit illumination of the lens in the artificial lens capsule. The laser scatters off the edges of the lens and artificial lens capsule, giving an illuminated cross-sectional view of the lens and artificial lens capsule.

Ideally, the slit illumination would be viewed from the side and a photograph would be taken to obtain all values for the lens geometry. However, the sides of the Saturn ring of the lens capsule and the stretching apparatus occlude this view. Therefore, the camera is placed at a 45-degree angle to the front of the lens. In order to maintain focus along the slit laser path, the image plane of the camera (the CCD sensor) is placed at an angle defined by the Scheimpflug principle. In addition, to avoid distortion of the back surface of the lens due to the refractive powers of the front surface of the lens, the lens is mounted in a liquid with an identical index of refraction. This is accomplished by either filling the lens with water (and the tank with water) or matching the index of the two using sugar water in the tank. A schematic and photograph of the Scheimpflug camera setup is shown in Figure 5-10.

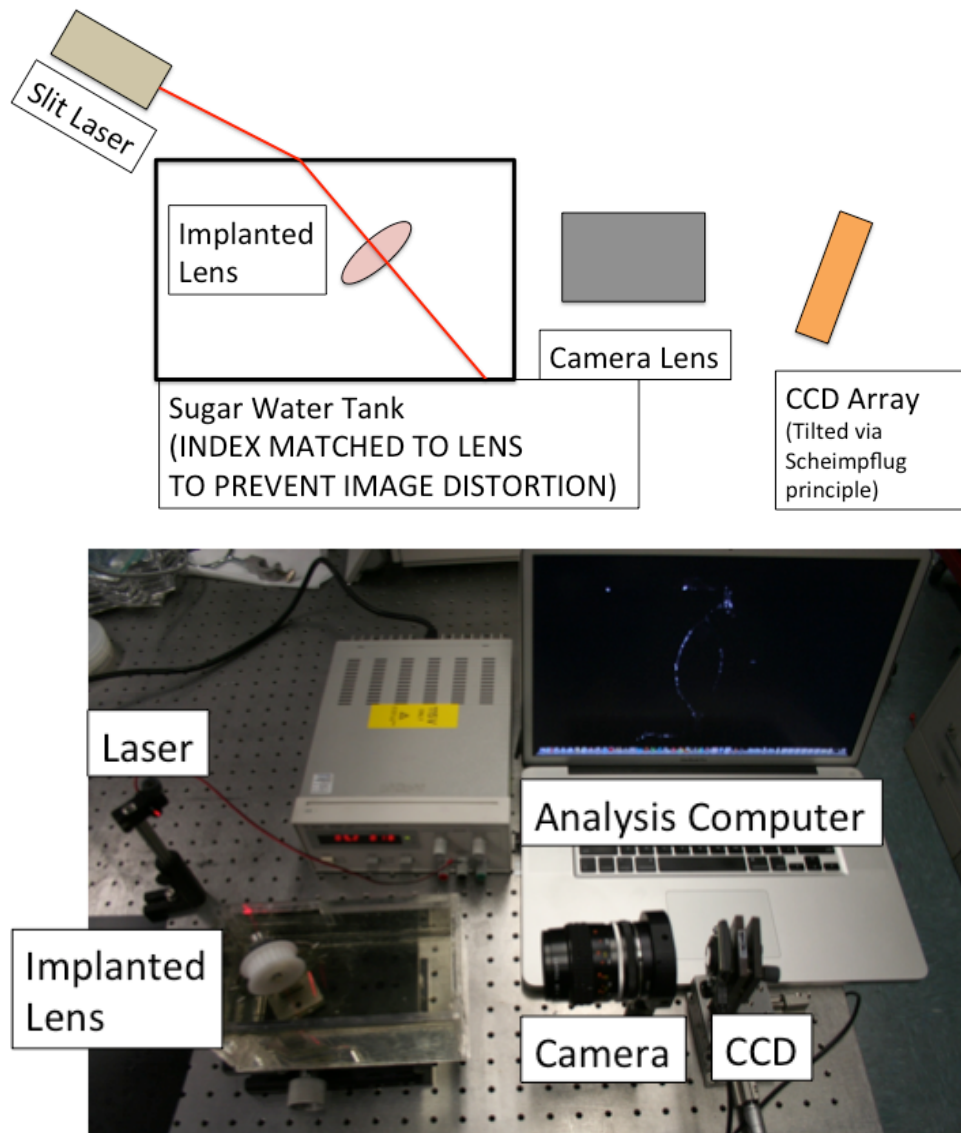


Figure 5-10. Schematic (above) and picture (below) of Scheimpflug camera system

The Scheimpflug principle explains why the imaging plane is tilted relative to the subject plane. The Scheimpflug principle relates to maintaining an object in focus that is not parallel to the lens plane. It states that the intersection of the image plane, object plane, and lens plane occur along a line (or point as seen from a bird's eye view). This is shown Figure 5-11. Therefore, the CCD array must be tilted in order to bring the lens into focus.

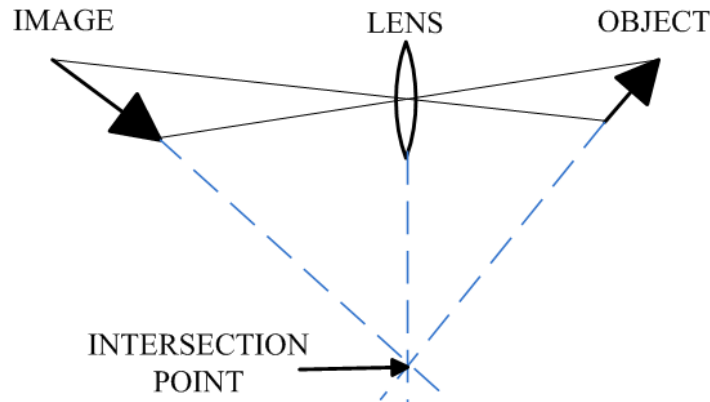


Figure 5-11. Scheimpflug principle [84]

Because the subject plane is at an angle to the sensor plane, images from the Scheimpflug camera need to be calibrated. This is done by imaging a target consisting of a series of square boxes of a known width. Based on this, the scale factor of the camera along both the x- and y-axes can be determined. Then, the image can be undistorted and a best-fit circle of the anterior and posterior surfaces can be determined using matlab and image analysis. The data from the circular fits is used to calculate optical power of the system using the thick lens equation.

To validate the Scheimpflug system, measurements from the laser scanning apparatus and the Scheimpflug setup were compared. On the laser scanning apparatus, the measured power was determined to be 18.39 diopters, while on the Scheimpflug setup, it was determined to be 18.42 diopters, with a difference of 0.03 diopters. This indicates that the calibration of the Scheimpflug system was accurate. However, subjectively, more variation is seen with Scheimpflug analysis due to the curve fitting along the surfaces of the lens. Analysis of the same images can cause variation of the

power by up to one diopter with this setup. Therefore, in this thesis, the Scheimpflug imaging system was used to determine how the surface geometry of the lens changed, while dioptric power values were determined from the laser scanning apparatus.

Table 5-1. Validation of Scheimpflug imaging system

Measurement Technique	Optical Power (D)
Laser Scan	18.39
Scheimpflug Camera	18.42
Error	0.03

In addition to validation, the same lens was stretched both on the laser scanning apparatus and on the Scheimpflug imaging system. The results demonstrated similar results between the two methods as shown in Table 5-2. Discrepancy between the two measurements is due to errors in both imaging systems as well as variation in the lens / stretching apparatus during multiple stretches.

Table 5-2. Lens stretching on the laser scanning apparatus and the schiempflug imaging system

	Laser Scan	Scheimpflug
Stretched Power	18.2	18.4
Unstretched Power	26.9	27.9
Accommodation	8.7	9.5

Based on the calibration of a lens immediately moved from the laser scanning apparatus to the Scheimpflug imaging setup, and separate measurements of

accommodation of an implanted lens in the artificial capsule, the Scheimpflug calibration was deemed accurate.

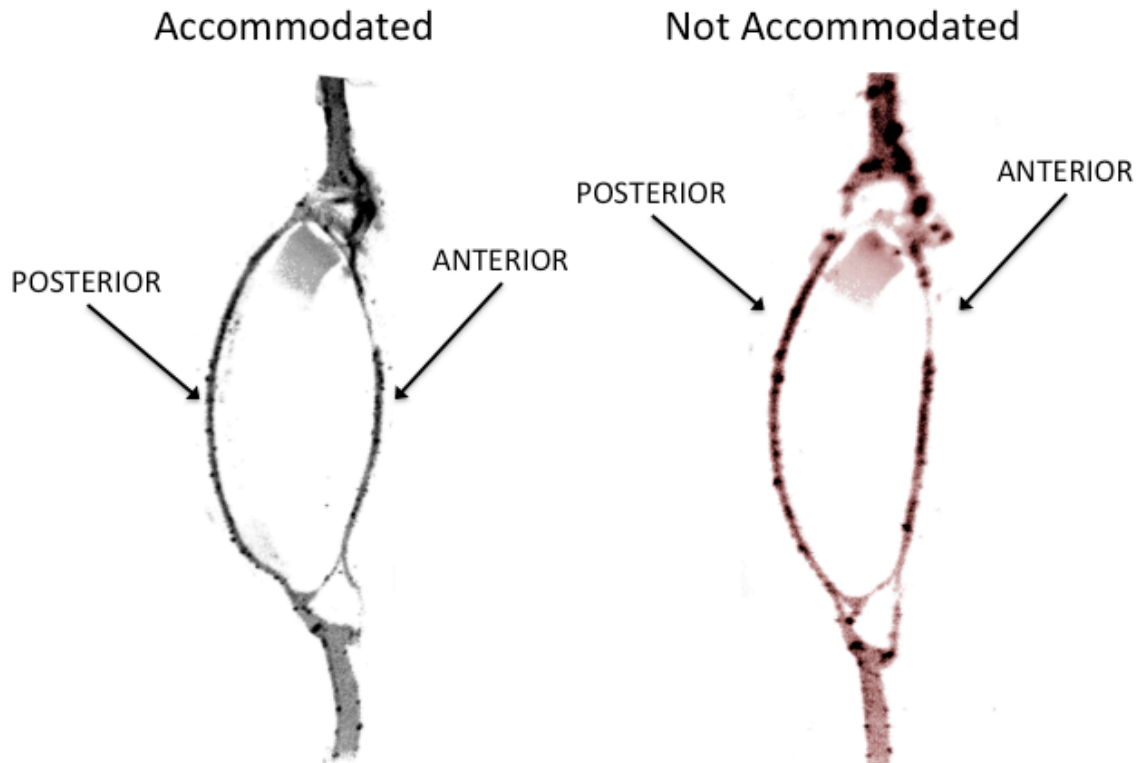


Figure 5-12. Images taken from the Scheimpflug imaging system. The lens is shown in the accommodated state (left) and not-accommodated state (right). The valve can be seen superiorly in both images.

5.5 Pressure Monitoring

A special setup was used to measure internal pressure in the lens. Two testing methodologies were used for this. Initially, a catheter pressure transducer, Millar SPR-524, was sealed inside the lens (Figure 5-13). After calibration of the sensor, pressure measurements were taken with respect to fill volume and during accommodation in an artificial capsule.

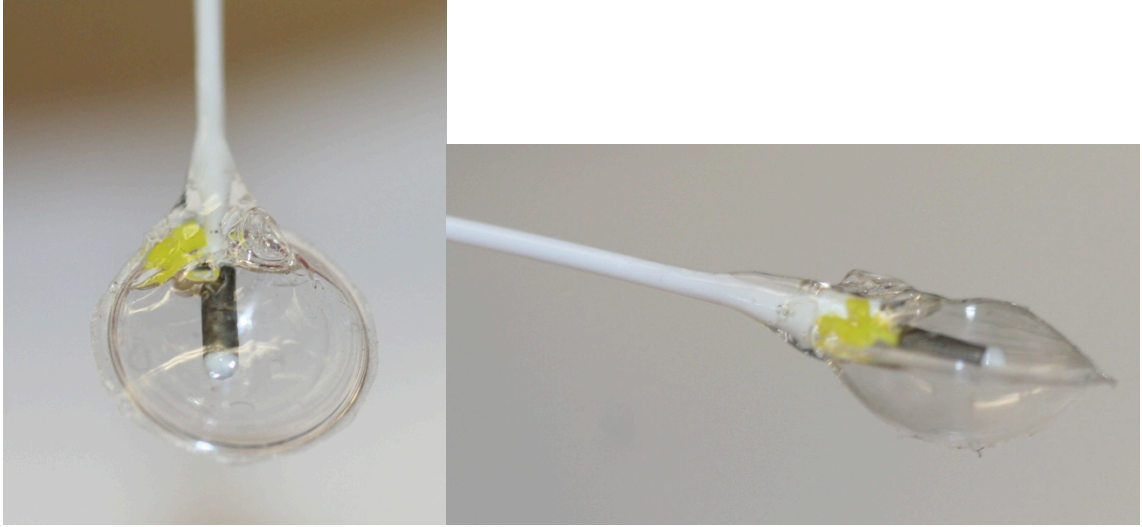


Figure 5-13. Top and side view of lens with inserted pressure transducer

To allow for more flexibility of the lens and remove the relatively rigid pressure transducer from the wall of the lens, a second design was made (Figure 5-14). A pressure transducer was located remotely from the lens, but placed in fluidic connection with the lens through a tiny tube, accessing the lens valve. The system was filled with water and no air bubbles to allow pressure signals to be transduced through the tube to the remote pressure sensor. In addition, all fluid was deemed incompressible, as there was no air in the line. This system allowed measurement of pressure while simultaneously monitoring the lens profile in the Scheimpflug imaging system.

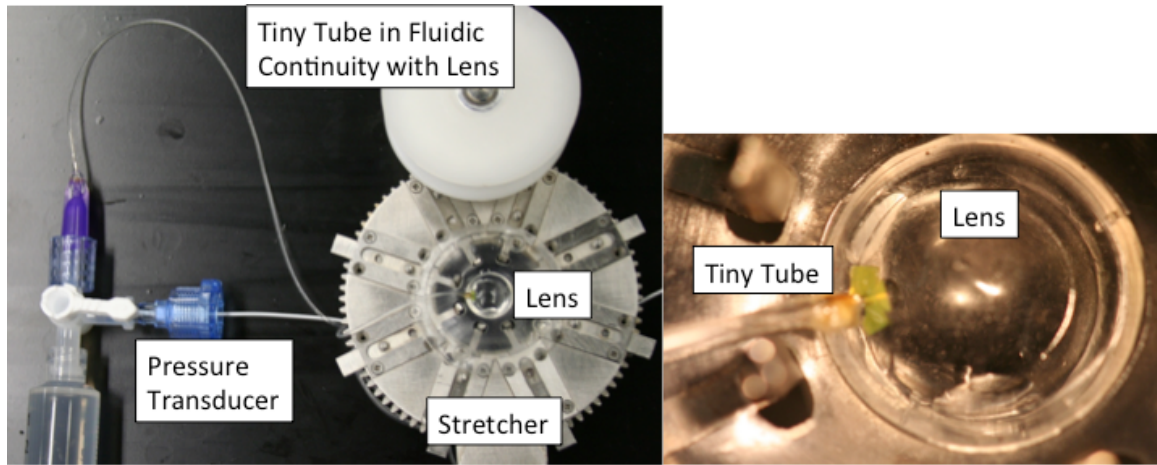


Figure 5-14. Improved method of pressure monitoring

5.6 Lens Biomechanics Data

To monitor pressure and fill volume, two experiments were performed. The first used a constant pressure source to apply an air pressure to the internal contents of the lens. The lens was cannulated through the incision port. Pressures from 0 to 41 mmHg were applied to the internal volume of the lens and the shape of the lens was visually monitored (Figure 5-15). The results from this were used to roughly determine operating pressures within the lens. In addition, the results were used to validate that sealing pressure of the MEMS-enabled refill valve were adequate.

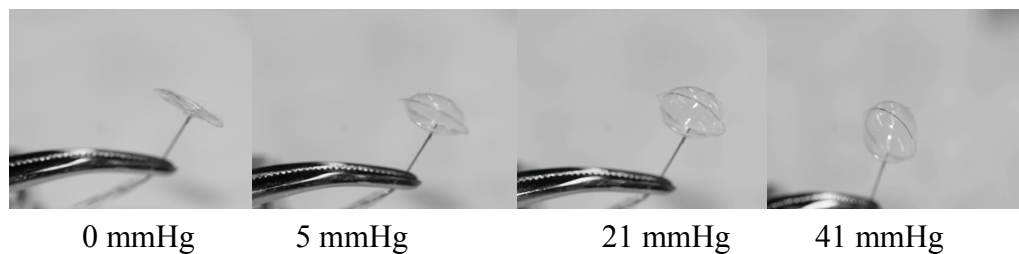


Figure 5-15. Inflation of the lens at different pressures. At maximum inflation, the lens is at an internal pressure of 41 mmHg.

To improve upon this data, pressure versus fill volume was monitored using the inserted pressure transducer (Figure 5-13). First, the lens was first evacuated. Then, water was injected into the lens through the refill valve in known increments. Pressure was monitored at each fill volume (Figure 5-16). The average slope in the linear region (90 to 140 μL) was determined to be 0.33 mmHg/ μL .

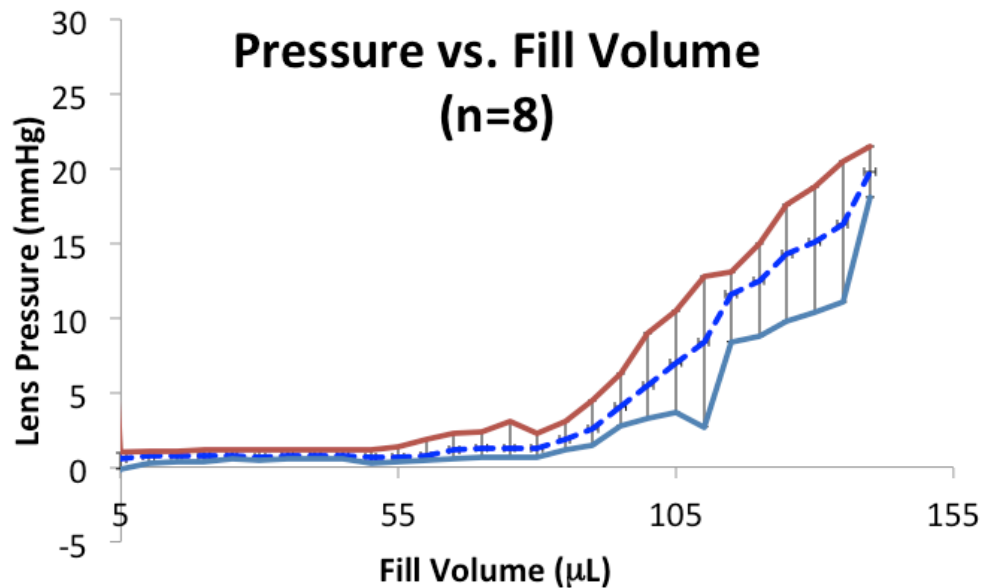


Figure 5-16. Pressure versus volume for the inserted lens transducer for 8 trials. This graph shows the maximum (red) and minimum (blue) pressures seen by the pressure transducer. The blue dotted line indicates the average pressure.

Next, pressure data from the initial implanted pressure transducer was taken with the lens implanted in the artificial capsule in non-stretched condition (stretch = 0 mm) and then sequentially stretched to a maximum value. Data is shown in Figure 5-17.

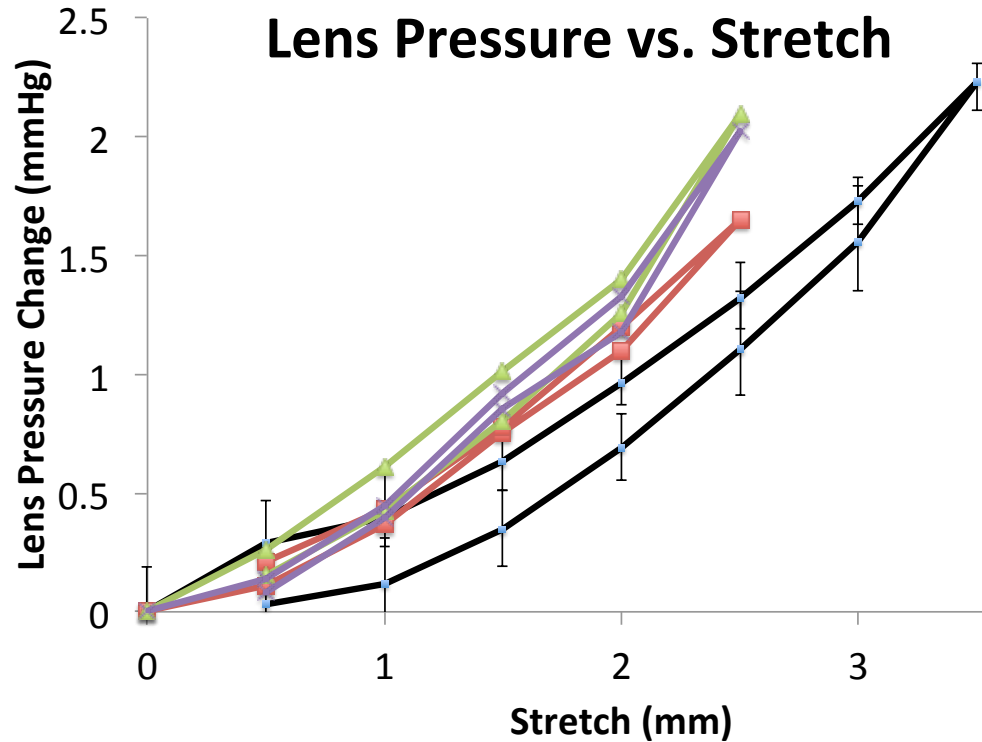


Figure 5-17. Lens pressure change during accommodation

Pressure change was between 1.7 and 2.3 mmHg at full stretch minus initial stretch. Also, as noted in the Figure 5-17, some hysteresis was seen when the lens was stretched and then unstretched. This may be due to mechanical hysteresis in the stretching apparatus itself, which was not accounted for in these experiments.

To improve upon these results, a remote pressure sensor was used as shown in Figure 5-14. Data with this setup was used with the artificial capsule and Scheimpflug imaging system to measure geometric changes in the lens with pressure simultaneously. Because the pressure transducer was remote to the lens itself, there was minimal interference between the pressure transducer and the lens itself during stretching.

The lens was placed in the relaxed position and pressure and geometric data were measured. Then, the lens was stretched and data was collected again. A total of 10 trials

were completed with the same lens and artificial capsule during measurement. Data is shown in Table 5-3.

Table 5-3. Lens dimensions, optical properties, and pressure during stretching in artificial capsule. Data reported as average \pm one standard deviation (n=10).

Geometric Properties			
	Not Stretched	Stretched	Not Stretched – Stretched
Anterior Radius of Curvature (mm)	4.4 \pm 0.1	6.0 \pm 0.4	-1.6
Posterior Radius of Curvature (mm)	4.8 \pm 0.1	6.4 \pm 0.2	-1.6
Thickness (mm)	4.5 \pm 0.1	4.1 \pm 0.1	0.4
Optical Properties			
	Not Stretched	Stretched	Accommodation (Not Stretched – Stretched)
Anterior Surface Power (D)	15.8 \pm 0.4	11.5 \pm 0.8	4.3
Posterior Surface Power (D)	14.3 \pm 0.3	10.8 \pm 0.3	3.5
Lens Power (D)	30.1 \pm 0.3	22.3 \pm 0.8	7.8
Pressure Differential (mmHg)			
Stretched Pressure – Not Stretched Pressure			
4.2 \pm 0.5			

From Table 5-3 we can see that the lens accommodates in the expected manner. As the lens is stretched, the anterior and posterior radii of curvature increase and reduce the optical power of the surface. This is similar to the natural accommodation mechanism, where the lens takes a relaxed / not stretched form with a higher optical power (and smaller radii of curvature). When the lens is stretched by the zonules and lens capsule, the radii of curvature increases and optical power decreases. For the natural lens, both anterior and posterior surfaces contribute to accommodation in a similar manner to the mechanism seen with this lens. Thickness of the lens decreases in a manner similar to

what is seen in the natural lens. For example, 4.2 mm change in thickness of this lens is similar to the 0.34 mm change for a 6 diopter from a 29-year-old female subject seen by Dubbelman (values interpolated from graph) [13] and the 0.31 mm change for a 6 diopter stimulus with 29-year-old subject seen by Brown [85].

Table 5-3 further shows that the anterior surface of the lens contributes more to the accommodation than the posterior surface (4.3D for the anterior surface versus 3.5D for the posterior surface). This is also seen with the natural human lens.

The ability to monitor pressure differential gives data not directly measured from a natural lens. Measured values of 4.2 mmHg are similar to previous measurements from the implanted pressure transducer. Discrepancies between the two measurements are most likely due to the effect of the rigid catheter pressure transducer interfering with the lens / artificial capsule during stretching.

In summary, Scheimpflug data demonstrates that the lens accommodates in a manner similar to the natural lens. Both anterior and posterior radii of curvature contribute to the accommodation mechanism, with the anterior surface contributing more. The thickness change in the lens is similar to thickness changes seen with the natural lens from previous studies with similar accommodation levels. This is expected as the lens is meant to work with the existing accommodation anatomy in the eye. This study also provides insight into the pressures exerted by the lens capsule by extrapolation from the artificial capsule. During accommodation, average pressure increases in the artificial lens are seen to be 4.2 mmHg. This data may be used with future studies and modeling of the natural lens to better understand the natural accommodation mechanism, which remains an object of active research.

5.7 Base Power Adjustment

The base power of the accommodating intraocular lens can be adjusted, or tuned, by adjusting volume of the intraocular lens, changing the index of refraction of the filling liquid, or using a secondary lens. Here, the effect of lens volume and fluid refractive index are evaluated relative to lens power. In Chapter 6: Lens Optimization, the base power is altered using a secondary lens.

To understand how these methods work for tuning base power, the thin lens equation for the power of the lens is described below

$$Power = \frac{1}{f} = \frac{n_{lens} - n_{media}}{n_{media}} \left[\frac{1}{R_1} - \frac{1}{R_2} \right]$$

where f is the focal length of the lens in the media, n_{media} is the refractive index of the media, n_{lens} is the refractive index of the lens, and R_1 and R_2 are the radii of curvature of the surfaces of the lens. These dimensions are also shown in Figure 5-18.

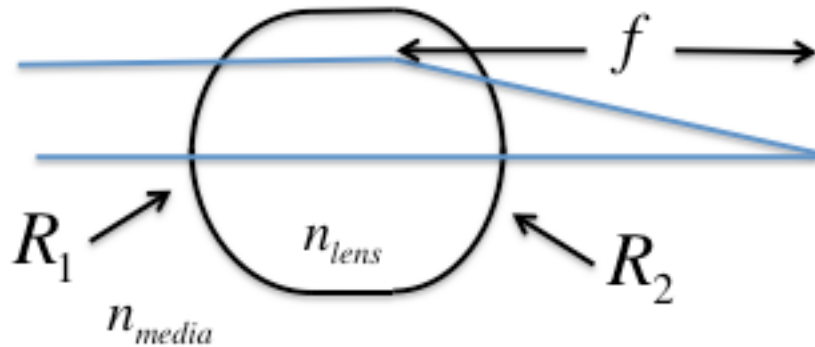


Figure 5-18 Lens diagram

From the thin lens equation, it is evident that adjusting the index of refraction will cause the base power to change. In addition, changing the inflation volume changes R_1 and R_2 and therefore the total lens power. It is important to note that the thin lens equation here is different than the lens equation described by ISO 11979-2, which does not include n_{media} on the denominator.

5.7.1 Power Adjustment with Fill Volume

To determine how fill volume effects lens power, the lens was filled while lens power was monitored. A series of four distinct fill weights were measured, between 130 to 160 μg . At each fill weight, the lens power was measured two times at each position, and the average power was computed. A plot of lens power versus fill weight from the experiment is shown in Figure 5-19.

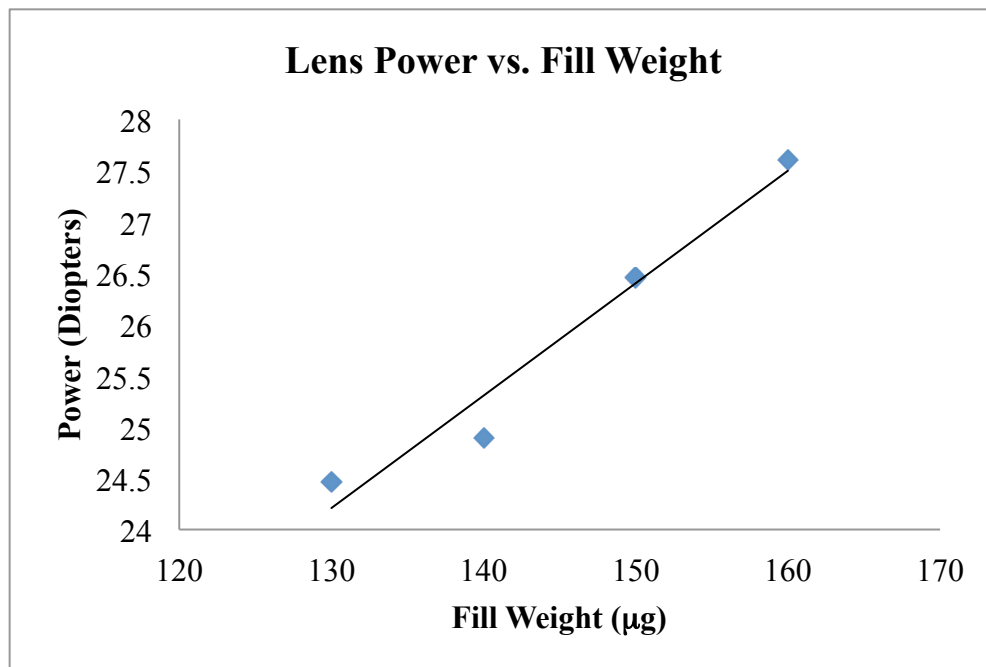


Figure 5-19. Lens power versus fill weight

The data demonstrates a linear increase in optical power with fill weight. Linear regression of the slope gave a power change of 0.11 diopters per μg of fill volume (0.11 D/ μL). Here data is presented with respect to ISO 11979-2 as described earlier.

Although this demonstrates the ability to adjust lens power by increasing or decreasing lens volume, it is ultimately limited by the lens and ocular geometry. When the lens is not entirely filled, it will no longer be taut and wrinkles may form. This causes a lower level of fill volume capability. In addition, the lens volume can only be as large as the lens capsule allows. A grossly oversized lens could cause damage to the cornea, iris, or lens capsule.

5.7.2 Power Adjustment with Refractive Index

To determine the effect of lens power relative to liquid refractive index, the base power of the lens was monitored as the index of refraction of the filling liquid was changed. To tune the optical power of the filling liquid, sugar water with various concentrations of sugar were made. Refractive index of the fluid was measured with an auto-refractor before filling the lens. After filling, the lens power was measured. Throughout these experiments the weight of the lens was maintained constant within $\pm 2 \mu\text{g}$.

Data from the experiment is shown in Figure 5-20. The trend in power versus refractive index demonstrates that the power changes from 24 D at a fluid index of 1.3836 to a power of 42 D with a fluid index of 1.4514. Some scatter in the data is seen.

This is most likely from tilt error while mounting the lens as power was measured. However, this data demonstrates that the ability to tune power based on refractive power is much larger using refractive index tuning than fill weight. In addition, this technique places little if any geometrical constraints on the lens, as it is possible to fill to the appropriate volume and then adjust based on filling fluid.

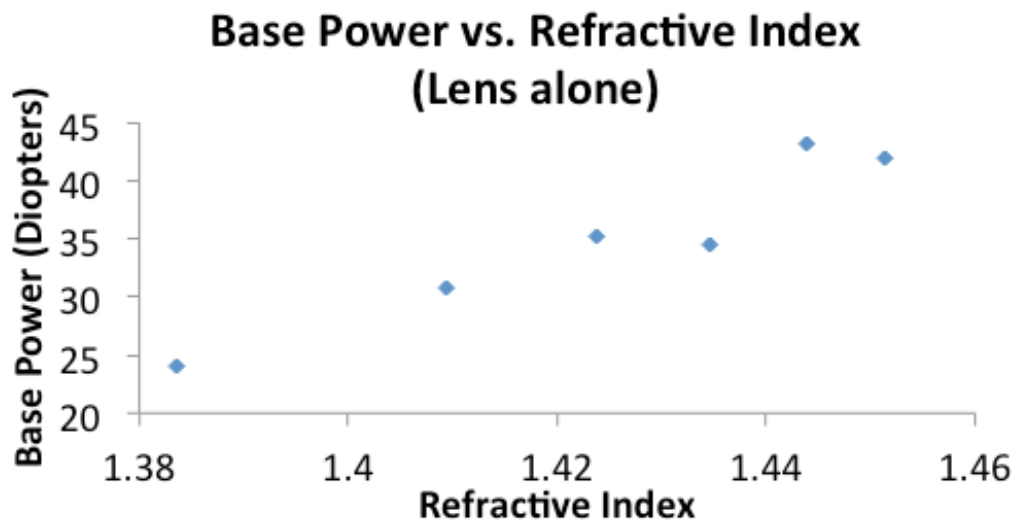


Figure 5-20. Lens power versus refractive index of filling media

5.8 Accommodation Versus Fill Volume

To understand the relationship between fill volume and accommodation, a series of six lenses were implanted into six distinct human lens capsules and fill volume versus accommodation was measured. The tissue was mounted in the stretching apparatus at a given lens fill volume. The accommodation level was measured. Then, the MEMS-enabled refill valve was accessed, additional fluid was added, and accommodation was measured again. This continued until the tissue was damaged.

To determine exact fill volume at each point, it was necessary to weigh the lens at the end of the trial and divide the fill volumes equally between the initial and final fill. This is because some fluid may have been released while accessing the MEMS-enabled refill valve multiple times. To justify this, the base power was monitored at the various fill volumes. Base power increased linearly with fill volume for all but one trial (Figure 5-21). For this outlier, it is possible that the lens was positioned in the capsule in a tilted manner. Because base power is proportional to fill volume, a linear trend indicates that fill volume is increasing in a linear manner.

Figure 5-21 shows base power versus percentage fill. The lens is assumed to be 100% full when no wrinkles or surface irregularities are seen on the lens surface. All weights on the x-axis are normalized to this weight. 100% full corresponds with 125 μL . When the one outlier is removed that did not increase power with fill volume, the average slope for base power is 0.1D per μL fill. This corresponds well with measurements implanted in the human lens capsule, which had a value of 0.1D per μL .

Percent maximum accommodation versus percent fill is plotted in Figure 5-22. Samples with poor convergence were removed from both Figure 5-21 and Figure 5-22 as their laser scans did not produce readable results. Therefore, few samples are seen in the poor convergence region of both graphs.

As the fill volume reaches 100%, an area of high accommodations is seen. This extends approximately to 120% (150 μL) fill. In this region, all samples reach maximum accommodation levels. As fill is increased further, accommodation amplitude lowers. This is believed to be due to high tension in the wall of the lens, which prevents the lens capsule from being able to deform it.

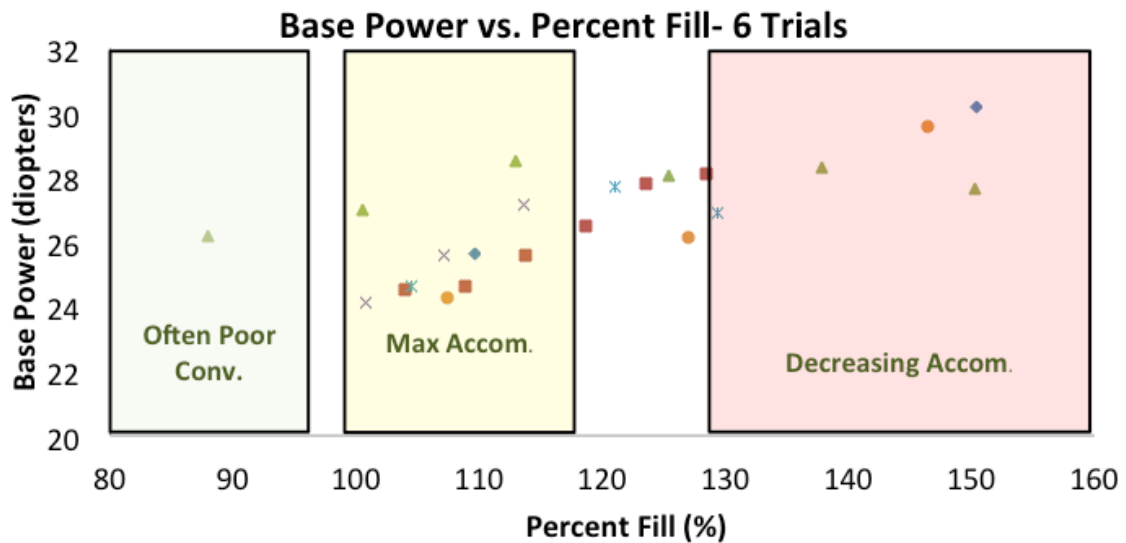


Figure 5-21. Base power versus percent fill for six implanted lenses. Three regions, based on findings from % max accommodation vs. percent fill are identified on this graph. Poor convergence is identified as an underfilled lens, and beam rays often stray in this area. Max Accom. refers to an area of maximum accommodation. Decreasing accommodation is seen at higher fill levels.

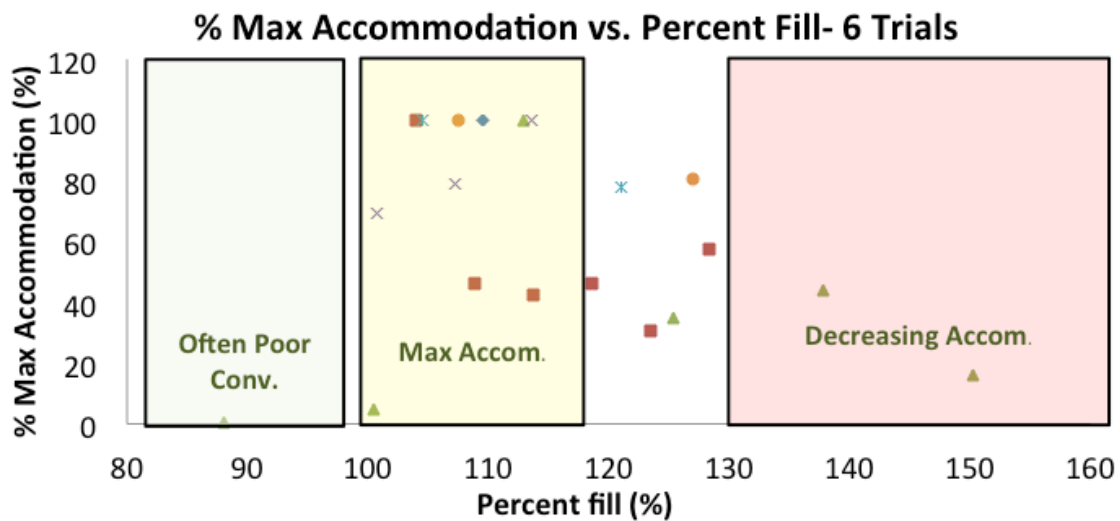


Figure 5-22. Percent of maximum accommodation versus percent fill for six implanted lenses

This data can be used to determine the amount of base power that can be adjusted on the lens while maintaining adequate accommodation. As the maximum accommodation region is approximately 25 μL (125 μL to 150 μL) and base power varies 0.1D per μL , the maximum adjustment of base power while maintaining maximum accommodation levels is 2.5 diopters.

5.9 Finite Element Modeling of Lens

A finite element analysis was completed to compare with results seen by Scheimpflug imaging. To reduce computation time an axisymmetric model was used in Comsol 4.2. The geometry of the lens was taken from Scheimpflug images in the non-stretched condition. Then, the lens was stretched by applying force to the artificial capsule in the model.

A 576 element mesh is shown Figure 5-23. The axis of symmetry lies at 0 mm. The lens and lens capsule are modeled in a stiction condition and are therefore modeled together. This boundary condition is extrapolated from the natural lens experiments where the lens does not slide relative to the lens capsule.

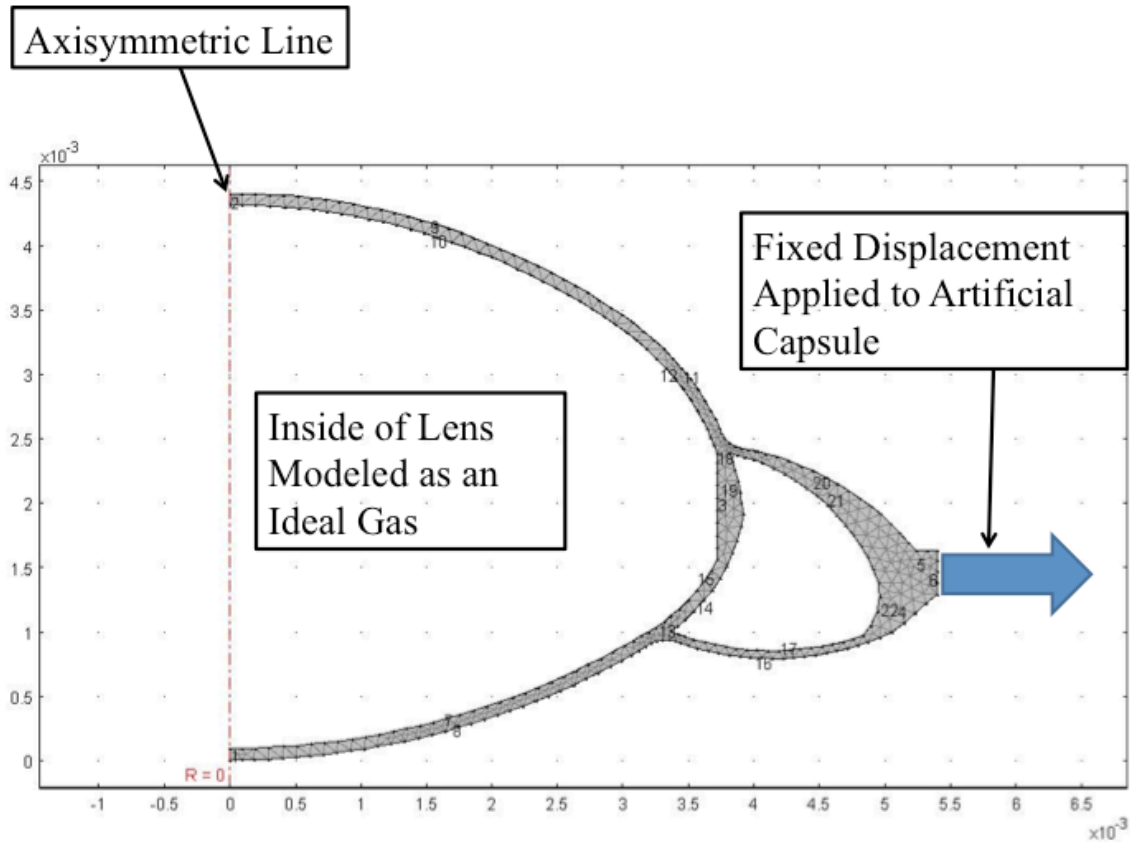


Figure 5-23. Finite element analysis mesh. Vertical and horizontal dimensions displayed as 10^{-3} m. The midpoint of the lens is held with an axisymmetric constraint. A fixed displacement is applied to the artificial capsule, as shown by the arrow. The inside of the lens is modeled as an ideal gas.

For accurate results, the FEA model has geometric nonlinearities to allow for the large deformations seen by the lens. In addition, the internal contents of the lens are not meshed. This is to improve stability of the model and reduce computation time. Large deformation for mesh elements often causes inversion of the mesh elements. In addition, even when a Poisson ratio is close to 0.5 (e.g., 0.495), internal volume of the model was found to deviate from the initial internal volume. Therefore, to solve both of these

problems, the internal volume was maintained almost constant by modeling it as a gas. The gas applies pressure to the internal wall of the model based on minute changes in volume. In response, the model equilibrates at an almost isovolumetric solution with few mesh elements.

For an ideal gas in an adiabatic state, pressure is given by

$$\frac{P}{P_o} = \left(\frac{\rho}{\rho_o} \right)^\gamma = \left(\frac{V_o}{V} \right)^\gamma$$

where P is pressure, P_o initial pressure (atmospheric pressure), ρ_o is initial density, ρ is density, V_o is initial volume, and V is volume. To find the change in pressure due to a volume deformation the prior equation can be used to find the pressure on the internal wall of the lens

$$\Delta P = P - P_o = P_o \left\{ \left(\frac{V_o}{V} \right)^\gamma - 1 \right\}$$

Although an incompressible liquid model is more appropriate than a gas model for the internal volume of the lens, modeling the internal environment as incompressible was found to prevent convergence of the solution. This is explained by the large forces the incompressible liquid plays when the model converges. Any small deviation in volume from normal deformation of the lens leads to extremely large forces. In an iterative solver, this makes the solutions unstable and therefore, prevents solutions. However, an ideal gas maintains internal volume while keeping solutions stable.

To physically find the internal volume without a mesh, a boundary integral is calculated by applying Stokes theorem.

$$Area = \oint \pi r^2 dz$$

where the boundary integral is calculated across the inner curve of the lens. The boundary conditions are shown in Figure 5-24. Note that an integral is not required at the $r=0$ position because the integrand πr^2 is equal to zero when $r=0$, and hence the line integral is equal to 0 at that point. Therefore, all integration can be taken along the internal lens wall.

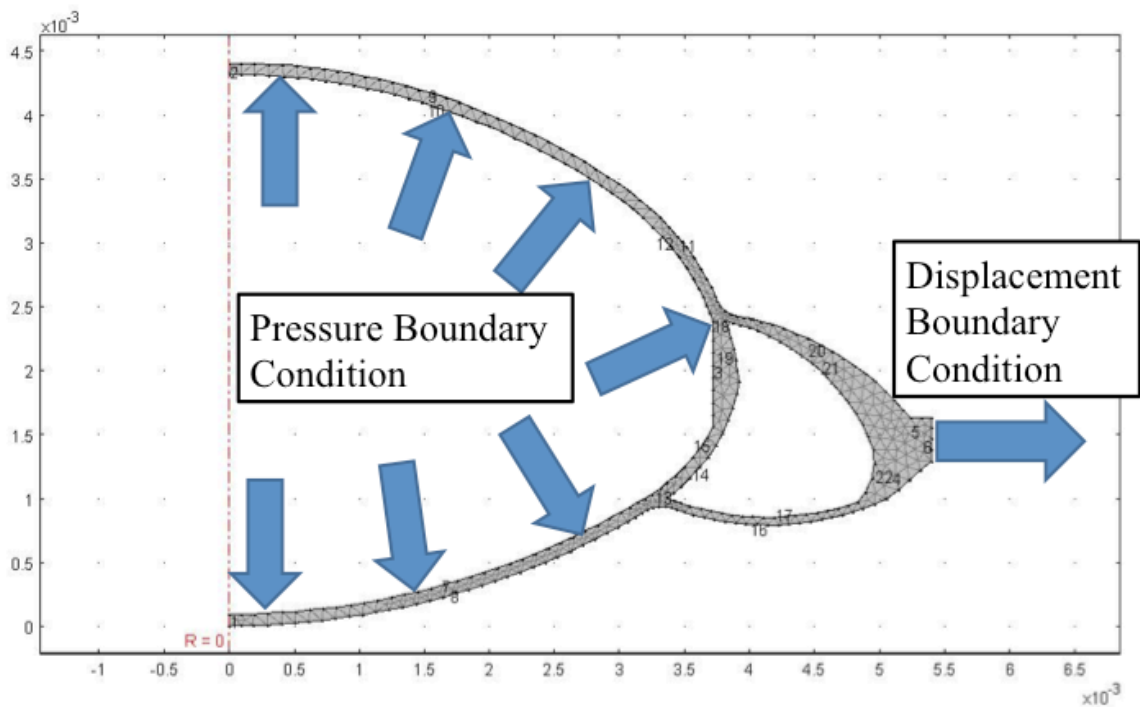


Figure 5-24. Mesh with boundary conditions. Pressure is applied based on volumetric changes of the lens volume. Lens volume is calculated with a boundary integral across the inner surface of the lens.

To calculate the power of the lens, the thick lens equation is applied to the anterior and posterior surfaces of the lens. To find curvature, a best-fit circle fit is determined across the central 4 mm of the lens using a matlab script.

Qualitative data from the finite element model and Scheimpflug images is shown in Figure 5-25. Quantitative data is presented in Table 5-4 for dimensions and pressure is presented in Table 5-5.

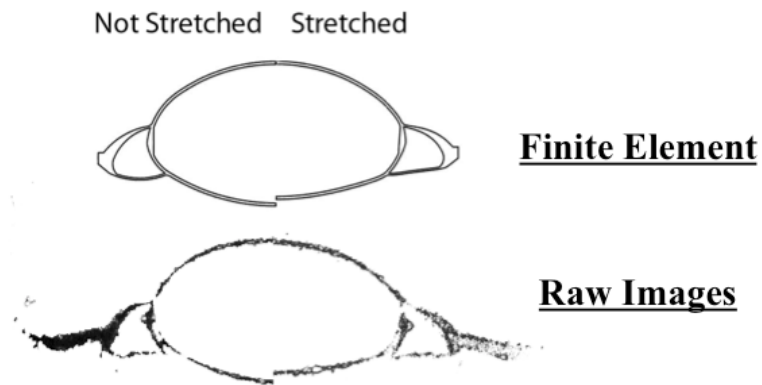


Figure 5-25. Finite element model versus raw images for non-stretched and stretched condition

Table 5-4. Comparison of Scheimpflug imaging and finite element analysis for lens stretching

	Not Stretched			Stretched		
	Anterior ROC (mm)	Posterior ROC (mm)	Thickness (mm)	Anterior ROC (mm)	Posterior ROC (mm)	Thickness (mm)
Scheimpflug	6.16	5.26	4.4	8.04	5.33	4.0
Finite Element	6.16	5.26	4.4	8.03	5.22	4.1
Error	0	0	0	0.01	0.11	0.1

Table 5-5. Pressure of lens versus finite element simulation.

	Accommodation Pressure (mmHg)
Lens Measurement	3.8
Finite Element Simulation	2.5
Error	1.3

As expected, the unstretched condition has 0 error between finite element and Scheimpflug analysis. This is because the solid model is based from the images of the

Scheimpflug analysis in the non-stretched condition. For the stretched condition, errors in the dimensions between the two models are small. The anterior radius of curvature (ROC) is within 0.01 mm, the posterior ROC within 0.11 mm, and the thickness within 0.1 mm. Pressure is similar, with a 1.3 mm deviation between the lens measurement and the finite element analysis.

Based upon these results, there was good correlation between finite element analysis simulation and actual measured values from Scheimpflug imaging. The largest discrepancy was found in a 1.3 mmHg measurement difference in internal pressure from the finite element and the lens measurement. This indicates that even pressure measurements are within the same range for the model and the actual lens. Dimensional measurements were within 0.11 mm.

5.10 Experimental Validation of Design in Porcine and Human Tissue

Lens accommodation was validated first in porcine eyes and secondly in human eyes. Human tissue is used as it ensures that physiologic forces are applied to the lens during deformation. However, with human tissue, there is more variation due to the condition of the tissue and the surgical technique. Therefore, these techniques are less repeatable than using the artificial lens capsule. Test methods for monitoring accommodation and mounting tissue are presented in Chapter 3: Measuring Accommodation.

5.10.1 Porcine Eye Validation

When implanted in porcine eyes, the power of the biomimetic accommodating intraocular lens is shown to decrease as the ciliary muscle was stretched (Figure 5-26). This is consistent with the action of the natural human lens. The lens accommodation is taken as the power with the lens not stretched minus the power of the lens while stretched at 4 mm. Two data points for accommodation were taken. The first is the initial 0 mm stretch minus the power at 4 mm stretch. The second is the power at the second 0 mm stretch minus the power at 4 mm stretch. Error bars correspond to the maximum and minimum accommodative powers recorded from this stretch.

Average lens accommodation of the implanted lenses is from 2.5 to 10.5 diopters. More variation in accommodation is seen at the higher accommodative amplitudes, which is indicated with the error bars.

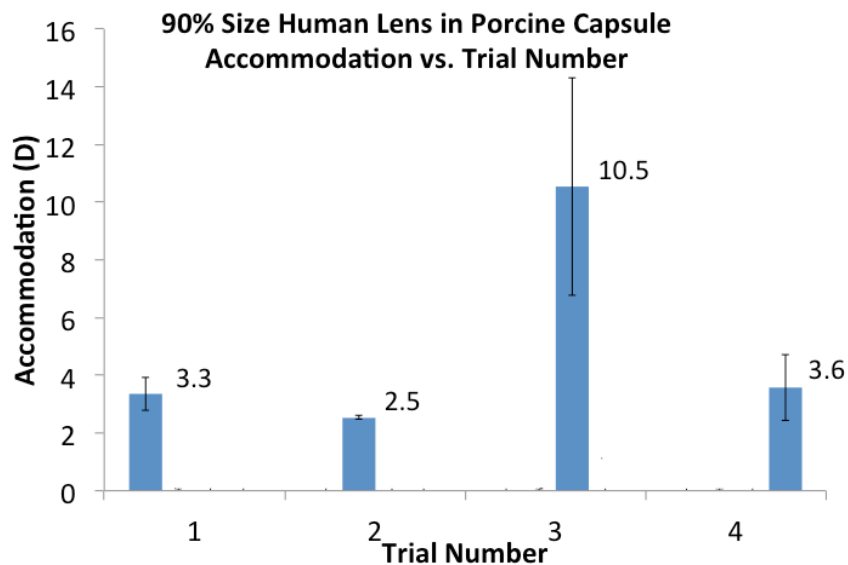


Figure 5-26. Accommodation amplitude versus trial number for four implanted lenses stretched at 4 mm diameter. Average accommodation levels of 2.5, 3.3, 3.6, and 10.5 diopters were seen in the four implanted lenses.

5.10.2 Human Eye Validation

To validate the device in human eyes, accommodation was measured as described in Chapter 3, Measuring Accommodation. Eight trials were carried out with different eyes and different implants. All results demonstrated higher than 2 diopters of accommodation. A table of results is shown in Table 5-6.

Table 5-6 Accommodation levels from 8 human lens implant trials with 5 mm ciliary muscle stretch

Test Number	Average Accommodation (D)
1	2.5
2	2.4
3	5.0
4	4.0
5	4.4
6	2.7
7	5.7
8	3.4

In addition, a series of five human lens implants were tested at a ciliary muscle stretch of 3 mm to ensure adequate accommodation, even at lower stretch levels (Table 5-7). Similar to the 5 mm stretch, all accommodation levels were over 2 diopters of accommodation.

Table 5-7 Accommodation levels from five human lens implants with five distinct lenses. Ciliary muscle stretched to 3 mm to ensure accommodation even under lower stretch levels

Test Number	Average Accommodation (D)
1	6.5
2	6.2
3	2.8
4	2.6
5	2.4

The results of these experiments demonstrate that the accommodating intraocular lens has the capability to accommodate when implanted into human tissue in an *ex vivo* stretching apparatus. As this is the best *ex vivo* setup, the next steps of accommodation testing include validating accommodation in an animal model.

This work objectively demonstrates the focusing ability of a fluid-filled biomimetic accommodating intraocular lens enabled by a MEMS refill valve in a porcine and human eye. In all cases, the focusing levels are significant for alleviation of presbyopia. The minimum and maximum accommodative amplitudes correspond to the focusing ability of 49 and 18-year-old lenses, respectively, from the porcine lens implants [17]. For the human lens implants focusing ability corresponded to a maximum age of 49- and minimum age of 33-year-old lenses.

Variability in the data is most likely due to discrepancy in age and condition of eyes, surgical implantation procedure, and lens-to-lens variation. However, by objectively demonstrating accommodation ability, this work validates the feasibility of a biomimetic accommodating intraocular lens enabled by a MEMS refill valve.

5.11 Conclusion

To understand the mechanism of action of the biomimetic intraocular lens, first the relationship between the lens capsule and the natural lens were examined. When a capsulotomy was placed centralized and the natural lens was allowed to slip across the capsulotomy, reverse accommodation was observed. Therefore, based upon this knowledge, a slightly decentered capsulotomy was used with the biomimetic accommodating intraocular lens.

Next, a Scheimpflug imaging system, pressure monitoring system, and artificial lens capsule were designed and made to allow precise measurements of the lens during accommodation. These values were used to determine that the accommodating IOL acts in a similar manner to the natural human lens. Similarities include both sides of the lens contributing to accommodation with more curvature change on the anterior, similar changes in thickness between the IOL and the natural lens, and accommodation in a manner consistent with the natural lens. Pressure data during accommodation gives a glimpse into how the natural lens works.

Methods to accurately tune base power were demonstrated by adjusting fill volume and refractive index of the filling liquid. Then the effect of fill volume on base power and accommodation levels was determined. Base power was seen to increase in a linear manner with fill volume. In addition, three regions of lens performance were found, one corresponding to poor optical quality and under-filling the lens, a maximum region of accommodation, and reduced accommodation. These levels limit the amount of base power adjustment on the current lens while maintaining accommodation.

A finite element model of the lens was made based upon a shell mesh of the lens. The internal environment of the lens was modeled as an ideal gas and pressure associated with any volumetric changes was applied along the inside of the lens. Results from this correlated well with images captured on the Scheimpflug imaging system.

Finally, validation of the accommodating intraocular lens was completed in an *ex vivo* stretching apparatus in both porcine and human eyes.

Based upon these results, this lens has the potential to be used after a natural clouded lens is removed in cataract surgery. Unlike currently FDA approved lenses, this lens has the potential to restore youthful accommodation levels with the capability of adjustable base power for high acuity vision.

6 LENS OPTIMIZATION

6.1 Introduction

This chapter describes how knowledge of lens function can be used to optimize lens design. A thin lens formula is presented and analyzed for lens power change due to a shape changing IOL. Based on the equation, a high index of refraction lens is presented as a method to achieve higher accommodation levels. In addition to high accommodation levels, base power is also increased for this high index of refraction lens. Therefore, a second dual lens is proposed. The dual lens has a diverging lens located inside the accommodating intraocular lens. The diverging lens is used to reduce base power of the lens, while the high index of refraction lens is used to provide high accommodation levels. In this way, both high accommodation and accurate base power can be achieved. In addition, the internal IOL can be customized for different refractive outcomes. Therefore, by changing the internal IOL, the base power of the lens can be modified while maintaining the same lens geometry and same filling fluid.

6.2 High-Index Lens

Prior chapters discussed the deformation of the lens in the lens capsule during accommodation. Based on a given shape change of the lens, accommodation can be changed by altering the refractive index of the lens itself. As described in Chapter 5, for a thin lens the lensmaker's formula is

$$Power = \frac{1}{f} = \frac{n_{lens} - n_{media}}{n_{media}} \left[\frac{1}{R_1} - \frac{1}{R_2} \right]$$

Therefore, for a shape changing lens, change in accommodative power (Accom) can be approximated relative to the change in surface curvatures of the lens.

$$Accom = \frac{n_{lens} - n_{media}}{n_{media}} \left[\frac{1}{\Delta R_1} - \frac{1}{\Delta R_2} \right]$$

If we take shape change as a constant, then by using a higher-index lens, the accommodation can be increased. Data collected from two lenses, one with a refractive index of 1.4 and one with a refractive index of 1.47 is shown in Table 6-1.

Table 6-1. Accommodation power for lenses with two different refractive indices

Artificial Capsule: Accommodation Levels	
n=1.4 fluid (one trial)	n=1.47 fluid (three trials)
8.7 diopters	22.8 diopters

Because n_{media} is 1.336, $n_{lens} - n_{media}$ is equal to 0.064 for the n=1.4 fluid, while it is equal to 0.134 for the n=1.47 fluid. Therefore, $n_{lens} - n_{media}$ is 2.1 times larger for the

$n=1.46$ fluid. From the accommodation power equation, accommodation is estimated to be approximately 2.1 times larger with this lens. The actual accommodation value for the $n=1.47$ fluid is 2.6 times larger. The difference between theoretical and measured values is likely from differences between the two lenses, two artificial lens capsules, and variation in the stretching between the two setups. However, a large increase in accommodation, close to 2.1 times higher, is seen when higher-index lenses are used, which corresponds to theory.

By using a high-index lens alone high accommodation amplitudes can be realized, but this is at the expense of a high base power. From the thin lens equation, it can be seen that the base power is also 2.1 times larger. Therefore, to utilize this concept for accommodation, there must be a method to reduce overall lens power.

6.3 Base-Power-Corrected High-Index Lens

To reduce base power of the lens and still maintain high accommodation levels, a dual lens system was designed. The outer lens was designed identically to the current biomimetic accommodating IOL. The internal lens was designed as a diverging lens to lower overall lens power.

A cross section schematic of the lens is shown in Figure 6-1. A diverging lens is placed inside the biomimetic accommodating IOL by attaching it to the equator of the lens. As in the previous designs, fluid is injected into the lens with a MEMS-enabled refill valve. To provide fluidic continuity between the anterior and posterior halves of the lens, a series of pass-through holes are made.

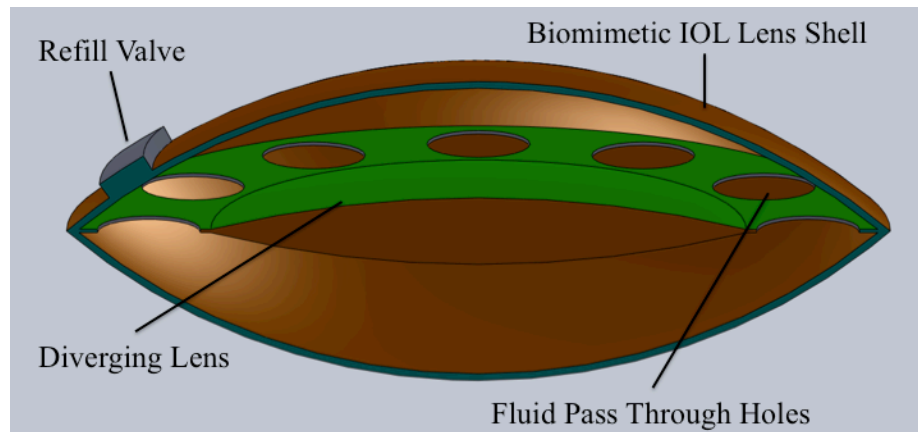


Figure 6-1. Cross section of a dual lens. The biomimetic accommodating IOL shell encases a diverging lens, which is attached to the lens along the equator. A refill valve allows fluid to flow into the anterior portion of the lens. Fluid pass-through holes allow fluid to go from one side of the lens to the other side.

A side view of a dual lens is shown with corresponding indices of refraction in Figure 6-2. The outer portion of the lens with the converging anterior and posterior surfaces corresponds to the shape of the biomimetic accommodating IOL. Change in shape of these surfaces provides a high level of accommodation due to the high index of refraction of the lens. To correct for base power, a lens inside the accommodating IOL acts as a negative power, or diverging lens. Although the internal lens has convex surfaces, the overall power is negative because it has a lower index of refraction ($n=1.4$) than the surrounding liquid ($n=1.47$).

A simplified ray diagram of the dual lens is shown in Figure 6-3. Parallel rays enter from the left and are converged by the anterior surface of the lens. The diverging lens acts to expand the rays, reducing power of the lens. As the rays pass across the posterior surface of the lens they are converged by the power of the posterior surface of the lens.

A Scheimpflug image of the lens in stretched and not stretched condition is captured in Figure 6-4. Using the index of refraction of the filling fluid and the anterior and posterior curvatures of the lens, the theoretical power of the lens without the diverging lens is calculated. Next, the total lens power with the diverging lens inserted was measured using the scanning laser. The calculated negative power of the diverging lens was calculated from these two values in Table 6-2.

From Table 6-2, high accommodation levels are seen. Before the diverging lens is accounted for, the stretched power is 27.5 D, while after the diverging lens is accounted for, the base power is 16.0 D. Therefore, the diverging lens accounts for -11.5 diopters of power when the lens is in the stretched position. Likewise, the unstretched power is lowered from 48.2 D to 37.8 D because of the diverging lens.

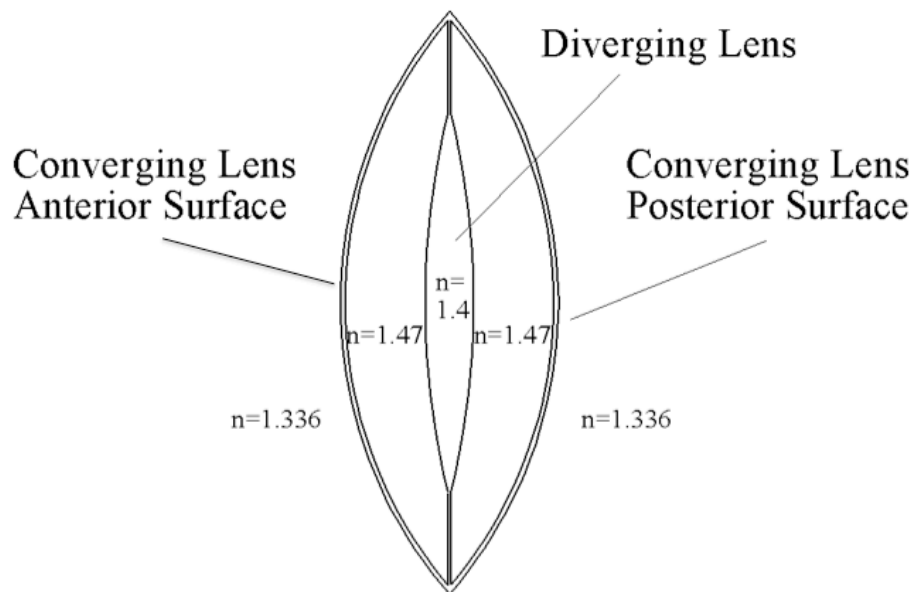


Figure 6-2. Two part lens. The anterior and posterior converging lens surfaces are used to change optical power during accommodation. To lower base power, a diverging lens is located in the center of the liquid-filled lens.

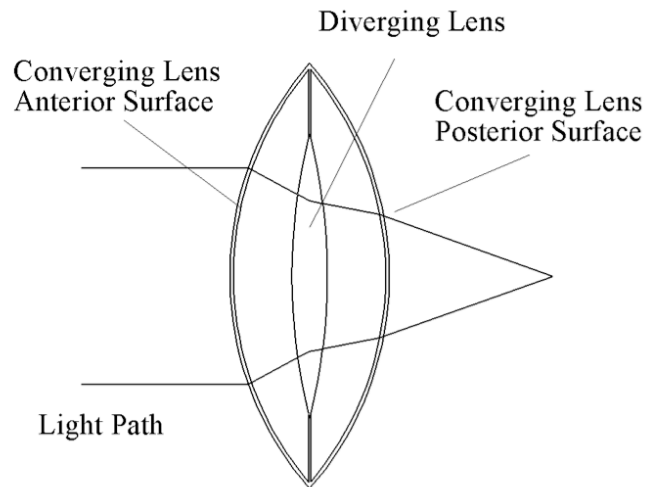


Figure 6-3. Simplified ray trace through dual lens. The converging lens anterior surface acts to converge the light path. The diverging lens expands the beam. The converging lens posterior surface finishes focusing the light.

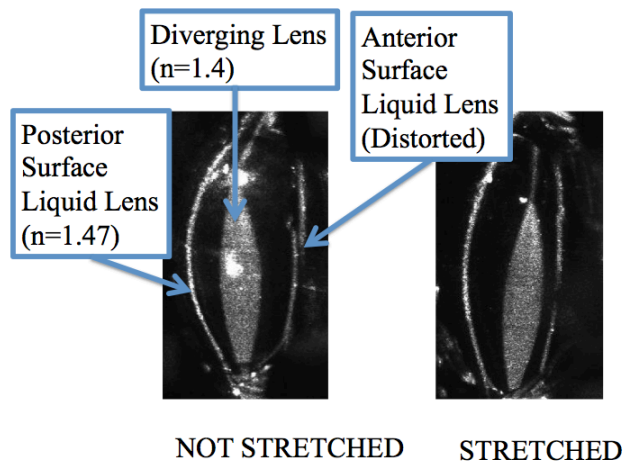


Figure 6-4. Scheimpflug image of dual lens in the not-stretched and stretched condition. The anterior surfaces are distorted from the Scheimpflug imaging system because the dual lens is not index matched with the surrounding water bath. To compensate, images are taken from both the anterior and posterior sides of the lens.

Table 6-2. Dual lens power as assessed by laser scan and theoretical power without the internal diverging lens. Based on these two values, the diverging power of the lens is determined.

	Stretched	Not-Stretched	Accommodation
Total Lens Power by Laser Scan (D)	16.0	37.8	21.8
Theoretical Power without the Internal Diverging Lens (D)	27.5	48.2	21.9

6.4 Conclusion

A refined lens design was prototyped and tested based on prior lens measurements. This used a high index of refraction to provide high accommodation levels. However, to adjust base power appropriately, a second, internal lens was made. The overall system was considered a dual lens system. The internal diverging lens was seen to reduce base power and provide clinically relevant base powers. The outer shell with high index of refraction provided high accommodation levels.

7 CONCLUSION

This work presents a possible solution for presbyopia. A medical device has been proposed based upon clinical knowledge of the anatomy and physiology of the lens, the medical course of presbyopia, and the surgical procedure for lens replacement. The fundamental requirements of the device include: the ability to focus using the natural neural circuitry and anatomy of the eye, intraoperative and post-operative refractive adjustment, minimal surgical incisions to prevent postoperative astigmatism and reduce recovery time, long-term biocompatibility, and high visual acuity.

Based upon these requirements, an inflatable intraocular lens is proposed that mimics the youthful human lens. Materials for the device were selected for biocompatibility and reliability. Processing of the materials was characterized in terms of viscoelastic properties. Processing was optimized for repeatable results.

To validate the design, a method to test accommodating intraocular lenses was developed. This testing methodology relied on human tissue to maintain forces and anatomy similar to the forces observed from a live implantation. This test setup was used to demonstrate repeatable accommodation ability of the lens.

To fully explain the biomechanics of the lens, the lens was imaged during simulated accommodation experiments. Lens measurements were compared with biometric measurements of the natural lens. This demonstrated that the lens acts in a manner similar to the youthful crystalline lens.

Based upon knowledge of the lens mechanics, improvements to the lens were made to increase accommodative amplitudes. Prototypes of these devices were built and efficacy was determined from testing.

APPENDIX A: Biological Testing Data, MED4-4210



Biological Testing Data MED4-4210

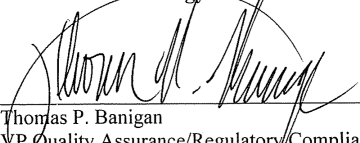
Test	Standard/ Method	Test Results
Cytotoxicity Study Using The ISO Elution Method (1X MEM Extract)	ISO 10993-5 USP <87>	A-Noncytotoxic B-Noncytotoxic C-Noncytotoxic
<i>In Vitro</i> Hemolysis Study (Modified ASTM -Extraction Method)	ISO 10993-4	A-Nonhemolytic
USP and ISO Systemic Toxicity Study Extract*	ISO 10993-11 USP <88>	A-Nontoxic
ISO Intracutaneous Study Extract*	ISO 10993-10 USP <88>	A-Nonirritant
ISO Muscle Implantation Study 1 Week*	ISO 10993-6 USP <88>	A-Nonirritant
ISO Muscle Implantation Study 12 Week	ISO 10993-6 USP <88>	A-Nonirritant
Genotoxicity: Bacterial Reverse Mutation Study (DMSO and Saline Extracts)	ISO 10993-3	A-Nonmutagenic
USP Pyrogen Study Material Mediated	ISO 10993-11 USP <151>	A-Nonpyrogenic
ISO Maximization Sensitization Study Extract	ISO 10993-10	A-Nonsensitization
Mammalian Mutagenesis Schultz, "Scientific Justification For The Deletion Of Certain Biological Test From The Testing Scheme Proposed In The FDA's 'Guidance for Manufacturers Of Silicone Devices Affected By The Withdrawal Of Dow Corning Silastic Materials.' "	-----	-----
Cytogenic Damage Schultz, "Scientific Justification For The Deletion Of Certain Biological Test From The Testing Scheme Proposed In The FDA's 'Guidance for Manufacturers Of Silicone Devices Affected By The Withdrawal Of Dow Corning Silastic Materials.' "	-----	-----

* Product meets USP Class VI test requirements.

Test Article Conditioning

Sample	Condition
A	Per NuSil Technology Product Specification
B	Condition A + Hot Air Oven 12 Hours @ 200°C
C	Condition A + Autoclave 2 Hours @ 15 psi

This test article has been tested and found compliant with the above requirements. Please contact the NuSil Technology LLC Healthcare Director if you require additional information.


 Thomas P. Banigan
 VP Quality Assurance/Regulatory Compliance

APPENDIX B: Index of Silicone Elastomer Testing, MED4-4210

INDEX OF SILICONE ELASTOMER TESTING MED4-4210

I.) BULK MATERIAL PROPERTIES

SEC.	PROPERTY	TEST METHOD	EXHIBIT
1	Chemical Structure & Composition	ASTM F-604	EXHIBIT 1
2	Appearance: (Color, Translucency/Transparency)	TM-002	EXHIBIT 2
3	Particulate Contamination:	TM-060	EXHIBIT 3
4	Molecular Weight of Uncrosslinked Polymer (GPC) Degree of Polymerization of Base Polymer	TM-098	EXHIBIT 4
5	Trace Metals Analysis (X-ray Spectroscopy)	ASTM F-1372 E-2 SM11-22	EXHIBIT 5
6	Viscosity	NT TM- 001	EXHIBIT 6

II.) PHYSICAL PROPERTIES (Cured)

SEC.	PROPERTY	No Conditioning	Hot Air Oven*	Autoclaved*	Test Method
7	Durometer, Hardness Shore A	EXHIBIT 7	EXHIBIT 8	EXHIBIT 9	NT TM-006
8	Silica Distribution Within the Polymer	EXHIBIT 10	/	/	EDS
9	Tensile Strength,	EXHIBIT 11	EXHIBIT 12	EXHIBIT 13	NT TM-007
10	Elongation, %	EXHIBIT 14	EXHIBIT 15	EXHIBIT 16	NT TM-007
11	Energy at Rupture (Strain Energy at Rupture)	EXHIBIT 17	EXHIBIT 18	EXHIBIT 19	NT TR-011
12	Tear Strength	EXHIBIT 20	EXHIBIT 21	EXHIBIT 22	NT TM-009
13	Modulus @ 200%	EXHIBIT 23	EXHIBIT 24	EXHIBIT 25	NT TM-007
14	Compression Set, %	EXHIBIT 26	EXHIBIT 27	EXHIBIT 28	NT TM-065
15	Tensile Set, @ 100% Elongation	EXHIBIT 29	EXHIBIT 30	EXHIBIT 31	NT TM-066
16	Cross-link Density, Solvent Swell (Xylene)	EXHIBIT 32	EXHIBIT 33	EXHIBIT 34	NT TM-038
17	Specific Gravity	EXHIBIT 35	EXHIBIT 36	EXHIBIT 37	NT TM-003
18	Volatiles, %	EXHIBIT 38	/	/	NT TM-004

* Accelerated Conditions : 1.) Hot Air Oven = 12 hours @ 200°C 2.) Autoclave = 15 psi. for 2 hours.

References

- [1] R. Menapace, O. Findl, K. Kriechbaum, and C. Leydolt-Koepl, "Accommodating intraocular lenses: a critical review of present and future concepts," *Graefes Arch Clin Exp Ophthalmol*, vol. 245, pp. 473-89, Apr 2007.
- [2] J. F. Alfonso, L. Fernandez-Vega, M. B. Baamonde, and R. Montes-Mico, "Prospective visual evaluation of apodized diffractive intraocular lenses," *J Cataract Refract Surg*, vol. 33, pp. 1235-43, Jul 2007.
- [3] E. A. Hermans, T. T. Terwee, S. A. Koopmans, M. Dubbelman, R. G. van der Heijde, and R. M. Heethaar, "Development of a ciliary muscle-driven accommodating intraocular lens," *J Cataract Refract Surg*, vol. 34, pp. 2133-8, Dec 2008.
- [4] J. Ben-Nun and J. L. Alio, "Feasibility and development of a high-power real accommodating intraocular lens," *J Cataract Refract Surg*, vol. 31, pp. 1802-8, Sep 2005.
- [5] J. S. Wolffsohn, S. A. Naroo, N. K. Motwani, S. Shah, O. A. Hunt, S. Mantry, M. Sira, I. A. Cunliffe, and M. T. Benson, "Subjective and objective performance of the Lenstec KH-3500 "accommodative" intraocular lens," *Br J Ophthalmol*, vol. 90, pp. 693-6, Jun 2006.
- [6] G. Zhao, J. Zhang, Y. Zhou, L. Hu, C. Che, and N. Jiang, "Visual function after monocular implantation of apodized diffractive multifocal or single-piece monofocal intraocular lens Randomized prospective comparison," *J Cataract Refract Surg*, vol. 36, pp. 282-5, Feb 2010.
- [7] S. Cillino, A. Casuccio, F. Di Pace, R. Morreale, F. Pillitteri, G. Cillino, and G. Lodato, "One-year outcomes with new-generation multifocal intraocular lenses," *Ophthalmology*, vol. 115, pp. 1508-16, Sep 2008.
- [8] A. Glasser, "Restoration of accommodation: surgical options for correction of presbyopia," *Clin Exp Optom*, vol. 91, pp. 279-95, May 2008.
- [9] D. Atchison, Smith, G., *Optics of the Human Eye*. Oxford: Butterworth-Heinmann, 2000.
- [10] D. A. Atchison and G. Smith, "Continuous gradient index and shell models of the human lens," *Vision Res*, vol. 35, pp. 2529-38, Sep 1995.

- [11] K. Park. (2011, May 16). *Chapter 160: Anatomy of the Uvea*. Available: <http://medtextfree.wordpress.com/2011/01/21/chapter-160-anatomy-of-the-uvea/>
- [12] H. von Helmholtz, *Helmholtz's Treatise on Physiological Optics*: Optical Society of America, 1924.
- [13] M. Dubbelman, G. L. Van der Heijde, and H. A. Weeber, "Change in shape of the aging human crystalline lens with accommodation," *Vision Res*, vol. 45, pp. 117-32, Jan 2005.
- [14] P. Rosales, M. Dubbelman, S. Marcos, and R. van der Heijde, "Crystalline lens radii of curvature from Purkinje and Scheimpflug imaging," *J Vis*, vol. 6, pp. 1057-67, 2006.
- [15] A. Duane, "Normal values of the accommodation at all ages," *Journal of the American Medical Association*, vol. 59, pp. 1010-1013, 1912.
- [16] J. F. Koretz, P. L. Kaufman, M. W. Neider, and P. A. Goeckner, "Accommodation and presbyopia in the human eye--aging of the anterior segment," *Vision Res*, vol. 29, pp. 1685-92, 1989.
- [17] A. Glasser and M. C. Campbell, "Presbyopia and the optical changes in the human crystalline lens with age," *Vision Res*, vol. 38, pp. 209-29, Jan 1998.
- [18] K. R. Heys, S. L. Cram, and R. J. Truscott, "Massive increase in the stiffness of the human lens nucleus with age: the basis for presbyopia?," *Mol Vis*, vol. 10, pp. 956-63, Dec 16 2004.
- [19] H. Pau and J. Kranz, "The increasing sclerosis of the human lens with age and its relevance to accommodation and presbyopia," *Graefes Arch Clin Exp Ophthalmol*, vol. 229, pp. 294-6, 1991.
- [20] H. A. Weeber, G. Eckert, W. Pechhold, and R. G. van der Heijde, "Stiffness gradient in the crystalline lens," *Graefes Arch Clin Exp Ophthalmol*, vol. 245, pp. 1357-66, Sep 2007.
- [21] F. Manns, J. M. Parel, D. Denham, C. Billotte, N. Ziebarth, D. Borja, V. Fernandez, M. Aly, E. Arrieta, A. Ho, and B. Holden, "Optomechanical response of human and monkey lenses in a lens stretcher," *Investigative Ophthalmology & Visual Science*, vol. 48, pp. 3260-3268, Jul 2007.
- [22] K. R. Heys, S. L. Cram, and R. J. W. Truscott, "Massive increase in the stiffness of the human lens nucleus with age: the basis for presbyopia?," *Mol Vis*, vol. 10, pp. 956-963, Dec 16 2004.
- [23] H. A. Weeber, G. Eckert, W. Pechhold, and R. G. L. van der Heijde, "Stiffness gradient in the crystalline lens," *Graefes Archive for Clinical and Experimental Ophthalmology*, vol. 245, pp. 1357-1366, Sep 2007.

- [24] H. Y. S. Scarcelli G., "Age-related Stiffening Of Human Lens Is The Result Of A Variation In Spatial Distribution Of Lens Elastic Modulus," presented at the Association for Research in Vision and Ophthalmology, Fort Lauderdale, 2012.
- [25] C. A. Cook, J. F. Koretz, A. Pfahnl, J. Hyun, and P. L. Kaufman, "Aging of the human crystalline lens and anterior segment," *Vision Res*, vol. 34, pp. 2945-54, Nov 1994.
- [26] J. F. Koretz, C. A. Cook, and P. L. Kaufman, "Aging of the human lens: changes in lens shape at zero-diopter accommodation," *J Opt Soc Am A Opt Image Sci Vis*, vol. 18, pp. 265-72, Feb 2001.
- [27] N. Brown, "The change in lens curvature with age," *Exp Eye Res*, vol. 19, pp. 175-83, Aug 1974.
- [28] J. F. Koretz and G. H. Handelman, "How the human eye focuses," *Sci Am*, vol. 259, pp. 92-9, Jul 1988.
- [29] H. J. Burd, S. J. Judge, and J. A. Cross, "Numerical modelling of the accommodating lens," *Vision Res*, vol. 42, pp. 2235-251, Aug 2002.
- [30] T. Kohnen, D. D. Koch, MyiLibrary., and SpringerLink (Online service). (2009). *Cataract and refractive surgery progress III ([3rd ed.)*. Available: <http://turing.library.northwestern.edu/login?url=http://dx.doi.org/10.1007/978-3-540-76380-2>
- [31] R. D. Sperduto and D. Seigel, "Senile lens and senile macular changes in a population-based sample," *Am J Ophthalmol*, vol. 90, pp. 86-91, Jul 1980.
- [32] K. P., "Can the Topical Aldose Reductase Inhibitor Kinostat(TM) Clinically Prevent Cataracts in Diabetics?," in *Accommodation Club 8th Meeting*, Bascom Palmer, 2012.
- [33] T. Root. (2009). *Ophthobook*. Available: <http://www.ophthobook.com>
- [34] R. Steinert, *Cataract Surgery: Technique, Complications, and Management*, 2e: Saunders, 2003.
- [35] P. B. Greenberg, V. L. Tseng, W. C. Wu, J. Liu, L. Jiang, C. K. Chen, I. U. Scott, and P. D. Friedmann, "Prevalence and predictors of ocular complications associated with cataract surgery in United States veterans," *Ophthalmology*, vol. 118, pp. 507-14, Mar 2011.
- [36] L. Vock, R. Menapace, E. Stifter, M. Georgopoulos, S. Sacu, and W. Buhl, "Posterior capsule opacification and neodymium:YAG laser capsulotomy rates with a round-edged silicone and a sharp-edged hydrophobic acrylic intraocular lens 10 years after surgery," *J Cataract Refract Surg*, vol. 35, pp. 459-65, Mar 2009.

- [37] N. Awasthi, S. Guo, and B. J. Wagner, "Posterior capsular opacification: a problem reduced but not yet eradicated," *Arch Ophthalmol*, vol. 127, pp. 555-62, Apr 2009.
- [38] D. J. Apple and J. Sims, "Harold Ridley and the invention of the intraocular lens," *Surv Ophthalmol*, vol. 40, pp. 279-92, Jan-Feb 1996.
- [39] O. Nishi, K. Nishi, C. Mano, M. Ichihara, and T. Honda, "The inhibition of lens epithelial cell migration by a discontinuous capsular bend created by a band-shaped circular loop or a capsule-bending ring," *Ophthalmic Surg Lasers*, vol. 29, pp. 119-25, Feb 1998.
- [40] O. Nishi, K. Nishi, and K. Sakanishi, "Inhibition of migrating lens epithelial cells at the capsular bend created by the rectangular optic edge of a posterior chamber intraocular lens," *Ophthalmic Surg Lasers*, vol. 29, pp. 587-94, Jul 1998.
- [41] S. D. McLeod, V. Portney, and A. Ting, "A dual optic accommodating foldable intraocular lens," *Br J Ophthalmol*, vol. 87, pp. 1083-5, Sep 2003.
- [42] A. L. Sheppard, A. Bashir, J. S. Wolffsohn, and L. N. Davies, "Accommodating intraocular lenses: a review of design concepts, usage and assessment methods," *Clin Exp Optom*, vol. 93, pp. 441-52, Nov 2010.
- [43] J. L. Alio, J. Ben-nun, J. L. Rodriguez-Prats, and A. B. Plaza, "Visual and accommodative outcomes 1 year after implantation of an accommodating intraocular lens based on a new concept," *J Cataract Refract Surg*, vol. 35, pp. 1671-8, Oct 2009.
- [44] H. N. Sen, A. U. Sarikkola, R. J. Uusitalo, and L. Laatikainen, "Quality of vision after AMO Array multifocal intraocular lens implantation," *J Cataract Refract Surg*, vol. 30, pp. 2483-93, Dec 2004.
- [45] H. Lesiewska-Junk and J. Kaluzny, "Intraocular lens movement and accommodation in eyes of young patients," *J Cataract Refract Surg*, vol. 26, pp. 562-5, Apr 2000.
- [46] J. S. Cumming, D. M. Colvard, S. J. Dell, J. Doane, I. H. Fine, R. S. Hoffman, M. Packer, and S. G. Slade, "Clinical evaluation of the Crystalens AT-45 accommodating intraocular lens: results of the U.S. Food and Drug Administration clinical trial," *J Cataract Refract Surg*, vol. 32, pp. 812-25, May 2006.
- [47] S. Kasthurirangan, E. L. Markwell, D. A. Atchison, and J. M. Pope, "MRI study of the changes in crystalline lens shape with accommodation and aging in humans," *J Vis*, vol. 11, 2011.
- [48] O. Findl and C. Leydolt, "Meta-analysis of accommodating intraocular lenses," *J Cataract Refract Surg*, vol. 33, pp. 522-7, Mar 2007.

- [49] I. L. Ossma, A. Galvis, L. G. Vargas, M. J. Trager, M. R. Vagefi, and S. D. McLeod, "Synchrony dual-optic accommodating intraocular lens. Part 2: pilot clinical evaluation," *J Cataract Refract Surg*, vol. 33, pp. 47-52, Jan 2007.
- [50] S. D. McLeod, L. G. Vargas, V. Portney, and A. Ting, "Synchrony dual-optic accommodating intraocular lens. Part 1: optical and biomechanical principles and design considerations," *J Cataract Refract Surg*, vol. 33, pp. 37-46, Jan 2007.
- [51] A. G., "Dual Optics Accommodating IOLs," in *Mastering the Presbyopic Surgery: Lenses and Phakic IOLs*, R. E. Garg A., Lin J., Goes F., Lovisolo C., Malyugin B., Ed., ed New Delhi: Jaypee Brothers Medical Publishers, pp. 189-194.
- [52] W. Qiao, D. Johnson, F. S. Tsai, S. H. Cho, and Y. H. Lo, "Bio-inspired accommodating fluidic intraocular lens," *Opt Lett*, vol. 34, pp. 3214-6, Oct 15 2009.
- [53] J. Kessler, "Experiments in Refilling the Lens," *Arch Ophthalmol*, vol. 71, pp. 412-7, Mar 1964.
- [54] S. A. Koopmans, T. Terwee, J. Barkhof, H. J. Haitjema, and A. C. Kooijman, "Polymer refilling of presbyopic human lenses in vitro restores the ability to undergo accommodative changes," *Invest Ophthalmol Vis Sci*, vol. 44, pp. 250-7, Jan 2003.
- [55] S. A. Koopmans, T. Terwee, A. Glasser, M. Wendt, A. S. Vilupuru, T. G. van Kooten, S. Norrby, H. J. Haitjema, and A. C. Kooijman, "Accommodative lens refilling in rhesus monkeys," *Invest Ophthalmol Vis Sci*, vol. 47, pp. 2976-84, Jul 2006.
- [56] O. Nishi and K. Nishi, "Accommodation amplitude after lens refilling with injectable silicone by sealing the capsule with a plug in primates," *Arch Ophthalmol*, vol. 116, pp. 1358-61, Oct 1998.
- [57] Y. Nishi, K. Mireskandari, P. Khaw, and O. Findl, "Lens refilling to restore accommodation," *J Cataract Refract Surg*, vol. 35, pp. 374-82, Feb 2009.
- [58] O. Nishi, Y. Nakai, Y. Yamada, and Y. Mizumoto, "Amplitudes of accommodation of primate lenses refilled with two types of inflatable endocapsular balloons," *Arch Ophthalmol*, vol. 111, pp. 1677-84, Dec 1993.
- [59] O. Nishi, T. Hara, T. Hara, Y. Sakka, F. Hayashi, K. Nakamae, and Y. Yamada, "Refilling the lens with a inflatable endocapsular balloon: surgical procedure in animal eyes," *Graefes Arch Clin Exp Ophthalmol*, vol. 230, pp. 47-55, 1992.
- [60] A. Palsule, "Silicone and Fluorosilicone Based Materials for Biomedical Applications," Materils Science, University of Cincinnati, 2010.

- [61] B. Ratner, Bankman, I., *Biomedical Engineering Desk Reference*: Academic Press, 2009.
- [62] P. Jerschow, *Silicone Elastomers* vol. 12, 2001.
- [63] W. S., "Synthetic Silicas," in *Handbook of Fillers for Plastics*, M. J. Katz H., Ed., ed New York: Van Nostrand Reinhold, 1987, pp. 177-178.
- [64] C. J. Colas A., "Silicone Biomaterials: History and Chemistry," in *Biomaterials Science: An Introduction to Materials in Medicine*, R. B., Ed., ed: Academic Press, 2004.
- [65] L. R., "Composite Biomaterials," in *Biomaterials: Principles and Applications*, B. Park J., J., Ed., ed Boca Raton, FL: CRC Press, 2003, pp. 79-94.
- [66] L. A. Park S., Goel V., Keller J., "Hard Tissue Replacements," in *Biomaterials: Principles and Applications*, B. Park J., J., Ed., ed Boca Raton, FL: CRC Press, 2003, pp. 173-206.
- [67] C. McConville, G. P. Andrews, T. P. Lavery, A. D. Woolfson, and R. K. Malcolm, "Rheological Evaluation of the Isothermal Cure Characteristics of Medical Grade Silicone Elastomers," *Journal of Applied Polymer Science*, vol. 116, pp. 2320-2327, May 15 2010.
- [68] G. Gao, "Large Scale Molecular Simulations with Applications to Polymers and Nano-scale Materials," PhD, Physics, California Institute of Technology, Pasadena, California, 1998.
- [69] K. Menard, *Dynamic Mechanical Analysis: A Practical Introduction, Second Edition*. Boca Raton, FL: CRC Press, 2008.
- [70] K. Stathi, P. A. Tarantili, and G. Polyzois, "The effect of accelerated ageing on performance properties of addition type silicone biomaterials," *J Mater Sci Mater Med*, vol. 21, pp. 1403-11, May 2010.
- [71] I. Stevenson, L. David, C. Gauthier, L. Arambourg, J. Davenas, and G. Vigier, "Influence of SiO₂ fillers on the irradiation ageing of silicone rubbers," *Polymer*, vol. 42, pp. 9287-9292, Oct 2001.
- [72] E. Wong, "Modeling and Control of Rapid Cure in Polydimethylsiloxane (PDMS) for Microfluidic Device Applications," PhD, Mechanical Engineering, Massachusetts Institute of Technology, Boston, MA, 2010.
- [73] C. J. Wolf, K. L. Jerina, H. J. Brandon, and V. L. Young, "The transport of octamethylcyclotetrasiloxane (D-4) and polydimethylsiloxane (PDMS) in lightly cross-linked silicone rubber," *Journal of Biomaterials Science-Polymer Edition*, vol. 12, pp. 801-815, 2001.

- [74] J. Comyn, *Polymer Permeability*. London, 1985.
- [75] D. M. Brewis, J. Comyn, and C. Phanopoulos, "Effect of Water on Some Wood Adhesives," *International Journal of Adhesion and Adhesives*, vol. 7, pp. 43-48, Jan 1987.
- [76] D. M. Brewis, J. Comyn, and S. T. Tredwell, "Diffusion of Water in Some Modified Phenolic Adhesives," *International Journal of Adhesion and Adhesives*, vol. 7, pp. 30-32, Jan 1987.
- [77] M. Ott, "Visual accommodation in vertebrates: mechanisms, physiological response and stimuli," *J Comp Physiol A Neuroethol Sens Neural Behav Physiol*, vol. 192, pp. 97-111, Feb 2006.
- [78] L. Z. Bito, P. L. Kaufman, C. J. DeRousseau, and J. Koretz, "Presbyopia: an animal model and experimental approaches for the study of the mechanism of accommodation and ocular ageing," *Eye (Lond)*, vol. 1 (Pt 2), pp. 222-30, 1987.
- [79] O. L. Wildsoet C., Garcia M., "Pilocarpine-Stimulated Pupil and Accommodative Changes in Guinea Pigs," presented at the Association for Research in Vision and Ophthalmology, Fort Lauderdale, FL, 2012.
- [80] B. Levy and J. G. Sivak, "Mechanisms of Accommodation in the Bird Eye," *Journal of Comparative Physiology*, vol. 137, pp. 267-272, 1980.
- [81] R. Gerometta, A. C. Zamudio, D. P. Escobar, and O. A. Candia, "Volume change of the ocular lens during accommodation," *Am J Physiol Cell Physiol*, vol. 293, pp. C797-804, Aug 2007.
- [82] K. Ehrmann, A. Ho, and J. M. Parel, "Biomechanical analysis of the accommodative apparatus in primates," *Clin Exp Optom*, vol. 91, pp. 302-12, May 2008.
- [83] M. A. Reilly, P. D. Hamilton, and N. Ravi, "Dynamic multi-arm radial lens stretcher: a robotic analog of the ciliary body," *Exp Eye Res*, vol. 86, pp. 157-64, Jan 2008.
- [84] F. Hunter. *Scheimpflug principle - Wikipedia, the free encyclopedia*. Available: http://en.wikipedia.org/wiki/Scheimpflug_principle
- [85] N. Brown, "The change in shape and internal form of the lens of the eye on accommodation," *Exp Eye Res*, vol. 15, pp. 441-59, Apr 1973.